SETCOR
Conferences & Events

GAMS Dubai 2015 International Conference Proceeding

http://www.setcor.org/conferences/GAMS-2015

Nano Technology Application in Stabilizing Expansive Soil: Irbid Clay

Abdulla A. Sharo[1], Ahmed S. Alawneh[2], Aslam A. Alomari[3]

[1]Abdulla A. Sharo, Ph.D, Assistant Professor, Department of Civil Engineering, Jordan University of Science and Technology, P.O. Box 3030, Irbid 22110, Jordan, E-mail: aasharo@just.edu.jo

[2]Ahmed A. Alawneh, Professor, Department of Civil Engineering, Jordan University of Science and Technology, P.O. Box 3030, Irbid 22110, Jordan, E-mail: asshlash@just.edu.jo

[3]Aslam A. Alomari, Ph.D, Assistant Professor, Department of Civil Engineering, Jordan University of Science and Technology, P.O. Box 3030, Irbid 22110, Jordan, E-mail: aaalomari3@just.edu.jo

ABSTRACT

Lately, there has been a great deal of interest for the application of nanotechnology in geotechnical engineering. Soil stabilization is one of the fertile areas for the use of nanotechnology in the field of geotechnics. The foremost thrust of this study is to conduct a systematic investigation for the evaluating the effects of the addition of nanomaterials on the expansive soil strength's characteristics, mainly compaction compenets which includes maximum dry density ($\gamma_{d\text{-}max}$) and optimum moisute content ($\omega_{opt.}$), through adding nano clay with differenrt percentages by weight to a slected expansive clayey soil chosen from Irbid city.

From the work conducted in this study the nano clay addition improvs the selected soil geotechnical properties where the maximum dry densty increased with the increase in percenteage og nano clay added to the soil. Same general incrasing trend in the optimum moisture content associated with the increase in percentage of nano clay was reported.

Keywords: expansive soil, soil compaction, nano clay, maximum dry density, optimum moisture content.

INTRODUCTION

Clayey soils are termed as expansive if they experienced shrink and swell behavior associated with changes in soil moisture. In response to the moisture changes, expansive soil will experince changes in its volume. This change in volume could be experinced as uplift pressure on the footing if prohibited and, consequently, could be harmfull to the strcture.

Due to the generally dry climate in Irbid city (Fig. 1), shrinkage occure more frequent than swelling which mainly takes place during the short wet season. Also, within the residential areas, watering the vegetations and landscaping surrounging the buildings is another important factor that can be active, particulary, when the footings are resting on expansive clay soils.

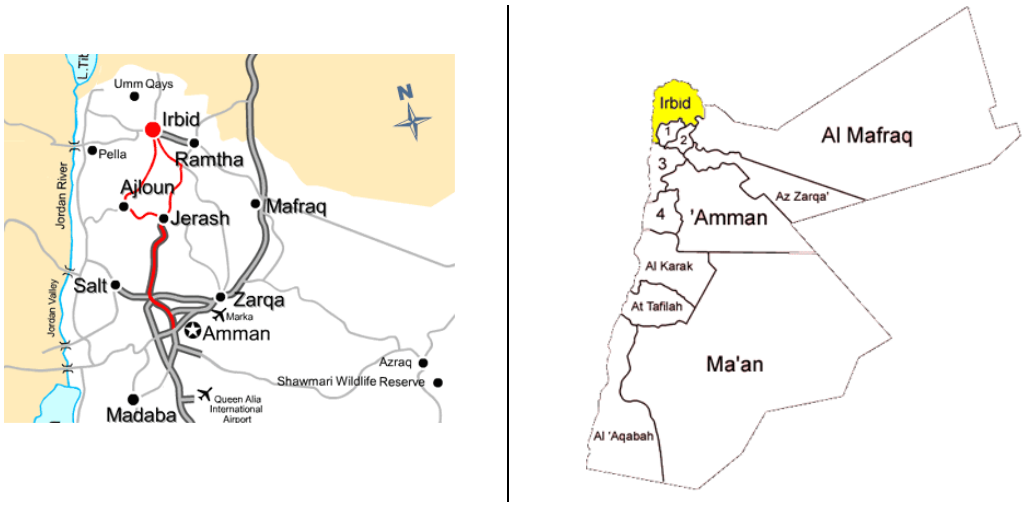

FIG. 1. Jordan map showing the location of Irbid city.

The above mentioned facts rises the need for an effective treatement for such a soils to become more stable and cabable of accomedating strctures. Recently, there has been a great deal of interest for the application of nanotechnology in geotechnical engineering. Soil stabilization is one of the fertile areas for the use of nanotechnology in the field of geotechnics. According to Kolias *et al*. (2005) soil stabilisation is a customary strategy used to enhance soils to accomplish the specifications of different projects.

In this study, a systematic investigation for the effects of the addition of nanomaterials on the expansive soil strength's characteristics, mainly compaction, was carried out. The improvement attained is dependent on the type of nanomaterials. Nano clay, Fig. 2, was used in this study as an additive material.

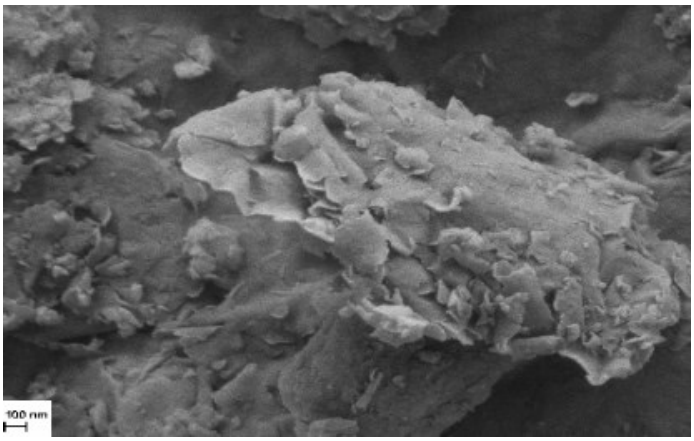

FIG. 2. The Nano-Clay used in this study.

SOIL USED IN THIS STUDY

In this study, the soil tested was obtained from Irbid city, northern region of Jordan (Fig. 1). Irbid soil is well recognized to geotechnical engineers to be expansive clayey soil with a smectite as a dominant mineral. A disturbed soil samples from the bottom of about 1.5 m borrow bit was collected from the eastern part of Irbid city.

The physical properties were estimated according to American Society for Testing and Materials specifications (ASTM D 7263–09) and (ASTM D 854-02). Based on the results, the solid unit weight of the clay was approximately 17.4 kN/m^3 and the specific gravity of soil solids was in the order of 2.76. Adaptation of the Unified Soil Classification System (USCS), the soil was classified as high plasticity clay (CH).

NANO CLAY EFFECT ON THE COMPACTION CONDITIONS

The effect of nano-clay addition to the soil samples is presented by illustrations Fig. 3 and Fig.4. Figure 3 illustrates the effect of nano clay on the maximum dry density ($\gamma_{d\text{-}max.}$) while figure 4 illustrates the effect of nano clay on the optimum moisture content ($\omega_{opt.}$). Both illustrations illustrate that nano-clay addition increased the dry density and the optimum moisture content of this type of clay. This increase in optimum moisture content and the maximum dry density as well is generally considered as an indication of soil improment.

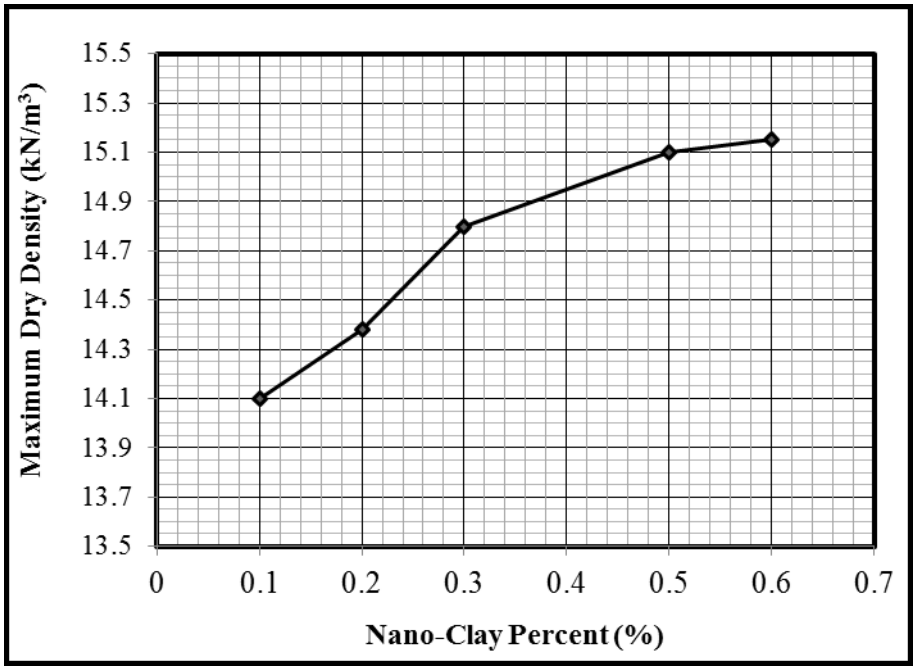

FIG. 3. Effect of different Nano-clay percentage (%) on maximum dry density ($\gamma_{d\text{-}max.}$).

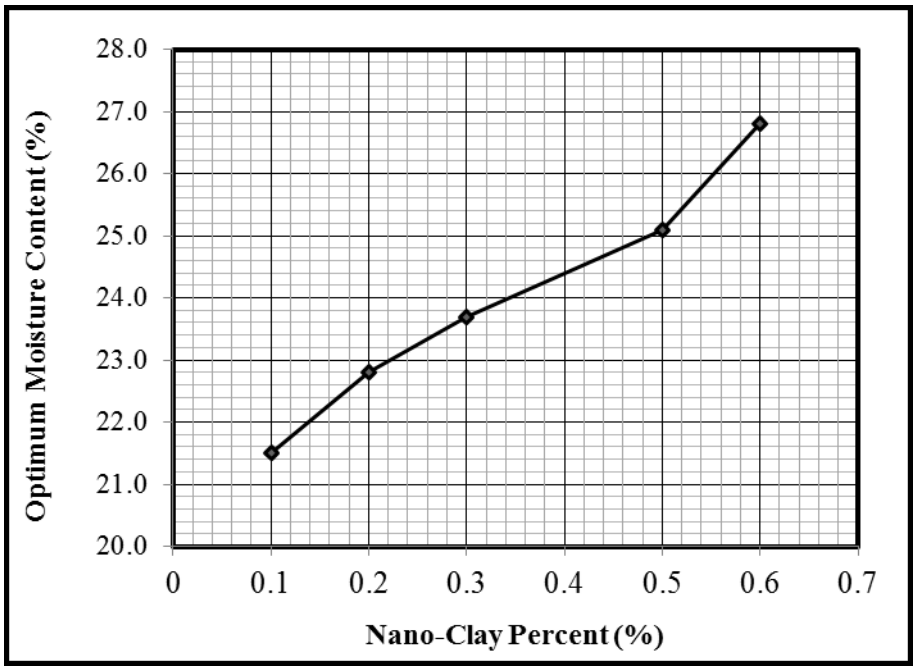

FIG. 3. Effect of different Nano-clay percentage (%) on optimum moisture content ($\omega_{opt.}$).

CONCLUSIONS

This research was directed to study the possibility of of improving the geotechnical properties of selected expansive soil from Irbid city. The effect of addition of nano clay material on the geotechnical properties, namely; dry density and optimum moisture content, of Irbid soil was carried out. In line with study the following conclusions can be drawn:

- The dry density of the selected Irbid clay soil was increased as the amount of nano clay add to the soil increase indicating iprovment of this soil.
- The optimum moisture content of the selected Irbid clay was increased as the amount of nano clay add to the soil increased indicating improvement of this soil.

The auther(s) belevie that these results will help invistigators for further improvement for the geotechnical properties of expansive soils.

REFERENCES

ASTM D7263-09 Standard Test Methods for Laboratory Determination of Density (Unit Weight) of Soil Specimens, "Annual Book of ASTM Standards, Section 4, Vol. 04.09, Soil and Rock; Building Stones," ASTM, Philadelphia, 1988.

ASTM D854-02 Standard Test Methods for Specific Gravity of Soils, "Annual Book of ASTM Standards, Section 4, Vol. 04.08, Soil and Rock; Building Stones," ASTM, Philadelphia, 1988.

Kolias, S., V. Kasselouri-Rigopoulou and A. Karahalios, 2005. Stabilisation of clayey soils with high calcium fly ash and cement. Cement Concrete Comp., 27(2): 301-313.

Synthesis and Characterization of Hybrid Material based on Ionic Liquid and Amorphous Porous Silicon

Mohamed R. Tchalala[1]*, Sahraoui Chaieb[1]
[1]Physical Sciences and Engineering Division, King Abdullah University of Science and Technology, Thuwal 23955-6900, Saudi Arabia

Abstract:
Ionic liquids are salts that are liquids over a wide range of temperature (Suarez et al., 1998). Because they can be designed by a choice of a cation and anion, they are called "designer solvents." (Eik et al., 2003) they are gaining huge momentum as new solvents for nanoparticles synthesis, or for batteries as well in heat storage for solar-thermal. They have potential applications in gas handling, pharmaceuticals, nuclear fuel processing and many other industrial processes such as separation or paper industry. In contrast to organic solvents, ionic liquid have a large liquid range, high thermal stability, polarity and volatility. They are non-flammable and are miscible with a variety of solvents. Their physico-chemical properties can be designed by judicious choice of cation/anion combinations, which makes them the most diverse solvent around.

Although IL has been studied as suitable solvents for nanoparticles synthesis as well as for catalysis their interactions with substrates as well as nanoparticle have been largely ignored. In the current study we report for the first time the behavior of various ILs when mixed with silicon nanoparticles for eventual applications in batteries or solar cells. While fluorine based IL behave as good solvent to the nanoparticles, the thiocyanate complexes with traces of iron ions(khare et al., 2010) that were used as a catalysis during the nanoparticles synthesis. This complexation stabilizes the dispersion. Several spectroscopic studies were used to investigate the interactions between the silicon nanoparticles and the ILs. We suggest that, contrary to the common belief, not all ILs are good solvents for silicon nanoparticles because of many limiting factors.

Keywords: ionic liquids, cation/anion combinations, silicon nanoparticles, hybrid material,complexation, stabilization, potential applications.

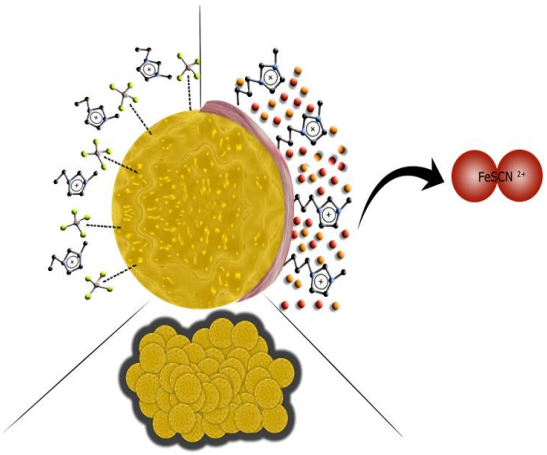

Figure 1: Schematic representation of nonstructural organization in binary amorphous porous silicon/ionic liquids mixtures

References:

Suarez, P. A. Z., Einloft, S.,Dullius, J. E. L., Souza, R. F., Dupont,J. (1998), Synthesisand Physical-chemical Properties of Ionic Liquids Based on 1-n-Butyl-3-Methylimidazolium Cation. J. Chim. Phys. Phys.-Chim. Biol., 95, 1626-1639.

Eike, D. M., Brennecke, J. F., Maginn,E. J., (2003)Predicting Melting Points of Quaternary Ammonium Ionic Liquids.Green Chem.,5, 323-328.

Khare, V., Kraupner, A.,Mantion, A., Jelicić, A., Thünemann, A. F., Giordano, C.,Taubert, A. (2010) Stable Iron Carbide Nanoparticle Dispersions in [Emim][SCN] and [Emim][N(CN)2] Ionic Liquids.Langmuir,26,10600-10605.

Synthesis, Characterization and Applications of Iron Oxide Nanoparticles in Cosmetics

Contributors: Dr Monika Vats[1], Dr M Nidhin[1], Dr Seema Pathak[1], Dr K J Sreeram[2]
[1] Department of Chemistry, ASAS, Amity University, Gurgaon, India
[2] Principal Scientist, CSIR- CLRI, Chennai, India

1. INTRODUCTION

Cosmetics are the materials used for beautification or improvement of appearance and confidence [1]. The word has evolved from Greek word kosmeticos mean adorn [1]. In last 3-4 decades use of cosmetics by females and males has increased a lot [1]. Therefore it becomes indispensable for cosmetics industries worldwide to enhance the functional properties of cosmetics. The uses of nanomaterial in cosmetics have been reported thousand years ago in ancient Egypt [2]. Nanomaterials has been embraced by the cosmetics industry for several reasons such as they penetrate deeper into skin, they posses antioxidant property, they protect against harmful rays, they enhance properties at the nano level including color, transparency, solubility etc [3]. Iron oxide nanoparticles are well known for their excellent biocompatibility, chemical stability and less toxicity and commonly used in targeted drug delivery, contrast agents in MRI [4]. Along with the above said properties, there are several advantages of using iron oxides nanomaterial in cosmetics as they are gentle and non-toxic for the surface of the skin, they are safe and non-irritating, they may be used as colouring agents in cosmetics, and they are resistant to moisture [5]. This paper reports the synthesis of iron oxide nanoparticles through biotemplates [6], the characterization of nanoparticles which was carried out using TEM, SEM, TGA, and DLS and application of synthesised nano particle used in various cosmetics products such as nanosuncream, talcum powder, nanolipstic.

2. EXPERIMENTAL

2.1 Preparation and of Iron oxide Nano Particles

Iron oxide nanoparticles were synthesized via a sustainable, environmentally friendly and green methodology as reported [6].

2.2 Characterization of the Synthesized Nanoparticles

Powder XRD analysis was done on a Rigaku, Miniflex, (II) Desktop X-ray diffractrometer. Morphology of nanoparticles was recorded by SEM (FEI Quanta 200 FEG High resolution Scanning Electron Microscope). Dynamic Light scattering (DLS) was done with help of Zetasizer 3000HSA (Malvern Instruments, UK).

2.3 Preparation of Cosmetics

2.3.1 Method of synthesis of lipstick:

20 ml bees wax and 5 ml olive oil are melted in a different bowls. With continuous stirring the contents of the bowls mixed and heated till both are completely miscible with each other. To this mixture 5 ml vodka is added with constant and vigorous stirring. Now add 0.1 g of iron oxide or nanosized iron oxide. Stir the mixture and add flavor/essence/essential oil as desired. Pour the mixture in lipstick mould to give the desired shape to the lipstick and refrigerate it for 3 to 5 hours.

2.3.2 Method synthesis of sunscreen:

Take 25 ml olive oil and heat it. Add 2 ml heated beeswax in it and stir it till all the beeswax is dissolve in oil. Now add 1 ml essential oil and 0.1g iron oxide nanoparticle/iron oxide to the mixture with constant stirring. Allow the mixture to cool down at room temperature to obtain the sunscreen.

2.3.3 Method synthesis of talcum powder:

Combine equal amount of corn starch, tapioca starch and arrowroot powder in a small bowl, and mix thoroughly. Directly add pinch of ferric oxide nanoparticle/ferric oxide to the mixture of starch. Add

the fragrance or essential oil to a cotton ball or absorbent cotton pad. Put the perfumed cotton ball or cotton pad in a container with the talcum powder and stir it or shake it well. Allow the perfumed talcum powder to sit for 24 hours, and stir or shake it again. Remove the perfumed pad or cotton ball and discard it. Put the perfumed talcum powder in the containers, and use as desired.

2.4 *In Vitro* SPF Analysis

SPF or Sun Protection Factor is a measurement of sunscreen that how far it will protect the skin from UVB rays. SPF value was calculated through *in-vitro* spectroscopic method [7]. The following protocol was used to record the observations. 1.0 g of the cosmetics were weighed and transferred to volumetric flask of 100 mL which was diluted to the volume with ethanol. The above solution was ultrasonicated for 5 min followed by filtration through cotton. Reject the first 10 mL, and from the rest of the solution take only 5.0 mL aliquot and transfer it to 50 mL volumetric flask. Dilute the flask to volume with ethanol. Now take 5.0 mL aliquot of the solution from 50 ml volumetric flask and transfer it to 25 mL volumetric flask and again the volume completed with ethanol. The absorption spectra of samples in solution were obtained in the range of 290 to 320 nm using 1 cm quartz cell, and ethanol as a blank for every 5 nm, and three determinations were made at each point. It can be calculated using the Mansur equation: SPF = CF X MF

Where: EE – erythemal effect spectrum; I – solar intensity spectrum; Abs - absorbance of sunscreen product; CF – correction factor (= 10). The values of EE x I are constants and Sayre et al determined them.

$$\text{MF}= \sum_{320}^{290} EE(\lambda) X\ Abs\ (\lambda)$$

2.4.1 *In vitro* antimicrobial activity

Cosmetics were screened for antibacterial activity against bacteria, E. coli, (Gram negative) by reported agar well-diffusion method. Cultures were grown overnight at 37^0C in 20 ml of agar medium in Petri plate. Then the agar plates were swabbed with the 100 µL inocula of bacterium and left for 15 min for adsorption. With the help of sterile plastic pipette having 8 mm diameter, wells were made into the seeded agar plates. The wells were loaded with a 100 µL volume with concentration of 2.0 mg/mL reconstituted in DMSO. All the plates were incubated at 37°C for 24 hr. Antibacterial activity of each product was observed by measuring the zone of growth inhibition against the test organisms.

3 RESULT AND DISCUSSION

The synthesized nano particle was analyzed for the particle size, crystalline behavior and morphology with the help of DLS, XRD and HRSEM, respectively. The size of the particle was found to be less than 50 nm. The Figure 1 (a) and (b) represent the XRD pattern and SEM images [6] for the synthesized nano iron oxide particles.

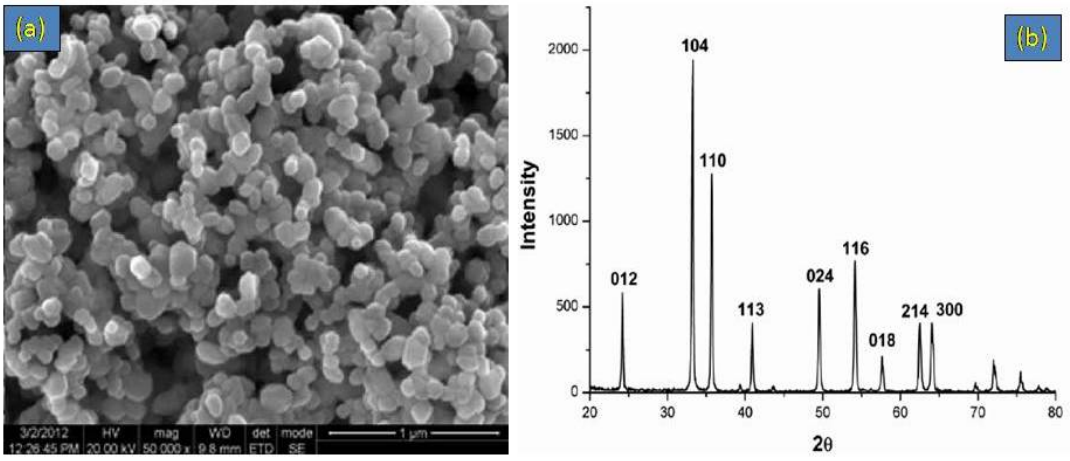

Figure 1. (a) FESEM images and (b) XRD pattern of the synthesized iron oxide nano particles nanoparticles [6].

The synthesized iron oxide nanoparticles were used in various preparations of cosmetics products such as nano sunscreen talcum powder and nanolipstic as presented in Figure 2. These nanoparticles provide uniform colour, higher SPF value and excellent UV protection to the cosmetic products. The lipstick formed is a solid and glossy stick. The sunscreen formed is a greasy and glossy. Fe_2O_3 nanoparticle helped for imparting pinkish red color as well as homogeneity to the talcum powder.

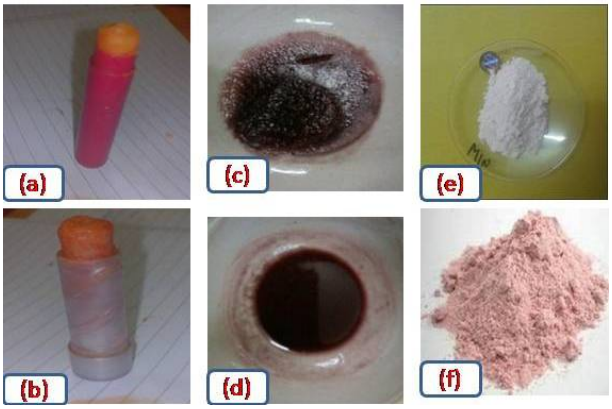

Figure 2 (a) Lipstick made using iron oxide, (b) lipstick made using iron oxide nanoparticle, (c) sunscreen made using iron oxide, (d) sunscreen using iron oxide nanoparticle, (e) talcum powder made using iron oxide and (f) talcum powder iron oxide nanoparticle.

The SPF is a quantitative analysis of efficiency of cosmetics. A cosmetic should have a wide range of absorbance between 290 and 400 nm, so that it is efficient in preventing sunburn and skin damage. The *in vitro* SPF screening test is good during product development [8]. In this paper synthesized cosmetics were evaluated for SPF by UV spectrophotometry using Mansur mathematical equation. The SPF values were in the range of 9 to 18. The SPF values of samples obtained via the UV spectrophotometric method were shown in Table 1. All the samples presented SPF values under the labelled amount (between 2 to 50). Dermatologists recommend a cosmetic product with SPF 15 or greater for all types of skins. Most of the oils have SPF value around 2. Among the cosmetic samples, sample 4 exhibits a maximal absorbance whereas sample 1 showed the lowest SPF as observed in Table 1. From the table it can be analysed that cosmetics containing nano-sized iron oxide displayed more SPF than the cosmetics containing normal iron oxide.
The AS/NZ standard specifies that to be classified as a broad spectrum protection product, a cosmetic product should not have a protection factor less than 4 [9], which support that the synthesized cosmetics are broad spectrum UV protector.
It has been observed that data variation can be due to (a) the use of non validated spectrophotometric methodology, (b) the use of different solvents, (c) the type of emulsion, (d) the effects of vehicle components, (e) the pH system [10]. Several times excipients and active ingredients also cause interfering with those of UVA and UVB sunscreens, etc. particularly for those with SPF more than 15.

Table 1. *In Vitro* Calculation of SPF Value

Sample. No.	Name of the Cosmetics	SPF Value
1.	Lipstick (iron oxide)	9± 0.2
2.	Lipstick (nanoparticle iron oxide)	18 ± 0.3
3.	Sun Screen (iron oxide)	10± 0.3
4.	Sun Screen (nanoparticle iron oxide)	19± 0.5
5.	Talcum Powder (iron oxide)	10 ± 0.3
6.	Talcum Powder (nanoparticle iron oxide)	18 ± 0.3

Antimicrobial materials protect against the growth of microorganisms in personal care products, including bacteria, viruses and fungi and play a vital role in ensuring that cosmetics are free from microorganisms during the storage and after they are opened. They are generally in low amounts [11]. Inorganic nano metal oxides may serve as effective disinfectants and efficient antibacterial for

cosmetic products. The prepared cosmetic were analysed for anti-microbial activity against E. Coli. It was observed the zone of inhibition was wider in case of cosmetics containing nano-sized iron oxide displayed more SPF than the cosmetics containing normal iron oxide, which is clearly depicted by Figure 3.

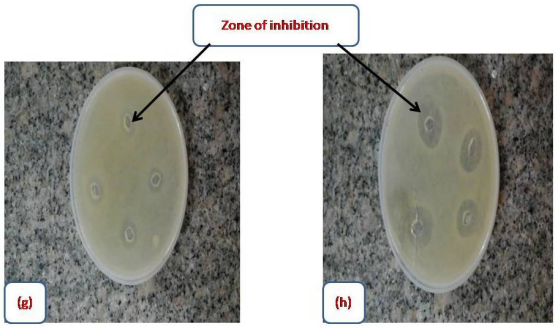

Figure 3. (g) Antibacterial activity of lipstick (iron oxide) showing small zone of inhibition, (h) Antibacterial activity of lipstick (nano particle iron oxide) showing bigger zone of inhibition.

4. CONCLUSIONS

The cosmetics made by using iron oxide nanoparticle definitely possessing more properties than the cosmetics made by using iron oxide. Iron oxide nanoparticle gives more protection against the harmful UV rays. Iron oxide nanoparticle is also helpful for imparting brownish/pinkish color homogeneity to the cosmetics. They also possess good anti-microbial properties.

5. AKNOLEDGEMENT

We are thankful to Dr Anurag Sharma, Asst. Prof. Department of Chemistry, Amity University, Gurgaon, India, for helping us in evaluating microbial activity. E. Coli was procured from lab of Dr S Mazumdar, Asst. Prof. Department of Chemistry, Amity University, Gurgaon, India. We are also thankful to technical staff of the Chemistry Department, Amity University, Gurgaon, India.

6. REFRENCES

1. (a) http://www.slideshare.net/jaseemusthu/history-of-cosmetics-14994473.
   (b) Skin cosmetics: An overview, LAP Lambert Academic Publishing (2013) ISBN-13: 978-3-659-49194-8
2. L. C. Rathbun, Nanotechnology-based Hair Dye – an ancient Egyptian recipe, (2006), http://www.nanooze.org/nanotechnology-based-hair-dye-an-ancient-egyptian-recipe).
3. S. Raj, S. Jose, U. S. Sumod, and M. Sabitha, Nanotechnology in cosmetics: Opportunities and challenges," J Pharm Bioallied Sci. 4 (2012) 186–193.
4. A. K. Gupta and M. Gupta, Synthesis and surface engineering of iron oxide nanoparticles for biomedical applications, 26 (2005) 3995-4021.
5. http://www.skinstore.com/iron-oxides.aspx.
6. M. Nidhin, R. Aravindhan, and K. J. Sreeram, Green Synthesis of Monodisp ersed Iron Oxide Nanopartic les for Leather Finishing, JALCA, 109 (2014)184-188
7. (a) Fonseca and Rafaela, Determination of Sun Protection Factor by UV-Vis Spectrophotometry, Health Care Current Reviews, 1(2013) 1-4.
   (b) E. A. Dutra, Determination of sun protection factor (SPF) of sunscreens by ultraviolet spectrophotometry, Rev. Bras. Cienc. Farm., 2004, 40 (3), 381-385.
   (c) V. Sudhahar and V. Balasubramanian, Sun production factor (SPF) determination of marketed sunscreen formulation by In-Vitro method using UV-VIS spectrophotometer, Archives of Applied Science Research, 5 (2013) 119-122.
8. C. D. Kaur and S. Saraf, I*n vitro* sun protection factor determination of herbal oils used in cosmetics," Pharmacognosy Res. 2(2010) 22–25.
9. Michael W. Allen, Ph.D., Gordon Bain, Ph.D, Measuring the Sun Protection Factor (SPF) of Sunscreens, Thermo Fisher Scientific, Madison, WI, USA Application Note: 51463.
10. L. E. Agrapidis-Paloympis, R.B.Nash, N.A. Shaath, The effect of solvents on the ultraviolet absorbance of sunscreens. J. Soc. Cosmet. Chem., New York, 38 (1987) 209-221.
11. http://www.cosmeticsinfo.org/antimicrobials.

The use of optical fibers for environmental decontamination

S. Teixeira,[1,*] S. Y. Ryu,[2] K. Kühn,[1] M. Hoffmann,[2] G. Cuniberti[1,3,4]
[1]Institute for Materials Science and Max Bergmann Center of Biomaterials, Technische Universität Dresden, Dresden, Germany
[2]Environmental Science & Engineering, California Institute of Technology, Pasadena, USA
[3]Dresden Center for Computational Materials Science, Technische Universität Dresden, Dresden, Germany
[4]Center for Advancing Electronics Dresden, Technische Universität Dresden, Dresden, Germany
*sara.teixeira@nano.tu-dresden.de

Abstract
This paper investigates the application of photocatalysis in an optical fiber bundle reactor for water decontamination. Because quartz optical fibers (QOP) are expensive and require careful handling, polymer optical fibers (POF) seem to be more economic and an easier alternative. The end tip of the optical fibers was polished by sand paper and then dip coated in a hydrosol solution with the photocatalysts and let it dry. The photocatalytic activity was evaluated by the degradation of 5 mg L^{-1} of ciprofloxacin present in water. Two fibers diameters were chosen to test the degradation of ciprofloxacin. There are no significant differences on the photocatalytic activity between the two types of fibers.

Keywords: antibiotics, immobilization, pharmaceuticals, photocatalysis, sunlight.

1. Introduction

The presence of pharmaceuticals in water has become a great concern due to the adverse consequences at both human's health and wildlife [1]. They have been detected in surface and ground water [2], drinking water [3] and tap water [2]. Recently, antibiotics have arisen the interest of researchers given the capability to accelerate the development of resistant microorganisms [4]. Despite pharmaceuticals reaching wastewater treatment plants (WWTPs), the conventional WWTPs are ineffective in their removal [4, 5]. Thus, photocatalysis allows their rapid and efficient removal, transforming them into by-products with lower toxicity [6, 7]. The catalyst can be employed either in a colloidal or in an immobilized form. The main aim of using the immobilized form is that the costly and extra final filtration process can be avoided, which is especially important for water decontamination [8]. Optical fibers (OF) are used as a photocatalyst support and as a light transmission tool. Polymeric optical fibers (POF) have high mechanic flexibility and low cost making them more desirable than quartz optical fibers (QOF) with the disadvantage that they show higher propagation loss than the QOF [9].

2. Materials and Methods

2.1. Chemicals and Materials

We used TiO_2 P25 (Evonik), ZnO (IOLITEC Ionic Liquids Technologies GmbH), and ciprofloxacin (Sigma Aldrich). Water was obtained from a Millipore Milli-Q System (Water, Millipore).

2.2. Fibers preparation

The 8 cm end tip of the OF was roughened with sand paper. In the case of the QOF (FT1000UMT from Thorlabs) the 8 cm end was stripped down to the quartz core. The core of the QOF and the core of the POF (Conrad) were polished by sand paper. Then, the roughened portion was cleaned with a rug and acetone and dip coated in a solution of: (a) 0.5 g of TiO_2 in 3 ml of water; (b) 0.5 g of ZnO in 3 ml of water; (c) 0.25 g of ZnO + 0.25 mg of TiO_2 in 3 ml of water. It was then dried overnight at room temperature and then hot air dried for 30 min.

2.3. Photocatalytic degradation experiments

The light was focused at the top of the OF bundle and transmitted through the fibers. The three fiber bundles consisted of 20 of 2-mm diameter POF, 20 of 1-mm diameter POF, and 20 of 1-mm diameter QOF with 20 cm length. Spacing between fibers prevented exfoliation of the catalyst and improved the parallel pattern of the fibers. Prior to illumination, the solutions with the coated part inserted in the water were stirred in the dark for 30 min to achieve an adsorption-desorption equilibrium of the antibiotic on the photocatalyst's surface. Aliquots of 2 mL were withdrawn at determined time intervals. As controls, experiments were carried out in the absence of catalyst nanoparticles or without light. All other parameters in the control experiments were kept unchanged.

3. Results

SEM images (Figure 1) show a TiO_2 cracked coating immobilized on the fiber's surface revealing a not smooth coating. On one hand the cracks increase the surface area however, when inserted in water, the coating might get delaminated because of the water flow. There is a need to optimize the coating so delamination does not occur.

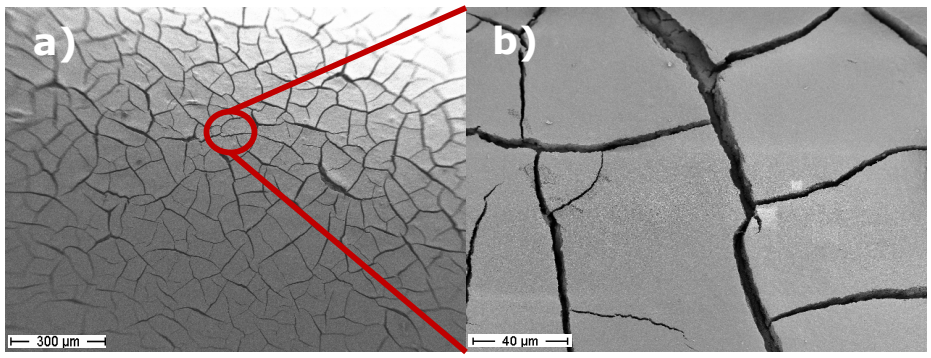

Figure 1 – SEM images of the a) surface of a coated optical fiber by TiO_2 and b) magnification of image a).

To evaluate the photocatalytic activity of the different OFs we tested the degradation of 5 mg L^{-1} of ciprofloxacin in water. Figure 2 illustrates the degradation profile of the antibiotic during the exposition to visible light. Ciprofloxacin is not degraded by visible light without catalyst (data not shown). In Figure 2a) we can see the degradation of the antibiotic by several photocatalysts immobilized in a 20 1-mm QOF bundle. All the catalysts exhibit similar degradation profile, in which after 3 hours of exposition to visible radiation 70 % of the antibiotic remained in water.

Comparing the results with the 1-mm POF it is shown that the degradation by immobilized TiO_2 was slightly improved although by ZnO was slightly reduced. These small differences might be caused due to the weak attachment of the catalyst onto the fiber's surface. There are no significant difference in the results by using 1-mm QOF and 1-mm POQ with the disadvantage of QOF being more rigid and harder to handle. For this reason we evaluated the degradation of the antibiotic in water by a 2-mm POF. Since the coated area was doubled, also the photoactivity doubled for ZnO. After 3 hours of exposition to visible light, only 40 % of antibiotic remained in water. The same happened for the mixture of ZnO/TiO_2. For TiO_2 no change was observed when compared to the 1-mm QOF and 1-mm POF which suggests a higher dependence of ZnO to the area of the coated photocatalyst.

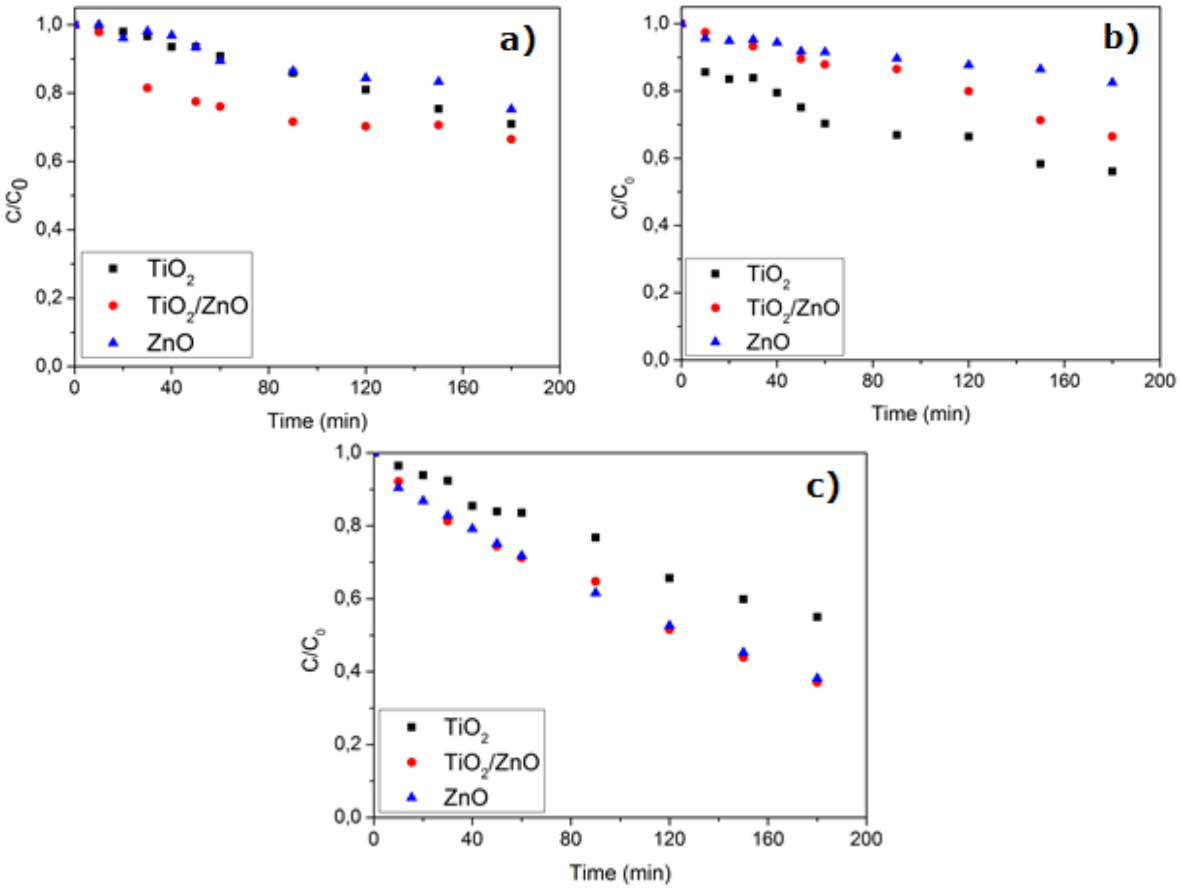

Figure 2 – Degradation of 5 mg L^{-1} ciprofloxacin by different photocatalysts immobilized on a) 1-mm quartz optical fiber; b) 1-mm polymer optical fiber; and c) 2-mm polymer optical fiber.

PMMA showed to have good transmittance and photodegradation resistance, and therefore it can be a good support if the photocatalyst adherence is improved.

4. Conclusion

The projection of effective reactor designs for large-scale use, as required by industrial and commercial applications, represents the main difficulty in the development of highly efficient photocatalytic reactors. Comparing the POF and QOF with the same fiber diameter, POF showed slight higher photocatalytic activity and have the advantage of being flexible. Increasing the diameter of the POF we enhance the photocatalytic activity. POF seem to be suitable for the use of decontamination of polluted water. It is now necessary to test the reusability of the fibers.

References

1. Isidori, M., Bellotta, M., Cangiano, M. & Parrella, A. Estrogenic activity of pharmaceuticals in the aquatic environment. *Environ. Int.* **35,** 826–9 (2009).
2. Li, W. C. Occurrence, sources, and fate of pharmaceuticals in aquatic environment and soil. *Environ. Pollut.* **187,** 193–201 (2014).
3. Fram, M. S. & Belitz, K. Occurrence and concentrations of pharmaceutical compounds in groundwater used for public drinking-water supply in California. *Sci. Total Environ.* **409,** 3409–17 (2011).
4. Pereira, J. *et al.* Photocatalytic degradation of oxytetracycline using TiO2 under natural and simulated solar radiation. *Sol. Energy* **85,** 2732–2740 (2011).
5. Cunningham, V., Binks, S. & Olson, M. Human health risk assessment from the presence of human pharmaceuticals in the aquatic environment. *Regul. Toxicol. Pharmacol.* **53,** 39–45 (2009).
6. Faramarzpour, M., Vossoughi, M. & Borghei, M. Photocatalytic degradation of furfural by titania nanoparticles in a floating-bed photoreactor. *Chem. Eng. J.* **146,** 79–85 (2009).
7. Fujishima, A., Zhang, X. & Tryk, D. TiO2 photocatalysis and related surface phenomena. *Surf. Sci. Rep.* **63,** 515–582 (2008).
8. Matsuoka, M., Toyao, T., Horiuchi, Y., Takeuchi, M. & Anpo, M. in *Photocatal. Water Purification_From Fundam. to Recent Appl.* (ed. Wiley-VCH Verlag GmbH & Co.) 179–197 (2013).
9. Kazuyuki Horie, Hideharu Ushiki, F. M. W. in *Mol. Photonics Fundam. Pract. Asp.* 151–175 (Wiley-VCH Verlag GmbH, 2000). doi:10.1002/9783527613205

Molecular dynamics simulation of functionalized graphene – a study of the mechanical properties of graphene

Liliana Sofia Melro, Ryszard Pyrz and Lars Rosgaard Jensen
Department of Mechanical and Manufacturing Engineering, Aalborg University
Fibigerstraede 16, 9220 Aalborg East, Denmark

Abstract
Molecular dynamics (MD) simulations were carried out to investigate the influence of functional groups on the mechanical properties of graphene. The Young's modulus was calculated for carboxyl (COOH), hydroxyl (OH), and carbonyl (C=O) functionalised layers. Results show a decrease of the Young's modulus with grafting of functional groups on the carbon network which can be attributed to the change in carbon – carbon bond hybridisation from sp^2 to sp^3. Carboxylic groups proved to influence the least the elastic properties, as the grafting is made by a carbon – carbon bond instead of carbon – oxygen as in the hydroxyl case. Different coverage densities as well as dissimilar organisations of hydroxyl groups were also assessed and showed the higher influence of big clusters on the mechanical properties than small clusters or distributed hydroxyl groups.

Keywords: functional groups, graphene, mechanical properties, molecular dynamics.

1. Introduction

Graphene is a monolayer of carbon atoms covalently bonded by sp^2 hybridized atoms in a hexagonal pattern. The length of carbon-carbon bonds is typically 1.42 Å, the bond angle 120º, and the layer thickness 3.4 Å. The majority of studies that take into account the mechanical properties of pristine and functionalised graphene focus on MD simulations.[1-3] It is worth noting that with functionalisation the bonding between the grafted carbon and the neighbouring atoms become sp^3 hybridized.[4]
In this work we considered the influence of different functional groups (hydroxyl, carbonyl, and carboxyl) as well as the density and orientation of grafting on the elastic modulus of graphene using MD simulations.

2. Experimental methods

2.1.1. Graphene development

Graphene models were built using Materials Studio 6.0 (Accelrys Software Inc.). A graphene layer simulation cell with 960 atoms and periodic boundary conditions was created with a density of 2.24 $g.cm^{-3}$ and volume 8 551 $Å^3$. Cell dimensions are a = 49 Å, b = 51 Å, c = 3.4 Å and $\alpha = \beta = \gamma = 90^{\circ}$.

2.1.2. Models with different functional groups

Functional groups carboxyl (COOH), hydroxyl (OH), and carbonyl (C=O) were randomly grafted onto the graphene structure resulting in 10 % functionalisation (Figure 1). Adjustments to carbon-carbon bonds were made as graphene is a sp^2 hybridized material.

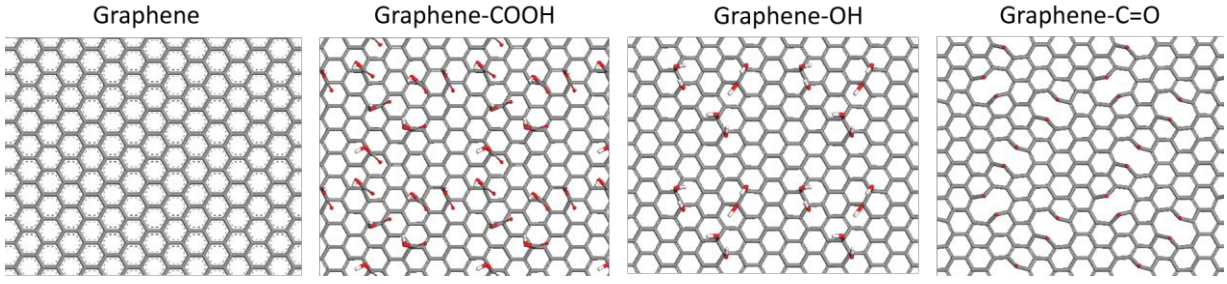

Figure 1. Pristine and functionalised graphene models with 10 % of functional groups

2.1.3. Models with different coverage percentages of hydroxyl groups

The influence of grafting density on the mechanical properties of graphene was studied by randomly grafting hydroxyl groups to the graphene structure in different percentages, 3.0 % and 7.0 %.

2.1.4. Models with different type of distribution of hydroxyl groups

The effect of the type of distribution of hydroxyl groups was assessed by comparing models with a single cluster, several small clusters and dispersed hydroxyl groups on the graphene. The study was performed for 3.0 % of grafting.

2.1.5. MD simulations

The initial structure was energy-minized and then equilibrated using a NVT ensemble for 100 ps and Berendsen thermostat with Velocity Verlet as the integration method. The condensed-phase optimized molecular potential for atomistic simulation studies (COMPASS) force field was used to model the interactions between atoms. This force field has previously been applied in MD simulations of carbon nanotubes and graphene.[2,4-6] In calculating the non-bonded potentials, the atom-based summation with a cut-off radius of 9 Å was used in the van der Waals summation and electrostatic interactions by Coulomb potential. All simulations were performed at 298 K at atmospheric pressure and timestep 1 fs. The cell was strained in intervals of 0.5 %, each followed by an equilibration step as described above, after which the stress was calculated based on the virial expression. The Young's modulus was obtained from the slope of the stress vs strain plots of the strained layers.

3. Results and discussion

3.1.1. Functional groups randomly dispersed

The Young's modulus for graphene models with dispersed functional groups are presented on Table 1. As expected and due to the sp^2 hybridized structure, pristine graphene obtained the highest value for Young's modulus, 1.35 TPa, which is close to what is reported in the literature.[2] From the obtained results it is obvious that the grafting of functional groups on the graphene layer has an influence on the mechanical properties. Both carboxyl and hydroxyl groups reduce respectively about 42 % and 47 % the Young's modulus. This can be explained by the change of the original sp^2 hybridized bonds between grafted and neighbouring carbon atoms to sp^3 in order to promote the grafting. This allows a larger rotation of the carbon atoms due to unsupported sp^3 bonds therefore decreasing the mechanical properties.[3,4] The difference between both functional groups may be attributed to the oxygen from the hydroxyl group being bonded directly to a carbon of the graphene surface, while the carboxyl functional group has a carbon-carbon bonding to the hexagonal structure. On the other hand, the carbonyl groups promote the complete breaking of a sp^2 bond between one neighbour atom of the grafted carbon creating a type of vacancy defect that decreases about 57 % the elastic modulus compared to pristine graphene.

Table 1. Parameters and data obtained from molecular dynamics simulations of graphene layers with oxygen containing functional groups. The volume is 50 302 $Å^3$.

	Graphene	**Graphene-COOH**	**Graphene-OH**	**Graphene-C=O**
No. Atoms	960	1 344	1 152	1 056
Young's modulus, *E* (TPa)	1.35	0.78	0.72	0.64

3.1.2. Functionalisation percentages of hydroxyl groups randomly dispersed

Graphene with grafted hydroxyl groups ranged from 3.0 % and 7.0 % functionalisation. A decrease on the Young's modulus with the increase of functionalisation was verified and is in agreement with work already published.[7]

Table 2. Comparison between different percentages of hydroxyl groups

	3.0 %	**7.0 %**
No. Atoms	1 024	1 092
Young's modulus, *E* (TPa)	0.77	0.71

3.1.3. Distribution of hydroxyl groups

Studies were performed only for 3.0 % grafting. Comparisons between randomly distributed groups, single cluster, and several clusters were made. The single cluster obtained the lowest Young's modulus for both percentages. The smaller clusters models on the other hand have less impact on the elastic modulus. In these four cases there is no obvious difference regarding the percentage of functionalisation. On the contrary, the randomly dispersed hydroxyl groups have a slightly larger decrease from 0.77 TPa to 0.72 TPa when increasing the functional-

isation. The consequences on graphene mechanical properties have proved to be dependent on the location, distribution and coverage of the functional groups as shown by Pei et al.[8]

Table 3. Comparison between different distributions of hydroxyl groups

	3.0 % of functional groups		
	Dispersed	**Cluster**	**Clusters**
No. Atoms	1 024	1 024	1 024
Young's modulus, *E* (TPa)	0.77	0.70	0.74

4. Conclusions

The mechanical properties have shown to be influenced by the presence of functional groups with the grafting promoting a change in hybridisation from sp^2 to sp^3. Carboxyl groups proved to influence the least the mechanical properties. On the other hand, carbonyl groups influence the most. A higher coverage density also means a decrease on the Young's modulus. A single large cluster has a higher influence on the mechanical properties of graphene than randomly distributed hydroxyl groups or even several smaller clusters.

Bibliography

1. Tsai J, Tu J. Characterizing mechanical properties of graphite using molecular dynamics simulation. *Mater Des*. 2010;31(1):194-199.

2. Jing N, Xue Q, Ling C, et al. Effect of defects on young's modulus of graphene sheets: A molecular dynamics simulation. *RSC Adv*. 2012;2(24):9124-9129.

3. Montazeri A, Ebrahimi S, Rafii-Tabar H. A molecular dynamics investigation of buckling behaviour of hydrogenated graphene. *Molecular Simulation*. 2015;41(14):1212.

4. Zheng Q, Geng Y, Wang S, Li Z, Kim J. Effects of functional groups on the mechanical and wrinkling properties of graphene sheets. *Carbon*. 2010;48(15):4315-4322.

5. Kulathunga DDTK, Ang KK. Modeling and simulation of buckling of embedded carbon nanotubes. *Computational Materials Science*. 2014;81:233-238.

6. Coto B, Antia I, Blanco M, et al. Molecular dynamics study of the influence of functionalization on the elastic properties of single and multiwall carbon nanotubes. *Computational Materials Science*. 2011;50(12):3417-3424.

7. Qin Z, Buehler M. Bioinspired design of functionalised graphene. *Molecular Simulation*. 2012;38(8-9):695-703.

8. Pei QX, Zhang YW, and Shenoy VB. Mechanical properties of methyl functionalized graphene: A molecular dynamics study. *Nanotechnology*. 2010;21(11):115709.

Performance of *Cassia fistula* Leaf-extract on Stainless Steel Corrosion in 0.5 M HCl

O.A. Omotosho,[1,*] J.O. Okeniyi,[1] A.S. Ogbiye,[2] O.B. Ajibola,[1] C.A. Loto[1,3]
[1]Mechanical Engineering Department, Covenant University, Ota, Nigeria
[2]Civil Engineering Department, Covenant University, Ota, Nigeria
[3]Chemical, Metallurgical and Materials Engineering Department, Tshwane University of Technology, Pretoria, South Africa
*e-mail: olugbenga.omotosho@covenantuniversity.edu.ng

Abstract:
In this study the performance of *Cassia fistula* leaf-extract on stainless steel corrosion in 0.5 M HCl medium was investigated. Different concentrations of *Cassia fistula* leaf-extract were employed in the acidic medium in which stainless steel specimens were immersed and corrosion rate was obtained through linear sweep voltametry instrumentation, at the ambient temperature of 28°C. Results showed that inhibition effectiveness of *Cassia fistula* leaf-extract on stainless steel corrosion in the test-environment tends to increase with increasing concentration of the natural plant extract. The 10 g/L *Cassia fistula* leaf-extract, which is the highest concentration of the leaf-extract employed in the study, exhibited optimal inhibition efficiency η = 88.46% on stainless steel corrosion in 0.5 M HCl.

Keywords: Linear sweep voltametry, corrosion rate, *Cassia fistula* leaf-extract, stainless steel, inhibition efficiency, acidic medium.

Introduction

Industrial surface treatment operation, oil well acidization, pickling and petrol refining operations utilize acidic solutions like hydrochloric acid (HCl) for their operation [1-3]. HCl has widespread industrial application with attendant corrosive effect on metal substrates. Though, the corrosive effects are most often combated with chemical inhibitors, this is already becoming outmoded because of the deleterious effect of many of the chemicals on the environment. Challenges associated with the use of chemical inhibitors are numerous [4-6]. Amongst such problems are contamination of plant and animal life, disposal burden, litigation and the expensive nature of a number of chemical inhibitors. In order to reduce dependence on the use of chemical inhibitors, a gradual shift of focus has been initiated by several researchers [7-15]. Thus, the focus is now on the use of green inhibitors obtained from plant extracts [3,12,16-21]. Chief amongst the reason for its utilization is the fact that it is cheap, easily available, sustainable, disposal and litigation free. Though, several research has been conducted using different inhibitors on stainless steel corrosion in acidic media [22-29], there is still paucity of studies on the use of green inhibitors on stainless steel in acidic media. Aside from this paucity of research effort in this study direction, is the fact that there appears to be no study yet on the utilization of *Cassia fistula* on stainless steel corrosion in HCl acid.

Stainless steel is known to have self healing properties that make it possible to form almost immediately a thin passive layer capable of protecting the metal. This protection often times is not enough to prevent certain aggressive aqueous acids like HCl from taking over the metal surface by attacking and destroying the film and rendering the metal surface bare for pitting corrosion attack which is a localized and insidious in nature [30-31]. The introduction of hetreoatoms containing green inhibitors that have the capability of donating lone electron pair is likely to facilitate the inhibition process [1,18,27]. Motivation for this study are drawn from the known fact that *Cassia fistula* leaf-extract contains phytochemicals like phenolics, flavonoid and proanthocyanidins [32] which are invariably made up of alcohol and carboxylic group that are also rich in lone pair electrons. This paper therefore investigates the performance of *Cassia fistula* leaf-extract on the corrosion degradation of stainless steel in HCl medium.

Materials and method

Stainless steel metal sheet were cut to a dimension of 1 cm by 1 cm with a guillotine. The metal surface was then treated in accordance with procedures stated in ASTM D2688-94 R99 [33] for treating stainless steel metal before corrosion experiments and then stored in a desiccator prior to the experimental usage. The chemical composition of the stainless steel material utilized for the study include: 15.12% Cr, 11.88% Ni and 67.51% Fe.

Fresh leaves of *Cassia fistula* (*C. fistula*) were obtained from Ota, Ogun State, Nigeria, and identified at the Forestry Herbarium, Ibadan, Nigeria, with voucher FHI No. 110261 assigned to the sample deposited at the Herbarium. The leaves of *C. fistula* were dried under conditioned atmosphere at 21°C before being pulverized using grinding machine. From these, *C. fistula* leaf-extract was obtained using procedure that had been detailed in studies [34-36].

Experimental procedure employed use of Model K47 corrosion cell system electrochemical cell kit having 3-electrode outlets from Princeton Applied Research®. The 3-electrode outlets used include reference electrode, EDT direct-ion double junction [6,37-38], graphite counter electrode and the stainless steel sample working electrode. Linear sweep voltametry (LSV) testing were then conducted at 28°C (ambient temperature) using DY2312 Digi-Ivy potentiostat connected to the 3-electrode outlet of the cell kit, in which the 1cm^2 bare surface area of the epoxy mounted steel sample exhibited contact with the test-solution. Test solution employed in the study include 0.5 M HCl in which different concentrations of *C. fistula* leaf extract were dissolved ranging from 0 g/L (the control sample) to 10 g/L in increments of 2 g/L. The LSV experiment, at a scan rate of 0.1 V/s from an anodic potential of +0.5 V to a cathodic potential of -1.0 V versus corrosion potential, gave readout of corrosion rate (*CR*) using the formula [39]:

$$CR = \frac{0.00327 \times i_{corr} \times eq.wt}{\rho_{ms}} \tag{1}$$

Where i_{corr} = corrosion current density (in μA/cm^2), ρ_{ms} = density of metallic sample (g/cm^3) and *eq.wt* = equivalent weight (g). From *CR*, inhibition efficiency, η (%), was estimated for each plant extract concentration from the equation [40-42]:

$$\eta = \left(1 - \frac{CR_{\text{sample with } C.\ fistula}}{CR_{\text{sample without } C.\ fistula}}\right) \times 100 \tag{2}$$

Results and discussion

The results of potentiodynamic polarization obtained from the LSV experiments, for stainless steel in 0.5 M HCl in the absence and presence of varying concentrations of *C. fistula*, are presented in Fig. 1. The plots in the figure include the potentiodynamic polarization curves in Fig. 1(a) as well as the anodic and cathodic Tafel slopes superimposed with the E_{corr} in Fig. 1(b), for the concentrations of the plant extract employed in the study. From the figure, it could be observed that the cathodic and anodic curves were both influenced in the experiments but that the cathodic curve exhibited more extensive influence. As could be seen from the E_{corr} plot in Fig. 1(b), the polarization curves in Fig. 1(a) drifted in the cathodic direction relative to the control sample as *C. fistula* leaf-extract concentration increased from 0 g/L to 6 g/L before the curves initiated drifts towards the E_{corr} of the control sample as the extract concentration increased further to 10 g/L. It is worth noting that cathodic potential, in the form of more negative E_{corr} relative to the E_{corr} of the control sample, was maintained from 2 g/L up to 8 g/L *C. fistula*, such that only the 10 g/L *C. fistula* exhibited slightly anodic E_{corr} of +0.005 V relative to the control.

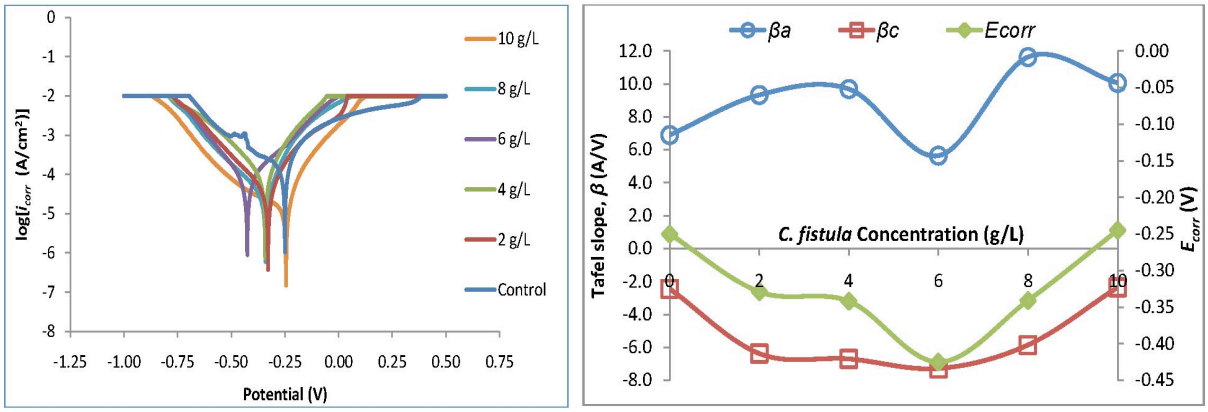

(a) (b)

Fig. 1. Plots of *C. fistula* effects on stainless steel corrosion in 0.5 M HCl medium (a) potentiodynamic polarization (b) Tafel slopes superimposed with E_{corr}

As could be observed from Fig. 1(b), trend of the plot of cathodic Tafel slope, β_c, exhibited better pattern with the plot of the E_{corr} than the trend of the plot of anodic Tafel slope, β_a, for the varying concentrations of *C. fistula* leaf-extract. For increasing *C. fistula* leaf-extract concentrations, β_c decreases as the E_{corr} decreases and increases as the E_{corr} increases. In comparison, β_a only decreased as the E_{corr} decreased in value from the 4 g/L *C. fistula* to the 6 g/L test-systems and only increased as the E_{corr} increased in value from the 6 g/L to the 8 g/L test-systems while it patterned otherwise relative to E_{corr} values for the other test-systems of *C. fistula* leaf-extract concentrations. These further corroborate the inference that the behaviour of stainless steel in the HCl medium, being stud-

ied, exhibited more of cathodic control in the presence of *C. fistula*, and from this it could be implied that cathodic hydrogen evolution mechanisms are under influence of the *C. fistula* leaf-extract. The shifts in corrosion potentials of stainless steel in the HCl medium exhibited highest displacement in E_{corr} value of –175 mV, i.e. in the cathodic direction, thus indicating that *C. fistula* leaf-extract is a cathodic type inhibitor [43-44].

Plot of the corrosion rate, estimated by the LSV instrument as per eq. (1), superimposed with the plot of corrosion inhibition efficiency, as per eq. (2), are presented in Fig. 2, for stainless steel in 0.5 M HCl in the absence and presence of different *C. fistula* leaf-extract concentrations. From the figure, it could be observed that corrosion rate values reduced drastically in the presence of the plant extract compared to corrosion rate from the control sample. Consequently, all the concentrations of *C. fistula* leaf-extract employed in the study inhibited stainless steel corrosion in the HCl medium.

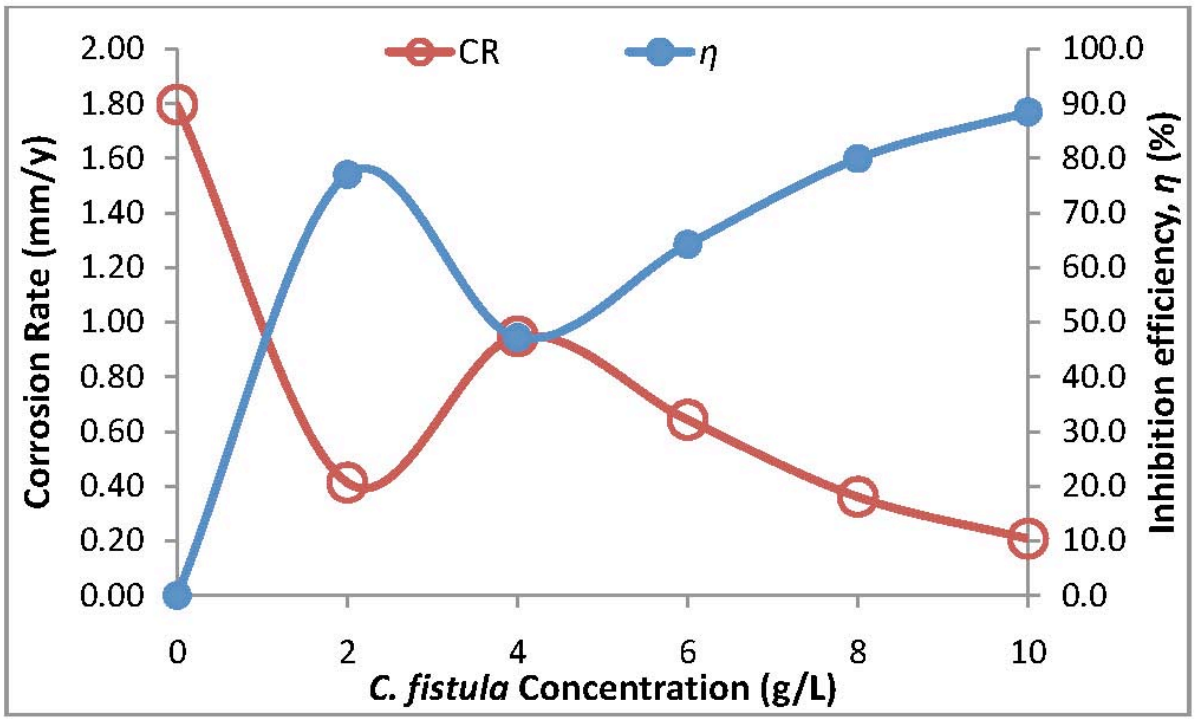

Fig. 2. Plots of corrosion rate and inhibition efficiency on stainless steel in 0.5 M HCl by *C. fistula* leaf-extract

With a slight exception, it could be deduced from Fig. 2 that the corrosion rate tends to decrease with increasing *C. fistula* concentration and/or inhibition efficiency tends to increase with *C. fistula* leaf-extract concentration. The exception to this was the performance from the 2 g/L *C. fistula* leaf-extract system, on stainless steel corrosion in 0.5 M HCl, which exhibited lower corrosion rate, and therefore higher corrosion inhibition efficiency effect, than what obtained from the 4 g/L and the 6 g/L *C. fistula* leaf-extract systems. In spite of this slight exception, the 10 g/L *C. fistula* concentration exhibited optimal inhibition efficiency, η = 88.46%, in the study, followed by the 8 g/L having η = 79.89%, with these trends being as a result of continuous increase in inhibition efficiency, η, from the 4 g/L to that of the 10 g/L *C. fistula* leaf-extract test-systems.

Conclusion

Performance of *C. fistula* leaf-extract has been studied in this paper using linear sweep voltametry instrument. The study established that all the different concentrations of *C. fistula* leaf-extract employed in the study inhibited stainless steel corrosion in 0.5 M HCl medium. With slight exception, observed in the 2 g/L *C. fistula* leaf-extract system, corrosion rate tends to reduce while inhibition efficiency tends to increase with increasing *C. fistula* concentration. By these, 10 g/L *C. fistula* leaf-extract exhibited optimal inhibition efficiency performance, η = 88.46%, on stainless steel corrosion in the 0.5 M HCL test-medium, followed in performance by the 8 g/L *C. fistula* leaf-extract that exhibited η = 79.89%.

References

1. M. Finsgar, J. Jackson, Corros. Sci. **86**, 17 (2014)
2. P. Rajeev, A.O. Surendranathan, C.S.N. Murthy, J. Mater. Environ. Sci. **3**, 856 (2012)

3. O.A. Omotosho, O.O. Ajayi, O.S. Fayomi, V.O. Ifepe, Int. J. Appl. Eng. Res. Dindigul, **2**, 85 (2011)
4. J.O. Okeniyi, A.P.I. Popoola, C.A. Loto, O.A. Omotosho, S.O. Okpala, I.J. Ambrose, Adv. Mater. Sci. Eng. **2015**, 540395 (2015)
5. J.O. Okeniyi, I.J. Ambrose, I.O. Oladele, C.A. Loto, A.P.I. Popoola, Int. J. Electrochem. Sci. **8**, 10758 (2013)
6. J.O. Okeniyi, O.M. Omoniyi, S.O. Okpala, C.A. Loto, A.P.I. Popoola, Eur. J. Environ. Civ. Eng. **17**, 398 (2013)
7. M. Scendo, J. Trela, Int. J. Electrochem. Sci. **8**, 9201 (2013)
8. O.A. Omotosho, O.O. Ajayi, ITB J. Eng. Sci. **44**, 77 (2012)
9. O.A. Omotosho, O.O. Ajayi, K.O. Ajanaku, V.O. Ifepe, J. Mater. Environ. Sci. **3**, 66 (2012)
10. O.A. Omotosho, O.O. Ajayi, O. Fayomi, V.O. Ifepe, Asian J. Appl. Sci. **5**, 74 (2012)
11. I.B. Obot, N.O. Obi-Egbedi, J. Electrochem. 40, 1977 (2010)
12. M. Lebrini, F. Robert, C. Roos, Int. J. Electrochem. Sci. **5**, 1678 (2010)
13. P.B. Raja, A.A. Rahim, H. Osman, K. Awang, Wuli Huaxue Xuebao/Acta Phys. Chim. Sin. **26**, 2171 (2010)
14. P.K. Kasthuri, A. Arulanantham, Asian J. Chem. 22, 430 (2010)
15. R. Rajalakshmi, S. Subhashini, S. Leelavathi, R.F. Mary, Orient. J. Chem. **24**, 1085 (2008)
16. J.O. Okeniyi, C.A. Loto, A.P.I. Popoola, O.A. Omotosho, in *Corrosion 2015 Conference & Expo*, Dallas, 2015, (NACE International, 2015) Paper No. 5636
17. O.A. Omotosho, O.O. Ajayi, O. Fayomi, O. Yussuff, Singap. J. Sci. Res. **2**, 14 (2012)
18. A.M. Al-Turkustani, Mod. Appl. Sci. **4**, 52 (2010)
19. E.I. Ating, S.A. Umoren, I.I. Udousoro, E.E. Ebenso, A.P. Udoh, Green Chem. Lett. Rev. **3**, 61 (2010)
20. G. Gunasekaran, L.R. Chauhan, Corros. Sci. **49**, 1143 (2007)
21. T. Jain, R. Chowdhary, P. Arora, S.P. Mathur, Bull. Electrochem. **21**, 23 (2005)
22. R. Herle, P. Shetty, S.D. Shetty, U.A. Kini, Port. Electrochim. Acta **29**, 69 (2011)
23. A.K. Satpati, P.V, Ravindran, Mater. Chem. Phy. **109**, 352 (2008)
24. A.B. Silva, S.M.L. Agostinho, O.E. Barcia, G.G.O. Cordeiro, E. D'Elia, J. Corros. Sci, 48, 3668 (2006)
25. A. Galal, N.F. Atta, M.H.S. Al-Hassan, Mater. Chem. Phy. **89**, 28 (2005)
26. A. Galal, N.F. Atta, M.H.S. Al-Hassan, Mater. Chem. Phy. **89**, 38 (2005)
27. S.A.M. Refaey, F. Taha, A.M. Abd El-Malak, Appl. Surf. Sci., 236, 175 (2004)
28. M. Abdallah, Mater. Chem. Phy. **82**, 786 (2003)
29. M. Abdallah, J. Corros. Sci. **44**, 717 (2002)
30. C.O.A. Olsson, D. Landolt, Electrochim. Acta **48**, 1093 (2003)
31. S. Bera, S. Rangarajan, S.V. Narasimhan, Corros. Sci. **42**, 1709 (2002)
32. T. Bahorun, V.S. Neergheen, O.I. Aruoma, Afri. J. Biotechnol. **4**, 1530 (2005)
33. ASTM D2688-94 R99, Standard Test Methods for Corrosivity of Water in the Absence of Heat Transfer (Weight Loss Methods). (ASTM International, West Conshohocken, PA, 2005)
34. J.O. Okeniyi, C.A. Loto, A.P.I. Popoola, Trans. Indian Inst. Met. **67**, 959 (2014)
35. J.O. Okeniyi, C.A. Loto, A.P.I. Popoola, Port. Electrochim. Acta **32**, 199 (2014)
36. S. Hameurlaine, N. Gherraf, A. Benmnine, A. Zellagui, J. Chem. Pharm. Res. **2**, 819 (2010)
37. J.O. Okeniyi, I.O. Oladele, O.M. Omoniyi, C.A. Loto, A.P. Popoola, Can. J. Civ. Eng. **42**, 408 (2015)
38. J.O. Okeniyi, I.O. Oladele, I.J. Ambrose, S.O. Okpala, O.M. Omoniyi, C.A. Loto, J. Cent. South Univ. **20**, 3697 (2013)
39. S.P., Canmet, in Techniques for Corrosion Monitoring, edited by L. Yang (Woodhead Publishing Limited, Cambridge, 2008)
40. J.O. Okeniyi, C.A. Loto, A.P.I. Popoola, Solid State Phenom. **227**, 185 (2015)
41. J.O. Okeniyi, C.A. Loto, A.P.I. Popoola, Energy Procedia **50**, 421 (2014)
42. S. Kumar, D.G. Ladha, P.C. Jha, N.K. Shah, Int. J. Corros. 2013, 819643 (2013)
43. Z.H. Tao, S.T. Zhang, W.H. Li, B.R. Hou, Corros. Sci. 51, 2588 (2009)
44. E.S. Ferreira, C.F. Giacomelli, F.C. Gicomelli, A. Spinelli, Mater. Chem. Phy. **83**, 129 (2004)

Electrical transport properties of an isolated single walled carbon nanotube aligned on an ST-cut quartz substrate

El-Hadi Sadki [1], Tohru Watanabe [2], Takahide Yamaguchi [2], and Yoshihiko Takano [2]

[1] Physics Department, United Arab Emirates University, PO. Box 17551, Al Ain, United Arab Emirates
[2] National Institute for Materials Science (NIMS), 1-2-1 Sengen, Tsukuba, Ibaraki 305-0047, Japan

ABSTRACT
In this proceeding, we introduce a technique for synthesizing an individual single walled carbon nanotube (SWNT) aligned on an ST-cut quartz single-crystal substrate, and demonstrate the measurement of its electrical transport characteristics. The SWNT is CVD synthesized from an optimized catalyst's size that yields just one individual SWNT suitable for electrical transport measurements. The temperature dependence of its electrical resistance is measured from room temperature down to few Kelvins.

Keywords
Single walled carbon nanotubes, ST-cut quartz, CVD

1. INTRODUCTION
Single walled carbon nanotubes (SWNTs) are promising materials to replace silicon for future electronic circuits and devices because of their unique electrical transport properties [1]. However, the main obstacle for this realization is the lack of control on the properties of the synthesized SWNTs and their exact positioning on substrates to make reliable and reproducible devices.

Recently, it has demonstrated that by using single-crystal ST-cut quartz as substrates to synthesize SWNTs on them by chemical vapor deposition (CVD) leads to highly aligned and long SWNTs that are very suitable for electronic device fabrication [2]. However, so far no electrical transport measurements have been conducted on an individual SWNT on these substrates because they are usually synthesized as arrays, and, hence, it is difficult to isolate just one SWNT for these measurements (See figure 1).

In this work, we introduce a technique for synthesizing an individual single walled carbon nanotube (SWNT) aligned on an ST-cut quartz single-crystal substrate, and demonstrate the measurement of its electrical transport characteristics. The SWNT is CVD synthesized from an optimized catalyst's size that yields just one individual SWNT suitable for electrical transport measurements. The temperature dependence of its electrical resistance is measured from room temperature down to few Kelvins and briefly discussed.

2. EXPERIMENTAL
The fabrication process for the synthesis of an individual SWNT, and the deposition of the electrical terminals on top of it, is summarized as follows. A patterned metallic foil is used as a shadow mask for the evaporation of the cobalt catalyst pads needed for the CVD growth of the SWNTs. The cobalt catalyst, with a thickness of 2 nm, is evaporated through the mask's pattern

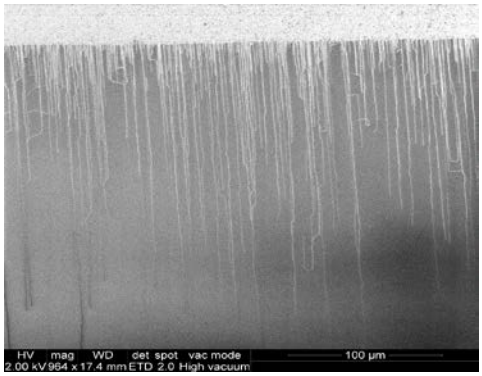

Figure 1. Scanning electron micrsocope (SEM) image of highly aligned single walled carbon nanotubes (SWNTs) on an ST-cut quartz substrate.

by an electron beam (EB) evaporator. The area of the Co-catalyst pad is optimized to yield to the growth of one individual long and aligned SWNT suitable for electrical transport measurements. After catalyst deposition, the SWNT is synthesized by thermal CVD method using a tube furnace. ST-cut quartz substrates (Hoffman Materials, Inc) are placed at the center of the downstream side of the furnace. A typical CVD process is as follows: Substrate is heated in a 200 sccm O_2 flow from room temperature to 900 ^oC for 30 minutes and let to settle for 5 minutes. Next, the O_2 flow is stopped and replaced by 300 sccm Ar flow for 10 mins. Then, a 200 sccm H_2 gas is flown for 10 mins. Finally, the H_2 gas is co-flown with 300 sccm CH_4 gas for 15 mins, which leads to a SWNT synthesis. Finally, the sample is left to cool-down to room temperature in a continuous H_2 flow.

Electrodes on the SWNT are also fabricated using shadow mask evaporation technique. The metal masks are prepared by the same method as of that used for catalyst pattern. Palladium (Pd) is selected as the material of the electrodes because of its low contact resistance to SWNTs [3]. The Pd electrodes, with a thickness of 50 nm, are EB evaporated in a four-terminal configuration, with a typical distance of 4.0 µm between adjacent electrodes. The electrical properties of the SWNT are measured from room temperature down to 2 K, using a physical properties measurement system (PPMS: Quantum Design Inc.) for the temperature control. Voltages of ~ ±1 V are applied by a voltage source through a 10 MΩ resistance connected in series with the sample, and the voltage is measured across the inner-electrodes on the sample by a voltmeter.

3. RESULTS AND DISCUSSION
Figure 2 (a) shows an SEM image of SWNTs synthesized from a catalyst pad of 100 x 10 µm in area. A lot of SWNTs are obtained

in this case, with average lengths of more than 100 μm. On the other hand, as shown in Figure 2 (b), if a catalyst pad of 10 x 2 μm is used, only one or a few SWNTs are obtained, with typically the emergence of an individual SWNT of more than 100 μm in length. Figure 2 (c) shows deposited electrodes on another SWNT synthesized from the same pad's dimensions of 10 x 2 μm.

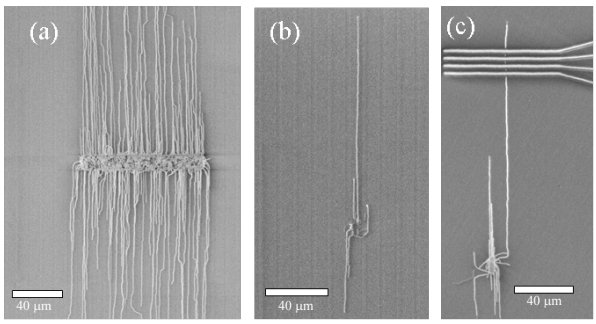

Figure 2. SEM images of SWNTs synthesized from different catalyst pads. Size of catalyst pad is 100 x 10 μm in (a), 10 x 2 μm in (b), and 10 x 2 μm in (c) with deposited metallic electrodes.

Figure 3 shows the result of the temperature dependence of the electrical resistance (normalized to its value at 300 K) of a SWNT measured with an electrical current of 10 nA. The nanotube has a diameter of 0.9 nm as measured by AFM.

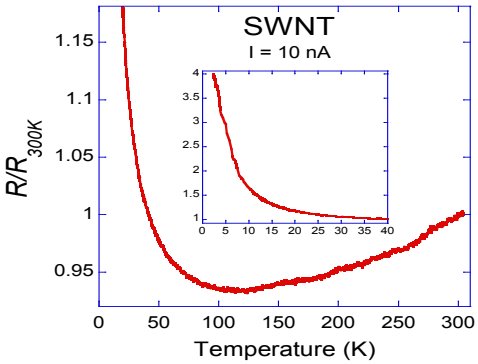

Figure 3. Temperature dependence of the electrical resistance of the nanotube (normalized to its value at 300 K). Inset shows the resistance in the low temperatures range. The electrical current is 10 nA in all measurements.

The SWNT's resistance decreases with decreasing temperature from room temperature down to about 120 K, and then it increases by decreasing temperature down to 2 K. At the lowest temperature of 2K, the resistance reaches about 4 times its room temperature value of 181 kΩ. The decrease in the resistance of the nanotube with decreasing temperature from room temperature down to about 120 K is attributed to its metallic nature [4]. To explain the "semiconducting-like" behavior of the resistance versus temperature below 120 K, it is noted that even "metallic" SWNTs can exhibit a "semiconducting" energy gap due their intrinsic curvature [5] and substrate effects [6]. Further studies are underway to investigate these properties of more individual SWNTs in this special configuration.

4. CONCLUSION

In conclusion, we have presented a technique for synthesizing an individual single walled carbon nanotube (SWNT) aligned on an ST-cut quartz single crystal substrate, and demonstrate the measurement of its electrical transport characteristics. The temperature dependence of its electrical resistance is measured from room temperature down to few Kelvins, and showed a decrease with decreasing temperature from room temperature down to about 120 K, and then an increase by decreasing temperature down to 2 K. Further studies are in progress to explain these properties.

5. ACKNOWLEDGMENTS

This study was supported by Nano-Integration Foundry (NIMS) in "Nanotechnology Platform Project" operated by the Ministry of Education, Culture, Sports, Science and Technology (MEXT), Japan. ESS would like to acknowledge the support from NIMS during his visit as a Guest Researcher.

6. REFERENCES

[1] Cao, Q. and Han, S.J. 2013. Single-walled carbon nanotubes for high-performance electronics. *Nanoscale*. 5, 19, 8852–8863. DOI= http://dx.doi.org/10.1039/C3NR02966B.

[2] Kang, S.J., Kocabas, C., Ozel, T., Shim, M., Pimparkar, N., Alam, M.A., Rotkin, S.V. and Rogers, J.A. 2007. High-performance electronics using dense, perfectly aligned arrays of single-walled carbon nanotubes. *Nat. Nanotechnol*. 2, 4, 230–236. DOI= http://dx.doi.org/10.1038/nnano.2007.77.

[3] Javey, A., Guo, J., Wang, Q., Lundstrom, M. and Dai, H.J. 2003. Ballistic carbon nanotube field-effect transistors. *Nature*, 424, 6949, 654–657. DOI= http://dx.doi.org/10.1038/nature01797.

[4] 26 Kane, C.L., Mele, E.J., Lee, R.S., Fischer, J.E., Petit, P., Dai, H., Thess, A., Smalley, R.E., Verschueren, A.R.M., Tans, S.J. and Dekker, C. 1999. Temperature-dependent resistivity of single-wall carbon nanotubes. *Europhys. Lett*, 41, 6, 683–688. DOI= http://dx.doi.org/10.1209/epl/i1998-00214-6.

[5] Kleiner, A. and Eggert, S. 2001. Band gaps of primary metallic carbon nanotubes. *Phys. Rev. B*, 63, 7, 073408 DOI= http://link.aps.org/doi/10.1103/PhysRevB.63.073408.

[6] Soares, J.S. and Jorio, A. 2012. Study of Carbon Nanotube-Substrate Interaction. *Journal of Nanotechnology*, 2012, 1-10. DOI= http://dx.doi.org/10.1155/2012/51273.

December 16, 2015

Dear Editor,

Please find enclosed our manuscript entitled **"Study of Interaction of 2-Mercaptobenzimidazole and Gold Atom for Self-Assemled Monolayers"** by Ourida Mahmoudi, Tarik Bordjiba, Mohamed-Abed Affoune that we wish to submit as a Proceeding. Our manuscript is dealing with the self-assembly of organic molecules at gold atom. The results of the present work give a new insight on self assembly of 2-Mercaptobenzimidazole molecules at metal surface.

We are looking forward to hearing from you soon.

Ourida Mahmoudi

8 mai 1945 University,
Guelma, Algeria
E-mail : Mahmoudi_o@yahoo.fr
Tel : (213) 6 62 43 73 70
Fax : (213) 37 20 72 68

Study of Interaction of 2-Mercaptobenzimidazole and Gold Atom for Self-Assemled Monolayers

Ourida Mahmoudi[123], Tarik Bordjiba[12 *] and Mohamed-Abed Affoune[3]
[1]*Departement of Chemistry, Badji-Mokhtar University, Annaba, Algeria*
Mahmoudi_o@yahoo.fr
[2]*Laboratery of Electrical Engineering of Guelma, 08th May 1945 University,Guelma, Algeria*
bordjiba_tarik@yahoo.ca
[c]*Departement of Process Engineering, 08th May 1945 University, Guelma, Algeria*
affoune2@yahoo.fr

Abstract:
The purpose of this work is to study the interaction of 2-Mercaptobenzimidazole and its adsorption on gold atom. The Density Functional Theory Study (DFT) calculations were performed on 2-Mercaptobenzimidazole (2MBI) and the complex: 2-Mercaptobenzimidazole-gold atom (2MBI-Au). The quantum chemical parameters of 2MBI and the complex: 2MBI-Au have been calculated. The considered quantum chemical parameters are: lengths bonds, angles bonds, optimization energy, binding energy, Mulliken atomic charges, energies of highest occupied molecular orbital (E_{HOMO}), the lowest unoccupied molecular orbital (E_{LUMO}), the energy difference (ΔE) between E_{LUMO} and E_{HOMO}. The complexation of 2MBI with Au atom modifies the quantum chemical parameters of the organic molecule. This study reveals that gold atom bonds with 2MBI molecule via sulfur atom.

Keywords:2-mercaptobenzimidazole, self-assembly, Adsorption, Density Functional Theory (DFT), Energy gap, Theoretical calculation, Gold.

1. Introduction

Recently, self-assembled monolayers (SAMs) have expected an immense interest due to their permanency and easy preparation [1]. The potential application of SAMs consists of several fields such as sensor fabrication, ion recognition,molecular electronics,studies of electron transfer kinetics, high density memory storage devices, biomolecular investigations, immobilization of biocatalysts, electrocatalytic studies ,mediation of electron transport across molecular filmsand corrosion protection. Self-assembled monolayers of aliphatic systems have been widely studied in the past years, whereas more recently the attention has focused on SAMs of aromatics and hetero-aromatics thiols by molecular electronics applications and by lithography to center on the ultra-short length level. Aromatic thiols SAMs are moreover attractive for the reason of very high electron density and intensive intermolecular interactions [1].
Among the hetero-aromatics thiols, the 2-mercaptobenzimidazole (2MBI) molecule, which is illustrated in Scheme1, has a simple thiolfunctionnel group that may be expected acting as the main chemisorption center.
Additionally, one or mutually of the two nitrogen atoms in the heterocyclic region ring may act as second center for interaction with the surface [2]. The 2MBI molecule could be present in two tautomeric forms [3] (Scheme1). The sulfur atom is protonated in the thiol form leaving two chemically dissimilar nitrogen heteroatoms one protonated and the other one deprotonated in difference in the thione form where mutually nitrogen atoms are protonated [2].

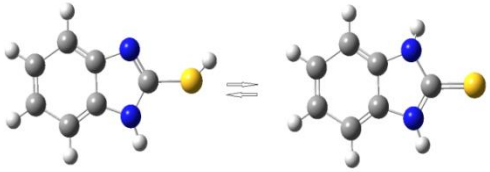

Scheme 1: Tautomerization of 2-mercaptobenzimidazole molecule

Most investigations employed gold as a substrate for adsorption of 2-mercaptobenzimidazole molecule because ordered gold films are easy to prepare [4]. Despite many experimental investigations on the structure Au-S bond in SAMs prepared of thiolate, the precise nature of the molecule-metal interface is still subject of discussion [5] and there is still insufficient acknowledged concerning the reactions provided SAMs from organosulfur compounds with metals [6].
In this context, we propose to study the adsorption of 2-mercaptobenzimidazole on gold atom with the intention to understand and evaluate the interaction between this molecule and the above mentioned metallic atom. We have used the density functional theory (DFT) [7] methods to determine the quantum chemical parameters such as the Mulliken charges, the highest occupied molecular orbital (E_{HOMO}) and the lowest unoccupied molecular orbital (E_{LUMO}) energies, the difference (ΔE) between E_{LUMO} and E_{HOMO} energy, total energies.

2. Computational details

Calculations have been completed by remedying to DFT methods via the Gaussian 09 W set of program. The 2MBI thiol molecule was built by using GaussView program. The geometry of obtained molecular was optimized and the calculations were performed PBE/LANL2DZ level.

In the optimized structure of the 2MBI molecule, the hydrogen atom that bonds by sulfur was substituted by metallic atom Au in order to simulate the adsorption of the 2MBI molecule on gold atom. The resulting structures were optimized by using the DFT method at the PBE/LANL2DZ level. The obtained structure is denoted as 2MBI-Au.

Computations of quantum chemical parameters such as: E_{HOMO}, E_{LUMO}, $\Delta E = E_{LUMO} - E_{HOMO}$, were done at DFT technique level by PBE/LANL2DZ for the organic molecule 2MBI and studied organometallic complex 2MBI-Au for study the adsorption of 2MBI molecule on gold atom.

3. Results and discussion

3.1. Molecular geometry

Fig. 1 shows the structure of 2MBI, 2MBI-Au before and after structure optimization. The drawn 2MBI is presented in Fig. 1a and the optimized structure of 2MBI is illustrated in Fig.1b. The main lengths and angles of bonds for the optimized structure of 2MBI are presented in Table 1. In the optimized structure of 2MBI component, S-H, S-C, C-N bond lengths and the HSC, SCN, CNH, SCN(H) bond angles were 1.386A°, 1.816, 1.337, 93.310, 125.658, 126.401, 120.803 using PBE/LANL2DZ. The results of theoretical calculations of this study are in agreement with experimental and theoretical parameters reported in the literature [11-13] as mentioned in Table1.

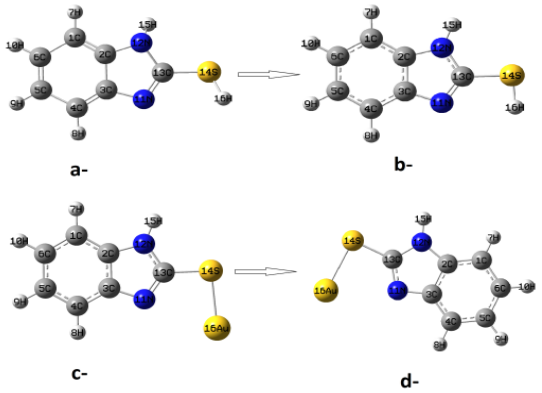

Fig. 2: The structure of 2MBI and substituted hydrogen of 2MBI with Au (a-, c-).
The optimized structures of 2MBI and substituted hydrogen of 2MBI with Au (b-, d-).

Table 1. Comparative selected bond's lengths (A°) and bond's angles (°) for 2MBI experimental and theoretical calculations by DFT.PBE/LANL2DZ.

Bond's lengths	Theoretical Calculations PBE/LANL2DZ	Experimental Reference (17,18)	Theoretical Calculations Reference (19)
H(16)—S(14)	1.386	----------	1.373
S(14)—C(13)	1.816	1.684, 1.6715	1.812
C(13)—N(11)	1.337	1.362, 1.365	1.393
C(13)—NH(12)	1.399	1.383	-------
NH(12)—H(15)	1.018	1.050	1.010
NH(15)—C(2)	1.408	1.383, 1.389	
N(11)—C(3)	1.419	----------	
C(2) —C(3)	1.437	1.384, 1.400	
H(16)—N(11)	2.692	----------	
Bond's angles	**Theoretical Calculations PBE/LANL2DZ**	**Experimental Reference (17,18)**	**Theoretical Calculations Reference (19)**
H(16)—S(14)—C(13)	93.310	----------	94.200
S(14)—C(13)—N(11)	125.658	126.800, 127.200	
C(13)—N(11)—C(3)	106.828	111.000 ,110.400	
C(13)—N(12)—H(15)	126.401	121.000	126.200
C(13)—NH(12)—C(2)	104.557	110.400, 110.000	
S(14)—C(13)—NH(12)	120.803	126.800, 127.200	120.700
N(11)—C(13))—N(12)	113.544	----------	113.300

The atom of Au as shown in Fig. 1c substituted the hydrogen atom, which binds by sulfur in the optimized structure of 2MBI molecule. This is in order to simulate the adsorption of 2MBI molecule on the gold atom.

After the optimization of this structure (Fig. 1d), the Au atom is still bonded to the 2MBI through the sulfur atom. The main lengths and angles of bonds for the optimized structure of 2MBI are shown in Table 2. We note that the optimized S-Au, S-C, C-N bond lengths and the optimized AuSC, SCN, CNH, SCN(H) bond angles in the complex 2MBI-Au were 2.403A°, 1.810A°, 1.349A°, 94.195°, 125.901°, 126.281°, 120.759°, respectively. A little variation is observed on the important bond lengths and angles comparatively with component 2MBI.

Table 2.Comparative selected bond's lengths (A°) and bond's angles (°) for 2MBI, 2MBI-**Au**, by DFT.PBE/LANL2DZ.

Bond's lengths\Complex	2MBI	2MBI-**Au**
M(16)—S(14)	1.386[H-S Bonded]	2.403[Au-S] Bonded
S(14)—C(13)	1.816	1.810
C(13)—N(11)	1.337	1.349
C(13)—NH(12)	1.399	1.397
NH(12)—H(15)	1.018	1.018
NH(12)—C(2)	1.408	1.409
N(11)—C(3)	1.419	1.416
C(3)—C(2)	1.437	1.438
M(16)—N(11) M:H,Au	2.692[H-N] unbonded	2.929[Au-N] unbonded
Bond's angles\Complex	2MBI	2MBI-**Au**
M(16)—S(14)—C(13)	93.310	94.195
S(14)—C(13)—N(12)	125.658	125.901
C(13) —N(12)—C(2)	106.828	105.040
C(13)—N(12)—H(15)	126.401	126.281
C(13)—N(11)—C(3)	104.557	106.807
S(14)—C(13)—NH(12)	120.803	120.759
N(11)—C(13))—N(12)	113.544	112.330

3.2. Optimization energy and Binding energy

From the optimized structures of 2MBI, 2MBI-Au, several parameters can be explored. Optimization energy, binding energy and lengths between sulfur or nitrogen and gold ('S' or 'N' and Au) are presented in Table 3.
The binding energy of the 2MBI thiol molecule to the gold atom was determinate by using the following eq [14]:

$$E_{binding} = -E_{adsorption} \quad (1)$$

Where $E_{adsorption}=E_{2MBI-M} - (E_{atom}+E_{2MBI})$
And E_{2MBI-M} is the total energy of the complex (metal atom and the molecule 2MBI); E_{atom} is the energy of the metal atom and E_{2MBI} is the energy of the molecule 2MBI.

Table 3. Optimisation energy of complexes and metal atom, adsorption energy, binding energy and length betweensulfur 'S' or nitrogen 'N' and metal ' M'.by DFT . PBE/LANL2DZ.

Complex 2MBI—M M:H or Au	Optimisation energy of Complex 2MBI- M (a.u.)	Optimisation energy of metal atom Au (a.u.)	Adsorption Energy(a.u.)	Binding Energy(a.u.)	Distance S—M(H) (A°)	Distance N—M(H) (A°)
2MBI S—H	-389.44409				1.386 bonded	2.692 Unbonded
2MBI-Au S—Au	-524.77041	-135.41879	-0.09247	0.09247	2.403 bonded	2.929 Unbonded

The results given in Fig. 1c-d show that gold atom is still bonded to the 2MBI by sulfur even after optimization. The bond length between S and Au atoms is equal to 2.403A°, the total energy optimization is evaluated to -524.77041a.u. and binding energy is equal to 0.09247a.u.
The bonding of gold to sulfur atom of 2MBI can be explained by the electronic configuration of gold atom. The electronic configuration of gold atom Au(0) is described as $[Xe]4f^{14}5d^{10}6s^1$ [15],the last orbital $6s^1$ is occupied by one electron, so this atom can donate and accept one electron to become more stable as shown in the following configuration$[Xe]4f^{14}5d^{10}s^2$. Furthermore, the donate electron is given to sulfur atom of the molecule 2MBI this is why after optimization of the structure of the complex 2MBI-Au, gold is still bonded with sulfur of the molecule 2MBI. The frees electrons of gold atom Au(0) and the sulfur atom S of the molecule 2MBI can be the origin of the covalent bond. From the work of [16] while —SH is adsorbed on the gold surface; the hydrogen atom is removed and the powerful Au—S covalent bond is subsequently constitute.
In this study, there are two different donor atoms, sulfur and nitrogen. According to [17-19], when bi-functional ligands with two donors atoms are utilized, the gold atom will bind to these ligands through the atom with the higher donor strength according to the order Si~P> C > S >Cl> N > O > F. In other words, the two bi-functional are coordinated to Au through the P and S atoms but not N, since P and S are better soft donor than N [20].
Additionally, the gold is frequently defined as a soft metal and consequently, mightbe estimated to prefer soft donor ligands for example S and C to the hard donor ligands such as those bonding throughN or O [21]. Consequently, it was usually supposed that Au (I) would not efficiently coordinate to a donor N atom [17-19].

3.3. Mulliken atomic charges

Only the main charges were considered, so the charges above the two nitrogen atoms, sulfur, carbon linked to the sulfur and metallic atoms are given in Table 4.

Table 4. Calculated Mulliken atomic charges of 2MBI and 2MBI-Au by DFT . PBE/LANL2DZ.

2MBI	2MBI-Au
16 H 0.151	16 Au 0.068
14 S -0.004	14 S 0.038
13 C -0.178	13 C -0.058
12 N -0.405	12 N -0.411
11 N -0.028	11 N -0.059

The PBE/LANL2DZ method is used to estimate the Mulliken atomic charges for the organic molecule and the complex. For the optimized molecule 2MBI, the sulfur atom carries a weak negative charge -0.004 and the two nitrogen atoms carry the negative charges whose values are -0.028 for deprotonated nitrogen and -0.405 for nitrogen bonded with hydrogen. These results show that sulfur and nitrogen atoms are sites, which can give electrons to the substrate atom to donate a coordination type further reaction with these atoms that have free of bond, and these can undergo doublet electrons. It was demonstrated that local electron densities are indispensable in several chemical responses and physicochemical characteristics of compounds [22].Adsorption of organic molecules can be explicated by the interaction of these molecules with metal atom.

For the calculated Mulliken atomic charges of complex 2MBI-Au, the charges distribution has changed comparatively to that one of the molecule 2MBI. Therefore, we distinguished an increase of atomicchargeofthe exocyclic sulfur,which becomes 0.038 instead of -0.004 after being linked to gold atom whose charge is positive and equal to 0.068. It have been cited that in the formation process of SAM from thiols (*i.e*., R-SH), the hydrogen atom is take away during SAM development, and a covalent sulfur-gold bond is created displaying extremely small charge transfer between metal and sulfur [23].The nitrogen atoms charges decreased strongly for deprotonated nitrogen whose value charge change into -0.059 and weakly for nitrogen bonded with hydrogen whose charge value becomes -0.411 and this will be explained by attracter inductive effect for sulfur to equilibrium the charge of gold. The molecule 2MBI is adsorbed to gold atom via sulfur through the thiol tautomer.

Atomic charge of the sulfur for the 2MBI-Au is higher than the sulfur atom in the molecule 2MBI. This is due to the aim to equilibrate charge between sulfur and gold in the complex 2MBI-Au.

Moreover, we distinguish that adsorption of organic molecule on metal atom change the charge distribution of the organic molecule 2MBI.

3.4. HOMO, LUMO, Gap energy and dipole moment

The calculated quantum chemical parameters E_{HOMO}, E_{LUMO}, gap energy and total energy for the organic molecule 2MBI, 2MBI with hydrogen atom removed denoted 2MBI˙, the complex 2MBI-Au, is presented in Table 5.

The results obtained by PBE/LANLD2Z method show that the 2MBI˙ displays the higher value of HOMO energy (E_{HOMO}= -5.62581 eV) than that one of the molecule (E_{HOMO}= -5.38029 eV). Additionally, the gap energy of the 2MBI˙ (3.62654 eV) is lower than that of the molecule (3.94356 eV). These indicating the capacity of the 2MBI˙ to donate electrons to the convenient metal atom more than the molecule 2MBI.

The high E_{HOMO} values show that the molecule has a trend to offer electrons to convenient acceptor with low energy vacant molecular orbital. Increasing values of the E_{HOMO} make easy adsorption by influencing the transport process through the adsorbed film; low E_{LUMO} energy indicates the capacity of the molecules to accept electrons [23].

Low values of the energy band gap ΔE allows better adsorption and facilitate bond with metal atoms, for the reason that the energy to extract an electron from the last occupied orbital will be low [25]. Cherry et *al*.[26] have used the notion of LUMO-HOMO energy gap in developing theoretical models which is able to explicate the structure and conformation barriers in various molecular systems [27] qualitatively. According to the results of this study, the 2MBI˙ is more reactive than 2MBI, this is why we have chosen substitute directly hydrogen atom of 2MBI by one atom of the gold. Additionally, the dipole moment μ of the 2MBI˙ is higher than that one of the organic molecule 2MBI (table 5). This confirms that 2MBI is adsorbed under 2MBI with hydrogen atom removed form and covalent bond is then formed [16].

Table 5. Calculated total energy, orbital energies E_{HOMO} , E_{LUMO} and gap energy ΔE for 2MBI, 2MBI· and 2MBI-**Au**.

2MBI and 2MBI-Au	E_{HOMO} (eV)	E_{LUMO} (eV)	Gap energy ΔE (eV)	Total energy (a.u.)	Total energy (eV)
2MBI	-5.38029	-1.43705	3.94356	-389.44409	-10597.55271
2MBI$^{\bullet}$	-5.62581	1.99926	3.62654	-388.83676	-10581.02601
2MBI-Au	-5.88514	-3.77675	2.10839	-524.77041	-14280.00523

Furthermore, increasing values of E_{HOMO} and μ make possible adsorption by facilitate the transport process through the adsorbent layer [28]. Nevertheless, the elevate component polarity (dipole moment equal to 2.3748 and 5.5144 for 2MBI and 2MBI·, respectively) makes easy electrostatic interaction between the electric field due to the metal charge and the electric moment of these compounds, and participates to their better adsorption [29,30].

From table 5, we can seen that the replacement of hydrogen atom in 2MBI by gold, change the levels of energies (HOMO, LUMO, gap energy) and the energy gap ΔE of the complex formed 2MBI-Ausmaller than the gap energy of 2MBI. This offers this complex to react with the second functionality.

The forms HOMO and LUMO of the organic molecule 2MBI and complex under investigations are showing in Fig.2

According to [32] it is recognized that the reactivity of a molecule depends on molecular orbital distribution. HOMO is habitually related with the electron donate aptitude of a molecule, while LUMO shows its aptitude to win electrons [32].It can be seen from Fig. 2(a) that the densities of both HOMO and LUMO of 2MBI molecule are comparatively the same on the entire area of the molecule due to the distribution of π-electron cloud on the molecule. The HOMO density is elevated in the region close to the imidazole ring and thiol group, which is qualified to the existence of electron pairs in the N atoms of imidazole ring [32] and sulfur atom. Therefore, the preferableactive centers for giving electrons in 2MBI are principally situated inside the regions approximately nitrogen and sulfur atoms. The LUMO densities on the C–C area in 2MBI molecule are elevated, demonstrating that the favored active centers for wining electrons are principally situated inside this area [32].

For the 2MBI-Au complex Fig. 2(b), the HOMO density is delocalized and essentially distributed on the imidazole section and on the sulfur atom while the population of LUMO is localized on the gold atom and it is obviously superior than that on the imidazole section and sulfur. It is rational to deduce that the sulfur in 2MBI molecule acts as the principal site to offer electrons and generate the coordinated bond with unoccupied d-orbital's of the gold atom.

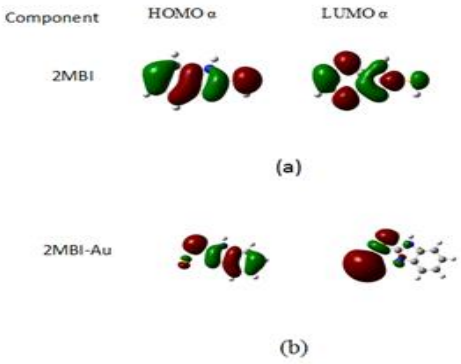

Fig. 3: Frontier molecular orbital diagrams of 2MBI and 2MBI-Au.
a-Orbital diagrams HOMO(α) and LUMO(α) of optimized 2MBI.
b-Orbital diagrams HOMO(α) and LUMO(α) of optimized 2MBI-Au.

From these figures, it can be concluded that the compound 2MBI is adsorbed on the gold via sulfur by using the benzimidazole-thiol moiety, which contains the heteroatoms and aromatic rings. Moreover, the presence of metal atoms affects significantly the molecular orbitals.

4. Conclusions

To summarize, the study of interaction of 2-Mercaptobenzimidazole and its adsorption on gold atom has performed by means of Density Functional Theory Study (DFT). The quantum chemical parameters of 2MBI and the complex 2MBI-Auhave been calculated. The considered quantum chemical parameters are: length's bonds, angles bonds, optimization energy, binding energy, Mulliken atomic charges, E_{HOMO}, E_{LUMO}, $\Delta E = E_{LUMO} - E_{HOMO}$. The complexation of 2MBI with Au atom modifies the quantum chemical parameters. This study

reveals that gold bonds with 2MBI molecule via sulfur atom. In the future work, we will study the interaction of 2-Mercaptobenzimidazole and its adsorption on the cluster of gold and thin films of several metals.

References

1. R.K. Shervedani, F. Yaghoobi, A. Hatefi-Mehrjardi, S.M. Siadat-Barzoki,Electrochimica Acta **53**, 418 (2008).
2. C.M.Whelan, M.R.Smyth, C.J.Barnes, N.M.D.Brown, C.A.Anderson, J Applied Surf. Sci.**134**, 144 (1998).
3. M.Gholami, I.Danaee, M.H.Maddahy and M.RashvandAvei, Ind. Eng. Chem. Res.**52**, 14875 (2013).
4. N.Mohtat, M.Byloos, M.Soucy, S.Morin, M.Morin, J. Electroanal. Chem.**484**, 120 (2000).
5. J.Kučera and A.Gross, Langmuir**24**, 13985 (2008).
6. X.Jiang, D.A.Bruzewicz, M.M.Thant, G.M.Whitesides, Anal. Chem.**76**, 6116 (2004).
7. B.Liu, F.Chen, L.Zheng, J.Ge, H.Xi and Y.Qian, R.S.C. Advances **3**, 15075 (2013).
8. G.R.Form, E.S.Raper, T.C.Downie, J Acta Cryst. B**32**, 345 (1976).
9. K.Ravikumar, K.C.Mohan, M.Bidyasagar and G.Y.S.K.Swamy, J. Chem. Crystallogr. **25**, 325 (1995).
10. N.AlHokbany, I.Aijammaz, Open Journal of Inorganic Chemistry**1**, 23 (2011).
11. A.Kokalj, Langmuir **26**, 14582 (2010).
12. Y.Liu, M.Li, Y.Suo, Surface Science **600**, 5117 (2006).
13. Y.Shundong, C.Dai, J.Weng, Q.Mei, Q.Ling, L.Wang and W.Huang, J. Phys. Chem. A**115**, 4535 (2011).
14. H.Schmidbaur, Gold: Progress in chemistry, biochemistry and technology, John Wiley, New York, 1999.
15. A.Grohman and H.Schmidbaur, Comprehensive organometallic chemistry II, Vol 3, In: E.W.Abel, F.G.Stone and Wilkinson G (eds) Elsevier Pergamon, Oxford, 1995.
16. H. E.Abdou, A. A.Mohamed and Jr. JP. Fackler, Gold(I) nitrogen chemistry. In F. Mohr (Ed) Gold chemistry: applications and future directions in the life sciences, Copyright c WILEY-VCH Verlag GmbH and Co KGaA, Weinheim, pp1–45, 2009.
17. M. C.Cimeno, A.Laguna, Comprehensive coordination chemistry II, Vol 6, In Silver and Gold: McJ.A.Cleverty, T.J.Meyer, D.E.Fenton (Eds) Elsevier Pergamon, Oxford, UK, 2004.
18. F.A.Cotton, G.Wilkinson and P.Gaus, Basic Inorganic Chemistry, Vol 3, John Willy and Sons, New York, 1995.
19. M.Karelson, V.S.Lobanov, Chem. Rev.**96**, 1027 (1996).
20. G.Heimel, L.Romaner, E.Zojer, J.-L.Brédas, M. Muccini and E.A.Meulenkamp, Organic optoelectronics and photonics III, Proceeding of SPIE, 6999, 699919, 2008.
21. G.Bereket, C. Ogretir and A. Yurt, J. Mol. Struct. (THEOCHEM) **571**, 139 (2001).
22. W.Cherry, N.Epiotis and W.T.Borden, Acc. Chem. Res.**10**, 167 (1977).
23. M.Şahin, G.Gece, F.Karci, S.Bilgic, Journal of Applied Electrochemistry **38**, 809 (2008).
24. M. Lagrene´e, B. Mernari, N. Chaibi, M. Traisnel, H. Vezin, F. Bentiss, Corros. Sci.**43**, 951 (2001).
25. K.F.Khaled, K.Babic´-Samaradzija, N.Hackerman, Appl Surf. Sci.**240**, 327 (2005).
26. O. Benali, L. Larabi, M. Traisnel, L. Gengembre, Y. Harek, Applied Surface Science **253**, 6130 (2007).
27. F.Zhang, Y.Tang, Z.Cao, W.Jing, Z.Wu and Y.Chen, Corros. Sci. **61**, 1 (2012).

The effects of temperature and pH on swelling of stimuli-sensitive hydrogels

A.D. Drozdov, C.-G. Sanporean, J. deC. Christiansen

Department of Mechanical and Manufacturing Engineering, Aalborg University, Aalborg 9220, Denmark

Abstract

A model is developed for equilibrium swelling by thermo- and pH-sensitive gels. Constitutive equations are derived by means of the free energy imbalance inequality for an arbitrary three-dimensional deformation with finite strains. Adjustable parameters are found by fitting observations on N-isopropylmethacrylamide-sodium methacrylate and N-vinylcaprolactam-sodium itaconite copolymer gels under unconstrained swelling. Quantitative agreement is demonstrated between the experimental data and results of simulation.

1. Introduction

Hydrogels are three-dimensional networks of polymer chains connected by covalent bonds, physical cross-links and hydrogen bonds. When a dry gel is immersed into a water bath, it swells retaining structural integrity and ability to withstand large deformations. Stimuli-sensitive gels demonstrate substantial and reversible changes in their degree of swelling in response to weak changes in temperature, pH, ionic strength, and electric field [1,2]. Thermo- and pH-responsive hydrogels have recently become a focus of attention as they demonstrate potential for ``smart'' applications ranging from micro- and nano-carriers for targeted delivery of drugs, peptides, and proteins to sensing systems for bio-analytes and carriers for enzyme immobilization, to multifunctional soft actuators, to antimicrobial active packaging systems, to devices for removal of organic dye contaminants from wasted water.

Thermo-sensitive gels form an important class of stimuli-responsive materials whose degree of swelling is strongly affected by temperature. When these gels are immersed into an aqueous solution at temperature T below some critical temperature T_*, they swell noticeably. When temperature exceeds T_*, most of the water molecules are expelled. The temperature T_* is referred to as the volume phase transition temperature (VPTT).

Multistimuli-responsive gels (whose water uptake is affected by temperature and pH) are prepared by incorporation of pH-sensitive moieties (anionic or cationic functional groups) into a thermo-responsive network. Their thermal response is associated with hydrophilic-hydrophobic transformation of segments, and their pH-sensitivity is attributed to ionization of functional groups, which induces electrostatic repulsion of bound changes and growth of ionic pressure. Observations show that for a given pH, degree of swelling Q decreases monotonically with temperature below an apparent VPTT $T_{*\mathrm{app}}$ and becomes unaffected by T above $T_{*\mathrm{app}}$. An increase in molar fraction ρ of ionic monomers (i) leads to a pronounced increase in equilibrium degree of swelling Q at temperatures below $T_{*\mathrm{app}}$, (ii) induces shift of the apparent VPTT $T_{*\mathrm{app}}$ to higher values, (iii) causes noticeable changes in the shape of $Q(T)$ diagrams below $T_{*\,\mathrm{app}}$, but (iv) weakly affects degree of swelling at temperatures exceeding $T_{*\,\mathrm{app}}$.

The objective of this study is twofold: (i) to develop constitutive equations for multistimuli-responsive anionic gels subjected to swelling, and (ii) to find material constants in these relations by fitting equilibrium swelling curves under unconstrained water uptake.

2. Constitutive model

A gel is treated as an interpenetrating three-phase continuum composed of a solid phase (polymer network), water, and solute (mobile ions). Transport of solvent and solutes through the network is modeled as their diffusion affected by (i) the electric field formed by mobile and bound ions, (ii) dissociation of functional groups, and (iii) self-ionization of water.

Macro-deformation of a gel coincides with that of the polymer network and obeys the molecular incompressibility condition. The reference (stress-free) configuration of the network differs from its initial configuration. Transition from the initial state into the reference state is driven by (i) hydrophilic-hydrophobic transformations of segments and (ii) ionization of functional groups attached to polymer chains. The deformation gradient for elastic deformation $\boldsymbol{F}_e$ (which describes transformation of the reference configuration into the actual configuration) is connected with the deformation gradient for macro-deformation $\boldsymbol{F}$ by the multiplicative decomposition formula $\boldsymbol{F}=f^{1/3}\boldsymbol{F}_e$, where the coefficient of volume expansion of polymer network f is treated as a linear function of degree of ionization of chains α and concentration of hydrophilic segments η.

The strain energy density of the polymer network is described by the neo-Hookean formula $W=½\,G\,[(J_{e1}-3)-\ln J_{e3}]$, G stands for shear modulus, and J_{e1}, J_{e2}, J_{e3} are the principal invariants of the Cauchy-Green tensors for elastic deformation. More sophisticated expressions for W were developed in [3] and validated by comparison with observations under multi-axial deformations in [4].

The specific energy of mixing of water molecules and segments of chains is determined by the Flory-Huggins (FH) formula, where the FH parameter χ decreases linearly with concentration of hydrophilic segments η. The specific energy of mixing of mobile ions is described by the conventional formula for dilute solutions. To calculate the specific energy of mixing of ionized and non-ionized functional groups, we suppose that the number of sites (per chain) to be occupied by non-ionized and ionized functional groups α_{max} is proportional to degree of swelling Q.

Governing equations for equilibrium unconstrained swelling of thermo- and pH-sensitive gels are derived in [5]. They involve (i) an analog of the Henderson-Hasselbach (HH) equation for degree of ionization of chains [6,7,8], (ii) an equation for volume fraction of H^+ ions inside a gel (a consequence of the electro-neutrality conditions and the Donnan equilibrium conditions), (iii) an equation for concentration of hydrophilic segments η [9,10] that accounts for the effect of ionization of chains on hydrophilic-hydrophobic transformation, (iv) an equation for equilibrium degree of swelling Q analogous to the balance equation for osmotic pressure developed in [7].

3. Fitting of observations

We analyze equilibrium swelling of N-isopropylmethacrylamide-sodium methacrylate (NIPMA-SMA) [11] and N-vinylcaprolactam-sodium itaconite (VCL-SI) [12] copolymer gels. Samples with various molar fractions of ionic monomers ρ were prepared by cross-linking copolymerization in aqueous solutions. Water

uptake tests were performed at temperatures ranging from 20 to 80 °C in deionized water. Swelling diagrams are depicted in Figure 1 which demonstrates quantitative agreement between the observations and results of simulation.

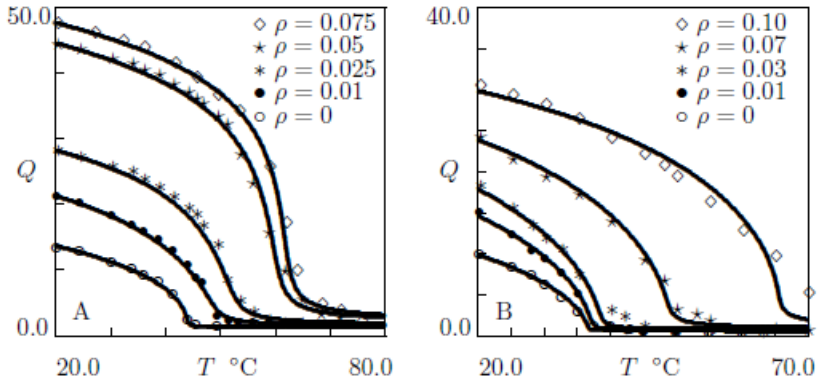

Figure 1: Degree of swelling *Q* versus temperature *T*. Symbols: experimental data on NIPMA-SMA (A) and VCL-SI (B) gels with molar fractions ρ of ionic monomers [11,12]. Solid lines: results of simulation.

The effect of temperature on degree of ionization of chains is illustrated in Figure 2, which reveals that α reaches its ultimate value α=1 far below T_*, decreases monotonically with temperature, and adopts small values above VPTT.

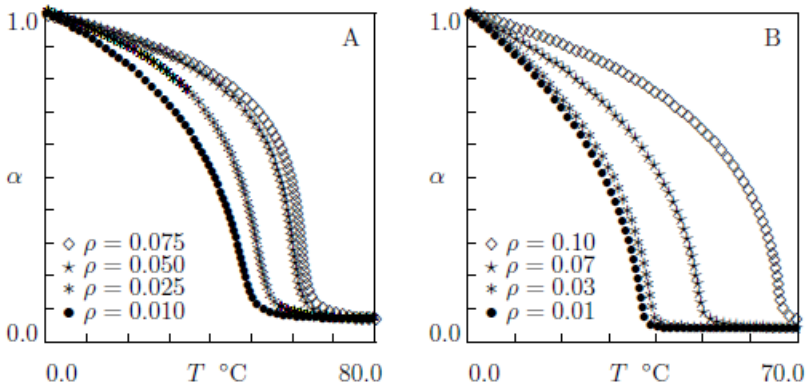

Figure 2: Degree of ionization α versus temperature *T*. Symbols: results of simulation for NIPMA-SMA (A) and VCL-SI (B) gels with molar fractions ρ of ionic monomers.

Figure 3 reveals that the FH parameter χ increases with temperature and approaches its ultimate value χ_*=½ at $T>T_*$. At all temperatures, χ belongs to a narrow interval between -4 and ½. For VCL-SI gels, χ decreases with ρ, whereas for NIPMA-SMA gels, it reveals a non-monotonic dependence in the interval of temperatures between 15 and 45 °C.

4. Conclusions

A model is developed for the elastic response of a thermo- and pH-sensitive gel subjected to swelling. Material constants are found by fitting observations on NIPMA-SMA and VCL-SI copolymer gels. It is

demonstrated that (i) the model ensures good agreement with observations, and (ii) adjustable parameters change consistently with molar fraction of ionic monomers.

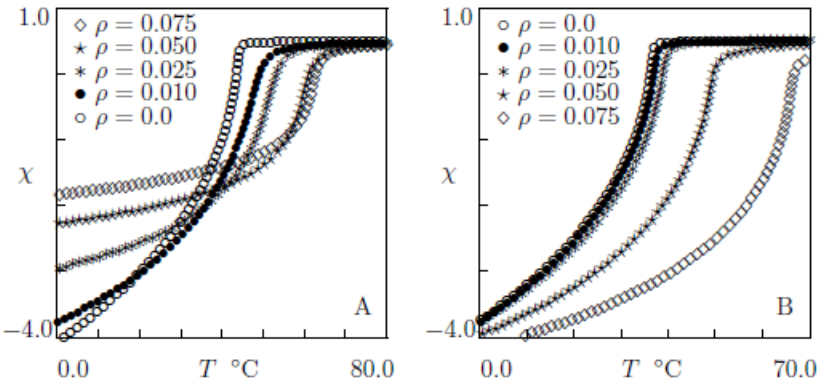

Figure 3: The FH parameter χ versus temperature *T*. Symbols: results of simulation for NIPMA-SMA (A) and VCL-SI (B) gels with molar fractions ρ of ionic monomers.

Acknowledgement

Financial support by the European Commission through FP7-NMP programme (project 314744) is gratefully acknowledged.

References

1. S.-K. Ahn, R.M. Kasi, S.-C. Kim, N. Sharma, Y. Zhou, Soft Matter 4 (2008) 1151-1157.

2. E.M. White, J. Yatvin, J.B. Grubbs, J.A. Bilbrey, J. Locklin, J. Polym. Sci. B: Polym. Phys. 51 (2013) 1084-1099.

3. A.D. Drozdov, J.deC. Christiansen, Int. J. Solids Struct. 50 (2013) 1494-1504.

4. A.D. Drozdov, J.deC. Christiansen, Int. J. Solids Struct. 50 (2013) 3570-3585.

5. A.D. Drozdov, C.-G. Sanporean, J. deC. Christiansen, Eur. Polym. J. 73 (2015) 278-296.

6. A.D. Drozdov, J.deC. Christiansen, Phys. Rev. E 91 (2015) 022305.

7. A.D. Drozdov, J.deC. Christiansen, J. Chem. Phys. 142 (1915) 114904.

8. A.D. Drozdov, J.deC. Christiansen, Modeling Simul. Mater. Sci. Eng. 23 (2015) 055005.

9. A.D. Drozdov, Eur. Phys. J. E 37 (2014) 93.

10. A.D. Drozdov, Acta Mech. 226 (2015) 1283-1303.

11. A. Fomenko, H. Pospisil, Z. Sedlakova, J. Plestil, M. Ilavsky, Phys. Chem. Chem. Phys. 4 (2002) 4360-4367.

12. M. Ilavsky, G. Manytbekov, K. Bouchal, L. Hanykova, Polym. Bull. 43 (1999) 109-116.

Solution electrospinning of particle-composite fibres

Lasse Christiansen and Peter Fojan
Aalborg University, Department of Physics and Nanotechnologies
Skjernvej 4, 9220 Aalborg E, Denmark

Keywords: Electrospinning, composite fibres, Poly(ethylene oxide) , aerogel particles

Introduction

Electrospinning is a simple and fast way to produce nano- and microfibers. By applying high voltage to a droplet of solution or polymer melt, fibre mats can be produced(1). These mats are porous in the micrometre domain, and have a high surface area to volume ratio(2).

Other materials with an even higher surface area to volume ratio are aerogels, which is highly porous with pore sizes in the nanometre range. The high surface to volume ratio makes it a good agent for gas sensors amongst other applications(3). The major drawback of these particles is their mechanical weakness(4). To counteract their brittle nature, they can be embedded into a scaffold for some applications. The brittleness can be drastically decreased by forming a particle/polymer composite, but the overall porosity of the material should not be compromised.

The method of choice to retain the porosity of the material on different scales (micro and nano) can be electrospinning. Aerogel and polymer can form a solution, and be processed into thin fibres. In this way, a membrane porous both on the micro- and nano- scale can be produced.

In the presented study, solution electrospinning of silica aerogel-polymer blends into composite fibres has been investigated, as a way to embed silica aerogel particles in a 3D mesh. The maximum polymer-silica weight-ratio yielding stable fibres has been determined. The morphology of the spun fibres at different weight ratios has been investigated, and the flowrate dependence of the fibre diameter was evaluated for polymer solutions with high particle contents. The self-supporting abilities of these fibres are discussed.

Materials and methods

Polymer and silica aerogel particles were added into a beaker and gently mixed. Then ethanol, followed by deionised water, was added under stirring. Solutions contained 1.5g polymer, 30ml ethanol and 30ml demineralised water and a varying amount of silica aerogel.

Electrospinning was performed on an electrospinning setup from Y-Flow. The relative humidity of the electrospinning encasing was kept at 20%. The needle collector distance was kept at a constant 15cm. Voltage on the needle was 9kV, and the flowrate was between 0.25ml h^{-1} to 2.0ml h^{-1}. After electrospinning, the produced samples were characterised with optical microscopy and scanning electron microscopy(SEM).

Results and Discussion

Six solutions were created. Their weight ratios (w/w) between polymer and silica aerogel particles were 1:1, 1:2, 1:4, 1:6, 1:8 and 1:9.

The fibres spun from solutions with w/w 1:1 to 1:6 all have a pearl-chain shape, where a particle was located in the fibre, with some distance of thin polymer fibre in between the separated particles. The length of polymer fibre between the particles tends to drop with increased particle concentration in the spinning solution

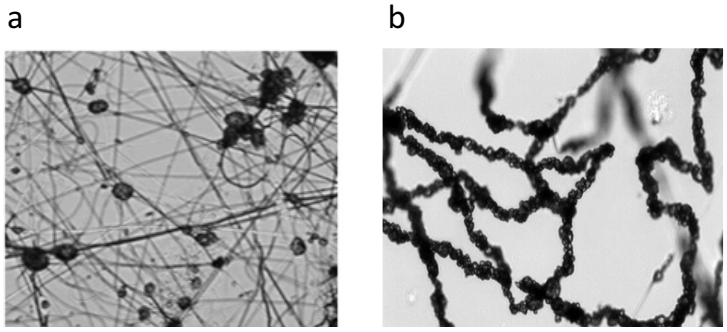

Figure 1 – Microscopy images fibres spun form solutions with polymer/silica aerogel w/w a) 1:1 and b) 1:8.

The fibre morphology changes drastically from between solutions with w/w 1:6 and 1:8. By electrospinning the later, fibres containing closely packed particles are formed. This change can be attributed to a very low amount of polymer available to form fibres. Instead, the silica aerogel particles touch each other, and pack the particles closely in the fibre. Images of fibres spun from solution with w/w 1:1 and 1:8 can be seen in figure 1.

Even though particles are more dominant or equal by weight in all solutions, the polymer fibre is still the dominant species. This is due to the relatively low amount of polymer used to create a thin fibre, with diameters in the nanometre range. The particles, on the other hand, are spherical and generally have a much larger diameter than the fibres. For solutions with w/w 1:8, the amount of particles becomes too high that fibres between the particles can be formed. Instead, the polymer glues the silica aerogel particles together.

These close packed fibres were analysed with SEM to obtain more detailed information on the fibre morphology. Solution 5 fibres were spun at flow rates ranging from 0.25 ml/min to 2 ml/min. With increased flowrates, the average fibre diameter increased from 13 um to 41 um. These fibres are presented in figure 2. The increase in diameter with flowrate corresponds with the general electrospinning theory of polymer solutions(5).

When the solutions were spun for a longer time period, fibre mats were formed. By spinning a 1:8 w/w solution onto a line over a prolonged period of time, a 3D structure was formed. This structure was strong enough to sustain its own weight. The obtained structure represents an enhancement of the mechanical properties of silica aerogel particles, through embedding them into a fibre matrix. Hence, the method has proven to embed silica aerogel particles into a solid polymer fibre matrix, able to support itself. The self-supporting particle/polymer fibres are presented in figure 4. The self-supporting fibres have been electrospun with a line needle movement of 10 mm/s, and a flowrate of 2 ml/h.

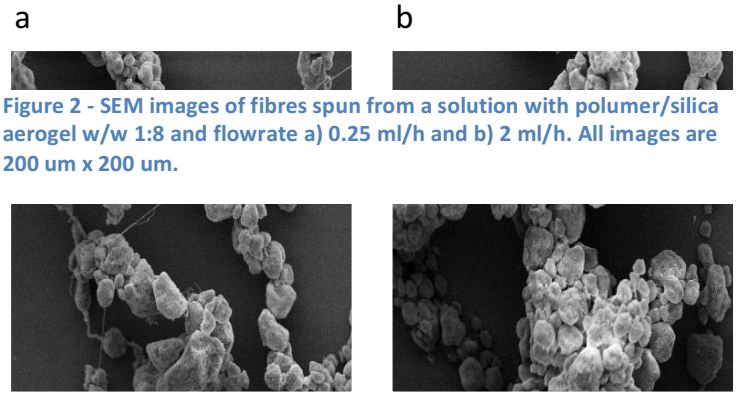

Figure 2 - SEM images of fibres spun from a solution with polumer/silica aerogel w/w 1:8 and flowrate a) 0.25 ml/h and b) 2 ml/h. All images are 200 um x 200 um.

Electrospinning of solutions with w/w 1:9 did not produce stable fibres. Instead, a polymer/particle powder was obtained. The particle concentration was too high for the polymer to hold the silica aerogel particles together, and was therefore not forming stable fibres.

Conclusion

Polymer/silica aerogel particle composite fibres have been produced with polymer/particle weight ratios from 1:1 to 1:8. Above this limit, no stable fibres were obtained. Fibres spun from solutions with w/w between 1:1 and 1:6 had a structure of single aerogel particles with polymer fibres in between.

Fibres spun with w/w 1:8 formed a fibre with closely packed aerogel particles. The general trend observed was that the fibre diameter increased with flowrate. Furthermore electrospinning of a solution with w/w 1:9 was attempted. This did not produce stable fibres, implying that the amount high amount of particles could not be hold together by the polymer.

1. Li D, Xia Y. Electrospinning of nanofibers: reinventing the wheel? Adv Mater. 2004;16(14):1151–70.
2. Gibson P, Schreuder-Gibson H, Rivin D. Transport properties of porous membranes based on electrospun nanofibers. Colloids Surf Physicochem Eng Asp. 2001;187:469–81.
3. Ayers MR, Hunt AJ. Molecular oxygen sensors based on photoluminescent silica aerogels. J Non-Cryst Solids. 1998;225:343–7.
4. Woignier T, Phalippou J, Hdach H, Larnac G, Pernot F, Scherer GW. Evolution of mechanical properties during the alcogel-aerogel-glass process. J Non-Cryst Solids. 1992;147:672–80.
5. Fridrikh SV, Yu JH, Brenner MP, Rutledge GC. Controlling the Fiber Diameter during Electrospinning. Phys Rev Lett. 2003;90(14):144502(4).

The Canonical Method of Nonholonomic Constraints

Khaled I. Nawafleh[1]

Applied Physics Department, Tafila Technical University, Jordan

Abstract

We discuss an extension of the Hamilton-Jacobi theory to nonholonomic mechanics with a particular interest in its application to exactly integrating the equations of motion. The major advantage of our result is that it provides us with a method of integrating the equations of motion just as the unconstrained Hamilton-Jacobi theory does.

1. Introduction

Nonholonomic mechanics describes the motion of systems whose restrictions on velocities do not arise from the constraints on the configuration space. The construction of Hamilton-Jacobi partial differential equations (HJPDEs) for nonholonomic constrained systems is of prime importance:The Hamilton-Jacobi theory provides a bridge between classical and quantum mechanics; it implies that quantum mechanics should reduce to classical mechanics in the limit $\mathbf{h} \to 0$. The Hamilton-Jacobi method is an alternative approach for solving problems of singular systems in the same manner as for regular systems.

2. Hamilton-Jacobi Treatment

A nonholonomic mechanical system is given by a Lagrangian function:

$$L = L(q_i, \dot{q}_i, t) \qquad i=1,2,\ldots,n \tag{1}$$

subject to a family of *m* nonholonomic constraint functions:

$$f_\alpha(q_i, \dot{q}_i) = 0 \qquad \alpha = 1,2,\ldots,m \tag{2}$$

We assume that the constraints $f_\alpha(q_i, \dot{q}_i)$ are linear in the velocities.

The equations of motion for a mechanical system with Lagrangian (1) and constraints (2) are given by the Lagrange-d'Alembert principle as:

$$\frac{d}{dt}\left(\frac{\partial L}{\partial \dot{q}_i}\right) - \frac{\partial L}{\partial q_i} = \lambda_\alpha \frac{\partial f_\alpha}{\partial \dot{q}_i} \tag{3}$$

The usual Hamiltonian *H(q,p)* for any dynamical system is given by

$$H(q_i, p_i, t) = p_i \dot{q}_i - L(q_i, \dot{q}_i, t) \tag{4}$$

The equations of motion followed by this Hamiltonian are obtained as:

$$\dot{q}_i = \frac{\partial H}{\partial p_i} \qquad \dot{p}_i = -\frac{\partial H}{\partial q_i} + \lambda_\alpha \frac{\partial f_\alpha}{\partial q_i} \tag{5}$$

The standard formulation of the Hamilton–Jacobi problem for a Hamiltonian system is based on the generating function *S(q,t):*

$$\frac{\partial S}{\partial t} + H(q_i, p_i, t) = 0 \tag{6}$$

Assume that there exists a solution of the Hamilton–Jacobi equation of the form

$$S = S(q_1, q_2, \ldots q_n; \alpha_1, \alpha_2, \ldots, \alpha_n, t) \tag{7}$$

[1] knawaflehh@yahoo.com

Making use of Canonical transformations, we can set:

$$\frac{\partial S}{\partial \alpha_i} = \beta_i \tag{8}$$

Next, Separation of variables for S may be obtained as:

$$S(q_1, q_2, ...q_n; \alpha_1, \alpha_2, ..., \alpha_n, t) = S_1(q_1, \alpha_1) + S_2(q_2, \alpha_2) + ... + S_n(q_n, \alpha_n) \tag{9}$$

After obtaining S, the Hamiltonian is obtained as:

$$H = -\frac{\partial S}{\partial t} \tag{10}$$

The Hamilton's equations of motion are given by:

$$\dot{q}_i = \frac{\partial H}{\partial p_i} \qquad \dot{p}_i = -\frac{\partial H}{\partial q_i} + \lambda_\alpha \frac{\partial f_\alpha}{\partial q_i} \tag{11}$$

Its worth to mention that the advantage of this method is that, in spite of the difficulties to solve a partial differential equation instead of an ordinary differential one, in many cases it works, being an extremely useful tool, indeed, in these cases the method provides an immediate way to integrate the equations of motion.

3. Illustrative Example

Consider the Lagrangian

$$L = \frac{1}{2}(\dot{x}^2 + \dot{y}^2 + \dot{z}^2) \tag{12}$$

subject to nonholonomic constraint:

$$f = \dot{z} - x\dot{y} \tag{13}$$

The Lagrange-d'Alembert equations of motion:

$$\frac{d}{dt}\left(\frac{\partial L}{\partial \dot{q}_i}\right) - \frac{\partial L}{\partial q_i} = \lambda \frac{\partial f}{\partial \dot{q}_i} \tag{14}$$

gives

$$\ddot{x} = 0 \qquad \ddot{y} = -\lambda x \qquad \ddot{z} = \lambda \tag{15}$$

Now we can solve for $x(t), y(t), z(t)$ as follows:

$$x = \alpha_1 t + \beta_1 \qquad y = \alpha_2 Ln\left(x + \sqrt{1+x^2}\right) + \beta_2 \qquad z = \alpha_3 \sqrt{1+x^2} + \beta_3 \tag{16}$$

The Hamilton-Jacobi formalism of the above equations can be obtained as:

$$\beta_1 = x - \alpha_1 t = \frac{\partial S_1}{\partial \alpha_1} \qquad \beta_2 = y - \alpha_2 Ln\left(x + \sqrt{1+x^2}\right) = \frac{\partial S_2}{\partial \alpha_2} \qquad \beta_3 = z - \alpha_3 \sqrt{1+x^2} = \frac{\partial S_3}{\partial \alpha_3} \tag{17}$$

Solving equations simultaneously, we obtain:

$$S(x, y, z, \alpha_1, \alpha_2, \alpha_3, t) = \alpha_1 x + \alpha_2 y + \alpha_3 z - \frac{1}{2}\alpha_1^2 t - \frac{1}{2}\alpha_2^2 Ln\left(x + \sqrt{1+x^2}\right) - \frac{1}{2}\alpha_3^2 \sqrt{1+x^2} \tag{18}$$

The generalized momenta are:

$$p_x = \frac{\partial S}{\partial x} = \alpha_1 - \frac{\alpha_2^2}{2}\frac{1}{\sqrt{1+x^2}} - \frac{\alpha_3^2}{2}\frac{x}{\sqrt{1+x^2}} \qquad p_y = \frac{\partial S}{\partial y} = \alpha_2 \qquad p_z = \frac{\partial S}{\partial z} = \alpha_3 \tag{19}$$

These can be inverted as:

$$\alpha_1 = p_x + \frac{\alpha_2^2}{2}\frac{1}{\sqrt{1+x^2}} + \frac{\alpha_3^2}{2}\frac{x}{\sqrt{1+x^2}} \qquad \alpha_2 = p_y \qquad \alpha_3 = p_z \tag{20}$$

With these results the Hamilton-Jacobi function becomes:

$$H = -\frac{\partial S}{\partial t} = \frac{1}{2}\alpha_1^2 \tag{21}$$

Inserting the value of α_1 :

$$H = \frac{1}{2}\left[p_x + \frac{p_y^2 + xp_z^2}{2\sqrt{1+x^2}}\right]^2 \tag{22}$$

The generalized equations of motion:

$$\dot{x} = \frac{\partial H}{\partial p_x} = \left[p_x + \frac{p_y^2 + xp_z^2}{2\sqrt{1+x^2}}\right] \tag{23}$$

$$\dot{y} = \frac{\partial H}{\partial p_y} = \left[p_x + \frac{p_y^2 + xp_z^2}{2\sqrt{1+x^2}}\right]\left(\frac{p_y}{\sqrt{1+x^2}}\right) \tag{24}$$

$$\dot{z} = \frac{\partial H}{\partial p_z} = \left[p_x + \frac{p_y^2 + xp_z^2}{2\sqrt{1+x^2}}\right]\left(\frac{xp_z}{\sqrt{1+x^2}}\right) \tag{25}$$

$$\dot{p}_x = -\frac{\partial H}{\partial x} + \lambda\frac{\partial f}{\partial \dot{x}} \qquad \dot{p}_y = -\frac{\partial H}{\partial y} + \lambda\frac{\partial f}{\partial \dot{y}} \qquad \dot{p}_z = -\frac{\partial H}{\partial z} + \lambda\frac{\partial f}{\partial \dot{z}} \tag{26}$$

After Simplifications:

$$\dot{x} = \alpha_1 \qquad \dot{y} = \frac{1}{\sqrt{1+x^2}} \qquad \dot{z} = \frac{x}{1+x^2} \tag{27}$$

$$\dot{p}_x = 0 \qquad \dot{p}_y = -\lambda x \qquad \dot{p}_z = \lambda \tag{28}$$

In comparison, we see that these equations are equivalent to those obtained by the Lagrange-d'Alembert principle.

4. Conclusion

In conclusion, using the Hamilton-Jacobi (HJ) scheme, we have formulated the problem of nonholonomic constrained system building on the work suggested by me and others with a particular interest in the application to exactly integrating of the equations of motion. In particular we formulated the theorem so that the technique of separation of variables applied as in the unconstrained theory.

We illustrated how this procedure works for the free particle motion and we show that the equations of motion that obtained by the Hamilton-Jacobi methods are equivalent to those obtained by the Lagrange-d'Alembert principle.

An important aspect of the theory of nonholonomic constraints is its relation with quantum mechanics. We expect that the overall results obtained in this work will provide the groundwork for quantizing nonholonomic systems. Thus, any discussion in this direction in the future should take this into account.

References

1. Rabei, E. M. and Guler, Y. Physical Review A, **46** (1992) 3513-3515.
2. Rabei, E. M., Nawafleh K.I. and Ghassib H. B. Phys. Rev. A66, 024101 (2002) 1-4.
3. Khaled I. Nawafleh, Eqab M. Rabei and Humam B. Ghassib, Int. Journ. Mod. Phys. A **19** (2004) 347-354.
4. Eqab M. Rabei, Khaled I. Nawafleh and Humam B. Ghassib, *Journal of Dynamical Systems and Geometric Theories*, 2 (2004) 1-6.
5. Khaled I. Nawafleh, Eqab M. Rabei and Humam B. Ghassib, *Turkish Journal of Physics*. 29 (2005) 151-162.
6. V.I. Arnol'd, Mathematical methods of classical mechanics, 2nd edition, Springer, 1989.

$C_5H_{11}NO_2S$ Effect on Concrete Steel-Reinforcement Corrosion in Industrial/Microbial Simulating Environment

J.O. Okeniyi,[1,*] A.O. Abioye,[1] Z.C. Adikpewun[1], A.A. Otesanya,[1] M.D. Eleshin[1], O.O. Gabriel,[1] O. Adeoye[1]
[1]Mechanical Engineering Department, Covenant University, Ota, Nigeria
*e-mail: joshua.okeniyi@covenantuniversity.edu.ng

Abstract:
This paper investigates the effect of $C_5H_{11}NO_2S$ (Methionine) on steel-reinforcement corrosion in concrete immersed in 0.5 M H_2SO_4, simulating industrial/microbial environment. For this, corrosion rate test-data were obtained by linear polarization resistance instrument from duplicates of steel-reinforced concrete samples immersed in the corrosive medium for 84 days experimental period and the obtained test data subjected to statistical distribution analyses as per ASTM G16-95 R04. While the analyzed results showed that there was no statistically significant difference from test-data obtained between the duplicated concrete samples, the different admixtures of $C_5H_{11}NO_2S$ employed in the study reduced corrosion rate in their admixed concrete compared to the control specimen without admixture. By this, 0.25% $C_5H_{11}NO_2S$ admixture (per weight of concrete mixing cement) exhibited optimal inhibition efficiency of 87.95±7.64% on the corrosion of reinforcing steel embedment in the concrete immersed in the industrial/microbial simulating environment.

Keywords: Methionine admixture, steel-rebar corrosion, industrial/microbial simulating-environment, statistical tests of significance, corrosion inhibition efficiency.

1. Introduction

Steel-reinforcement corrosion is a major deterioration problem affecting structural strength and service-life durability of steel-reinforced concrete material and for which safety risks, induced repairs and maintenance for averting in-service failure of structural members generate cost-intensive economic and social impacts globally [1-8]. The use of corrosion inhibitor admixture in concrete has been identified as an easily applicable, economical and highly effective approach for protecting concrete steel-reinforcement (steel-rebar) from corrosion degradation and for attaining durability of steel-reinforced concrete [1-2,9-11]. This constitutes research needs on the effectiveness of materials that could be used for inhibiting reinforcing steel corrosion in concrete developed for aggressive service-environments, especially that involving acidic sulphate medium usually prevalent in industrial (acid rain) or microbial (biogenic sulphate oxidizing) environments [12-14].

Motivation for this study had been especially drawn from the consideration that $C_5H_{11}NO_2S$ (Methionine) has been noted to be effective at inhibiting corrosion of iron, the highest elemental composition in reinforcing steel, in acidic environment [15]. However, there is dearth of study in which $C_5H_{11}NO_2S$ has been employed as admixture for inhibiting steel-rebar corrosion in physically cast concrete immersed in acidic sulphate medium, i.e. industrial/microbial environment. In this paper, therefore, the effect of $C_5H_{11}NO_2S$ (Methionine) on the corrosion inhibition of steel-reinforcement in concrete immersed in 0.5 M H_2SO_4 medium, an environment that had also been employed for simulating industrial/microbial environment in studies [10,14,16-17], was investigated.

2. Experimental

The 12 mm diameter reinforcing steel employed in this study was cut into 190 mm rods of specimen for each of which surface preparation was done as prescribed by ASTM G109-99a [18] and described in [4,14]. The samples of steel-reinforced concrete used for the study were cast according to standard procedure prescribed in ASTM C192/192M-02 [19] and that had been described in reported works [4,13]. As per [19], $C_5H_{11}NO_2S$ concentrations for the study were admixed in duplicates [20-21] to the samples, during casting. The $C_5H_{11}NO_2S$ admixed concentrations in the samples were varied from 0% (for the blank samples) in increment of 0.083% up to 0.417% i.e. wt% of the cement employed for casting each concrete paste. These totaled 12 steel-reinforced concrete samples for the study. 150 mm length of the reinforcing steel was centrally placed in each of the freshly cast concrete samples with the remaining 40 mm covered with self-adhesive tape [22] and bolted at one end for electrochemical connection.

Each 100 mm × 100 mm × 200 mm steel-reinforced concrete sample was immersed lengthwise in bowls containing the 0.5 M H_2SO_4 test-medium, the industrial/microbial simulating-environment. From this, corrosion rate, *CR*, measurements were obtained using 3-electrode, Model MS1500, LPR Data Logger (Metal Samples®) [23-24] in seven days interval for 84 days, which gave 13 data points of corrosion rate measurement for each sample. As prescribed by ASTM G16-95 R04 [25], the measured test-data were subjected to the statistical analyses of the Normal and Weibull distribution fittings using Kolmogorov-Smirnov goodness-of-fit statistics for ascertaining

the distribution function that describes the electrochemical test-data better than the other [14,23-24,26]. Also, significance of corrosion rate differences between duplicates of concrete samples having similar concentration of $C_5H_{11}NO_2S$ admixture was tested by the student's *t*-test statistics both at equal variance, homoscedastic, and at unequal variance, heteroscedastic, assumptions [13,20]. Based on these, corrosion inhibition efficiency, η, by the different concentrations of $C_5H_{11}NO_2S$ admixtures employed in the study was modeled from [3,23]:

$$\eta = \frac{CR_{\text{blank sample}} - CR_{\text{admixed sample}}}{CR_{\text{blank sample}}} \times 100 \quad (1)$$

3. Results and discussion

Results of the statistical models of mean corrosion rate by the Normal and the Weibull distributions for each sample of steel-reinforced concrete are presented in Fig. 1(a). Also, the *p*-values from the Kolmogorov-Smirnov goodness-of-fit analyses of test-data scatter like the Normal and the Weibull distributions were plotted for each sample, with linear plot for indicating threshold of significance, in Fig. 1(b).

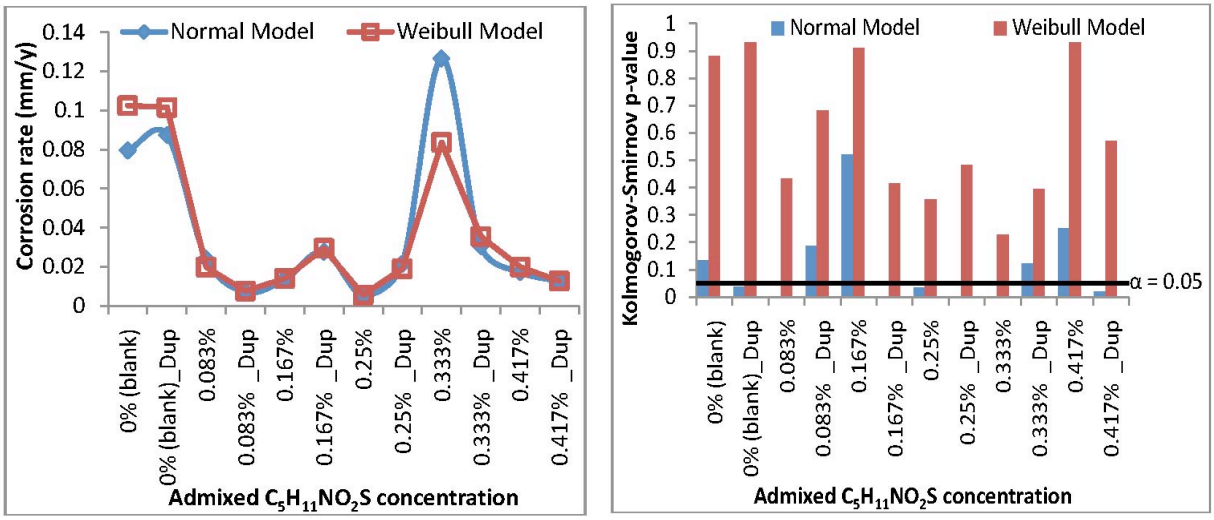

(a) (b)

Fig. 1. Statistical distribution analyses of corrosion rate (a) mean corrosion rate models (b) goodness-of-fit models

In Fig. 1(a), although the Normal mean model of corrosion rate patterned like the Weibull model for most steel-reinforced concrete samples, these distribution models over-predicted one another for some samples. In the plot also, it could be noted that samples with the same $C_5H_{11}NO_2S$ concentrations exhibited instances of discrepancies in the modeled corrosion rate between the duplicate samples. While the observed over-prediction by the statistical distribution models could lead to controversy on which of the distributions to employ for describing the corrosion rate data, this was addressed from the consideration that up to seven samples have their corrosion rate dataset not scattering like the Normal distribution in Fig. 1(b). Kolmogorov-Smirnov *p*-value is < 0.05 for these samples. In contrast, all the corrosion rate dataset of steel-reinforced concrete samples in the study followed the Weibull distribution, *p*-value > 0.05, according to the Kolmogorov-Smirnov goodness-of-fit test. This supports the use of the Weibull distribution model as the descriptive statistics for detailing $C_5H_{11}NO_2S$ effect on concrete steel-reinforcement corrosion in the test-environment.

The instances of discrepancies observed from the corrosion rate models of samples having similar concentration of $C_5H_{11}NO_2S$ admixture was addressed from the student's *t*-test of significance of differences between each of the duplicate samples in the study. The results for this are shown in Fig. 2(a), also with linear plot for indicating threshold of significance. The plot showed that the student's *t*-test *p*-value > 0.05 for all the concentrations of $C_5H_{11}NO_2S$ admixture considered in the study. From this, it could not be rejected that the discrepancies of corrosion rate test-results encountered between the duplicates of steel-reinforced concrete samples are only due to chance but they are not significant.

Based on the foregoing, the Weibull distribution analyses of corrosion rate was used for modeling inhibition efficiency, averaged over each duplicates of steel-reinforced concrete with the same $C_5H_{11}NO_2S$ admixture concentration. The results for this model are presented in Fig. 2(b), in ranking order of $C_5H_{11}NO_2S$ performance at inhibiting steel-reinforcement corrosion in the 0.5 M H_2SO_4 medium. This ranking order showed that while the

other $C_5H_{11}NO_2S$ admixtures employed in the study inhibited steel-reinforcement corrosion in the medium, the 0.25% $C_5H_{11}NO_2S$ exhibited optimal inhibition effect of η = 87.95±7.64 on reinforcing steel corrosion in the industrial/microbial simulating environment studied. This inhibition efficiency model find comparisons with results obtained in reported study by other researchers in acid rain (industrial simulating medium containing sulphuric acid) environment [27] in which inhibition efficiency as high as 80% was obtained through use of sodium molybdate and sodium nitrite as inhibitors. Also, application of the corrosion inhibition efficiency obtained in this study to the efficiency model [4,24] of Coffey et al [28] indicates that the 0.25% $C_5H_{11}NO_2S$ exhibited performance that interprets to "very good" model efficiency on the inhibition of steel-reinforcement corrosion in the studied medium. These results engender support for the use of $C_5H_{11}NO_2S$ (Methionine) as inhibitors of steel-reinforcement corrosion in concrete designed for the industrial/microbial environment.

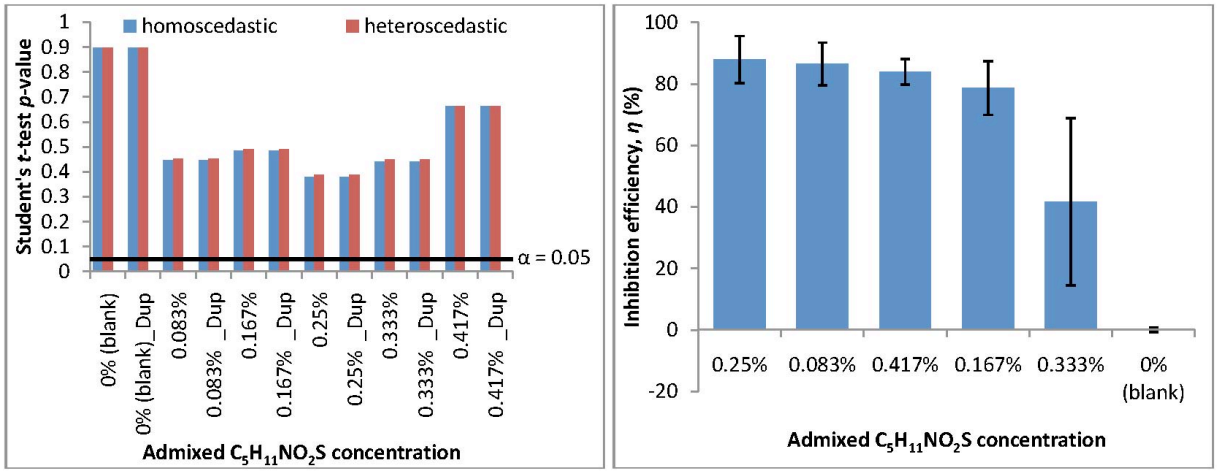

(a) (b)

Fig. 2. Other analyses of $C_5H_{11}NO_2S$ effect on the corrosion of concrete reinforcing steel (a) student's *t*-test model results (b) corrosion inhibition efficiency model

4. Conclusion

It could be concluded from this study that the admixture of $C_5H_{11}NO_2S$ (Methionine) in steel-reinforced concrete exhibited potency at reducing corrosion rate of reinforcing steel in concrete immersed in 0.5 M H_2SO_4 medium, simulating industrial/microbial environment. While other concentrations of $C_5H_{11}NO_2S$ employed in the study also inhibited steel-reinforcement corrosion, it was established in the study that 0.25% $C_5H_{11}NO_2S$, (per weight of concrete mixing cement) exhibited optimal inhibition efficiency of η = 87.95±7.64 on the corrosion of reinforcing steel embedment in concrete immersed in the studied acidic sulphate environment.

References

1. M. Ismail, P.B. Raja, A.A. Salawu, in Handbook of Research on Recent Developments in Materials Science and Corrosion Engineering Education, edited by H. Lim (IGI Global, Hershey, PA, 2015), p. 118
2. F.–L. Fei, J. Hu, J.–X. Wei, Q.–J. Yu, Z.–S. Chen, Construct. Build. Mater. **70**, 43 (2014)
3. N. Ghali, A. Addou, B. Mutel, B. Benstaali, F. Bentiss, J.–L. Brisset, Eur. Phy. J. Appl. Phy. **61**, 30801 (2013)
4. J.O. Okeniyi, I.J. Ambrose, I.O. Oladele, C.A. Loto, A.P.I. Popoola, Int. J. Electrochem. Sci. **8**, 10758 (2013)
5. T.J. Mesquita, E. Chauveau, M. Mantel, N. Kinsman, V. Roche, R.P. Nogueira, Mater. Chem. Phy. **132**, 967 (2012)
6. T. Mesquita, E. Chauveau, M. Mantel, N. Kinsman, R.P. Nogueira, Rev. Metall. **108**, 203 (2011)
7. G. Taché, V. Bouteiller, M. Brouxel, Mater. Tech. **98**, 186 (2010)
8. F. Moulinier, Rev. Metall. **103**, 139 (2006)
9. J.O. Okeniyi, A.P.I. Popoola, C.A. Loto, O.A. Omotosho, S.O. Okpala, I.J. Ambrose, Adv. Mater. Sci. Eng. **2015**, 540395 (2015)
10. J.O. Okeniyi, I.O. Oladele, O.M. Omoniyi, C.A. Loto, A.P. Popoola, Can. J. Civ. Eng. **42**, 408 (2015)
11. Y. Tang, G. Zhang, Y. Zuo, Constr. Build. Mater. **28**, 327 (2012)
12. M.P. Lavigne, A. Bertron, C. Patapy, X. Lefebvre, E. Paul, Mater. Tech. **103**, 204 (2015)
13. J.O. Okeniyi, I.O. Oladele, I.J. Ambrose, S.O. Okpala, O.M. Omoniyi, C.A. Loto, J. Cent. South Univ. **20**, 3697 (2013)
14. J.O. Okeniyi, O.M. Omoniyi, S.O. Okpala, C.A. Loto, A.P.I. Popoola, Eur. J. Environ. Civ. Eng. **17**, 398 (2013)

15. E.E. Oguzie, Y. Li, S.G. Wang, F. Wang, RSC Adv. **1**, 866 (2011)
16. J.O. Okeniyi, C.A. Loto, A.P.I. Popoola, Solid State Phenom. **227**, 281 (2015)
17. H. Gerengi, Y. Kocak, A. Jazdzewska, M. Kurtay, H. Durgun, Constr. Build. Mater. 49, 471 (2013)
18. ASTM G109-99a, Standard Test Method for Determining the Effects of Chemical Admixtures on the Corrosion of Embedded Steel Reinforcement in Concrete Exposed to Chloride Environments. (ASTM International, West Conshohocken, PA, 2005)
19. ASTM C192/192M-02, Standard Practice for Making and Curing Concrete Test Specimens in the Laboratory. (ASTM International, West Conshohocken, PA, 2005)
20. J.O. Okeniyi, C.A. Loto, A.P.I. Popoola, Energy Procedia **50**, 421 (2014)
21. R.A. Corbett, in Corrosion Tests and Standards: Application and Interpretation, 2nd edn. edited by R. Baboian (ASTM International, West Conshohocken, PA, 2005) p. 139
22. M. Ormellese, L. Lazzari, S. Goidanich, G. Fumagalli, A. Brenna, Corros. Sci. **51**, 2959 (2009)
23. J.O. Okeniyi, C.A. Loto, A.P.I. Popoola, Trans. Indian Inst. Met. **67**, 959 (2014)
24. J.O. Okeniyi, I.J. Ambrose, S.O. Okpala, O.M. Omoniyi, I.O. Oladele, C.A. Loto, P.A.I. Popoola, Sadhana **39**, 731 (2014)
25. ASTM G16-95 R04, Standard Guide for Applying Statistics to Analysis of Corrosion Data. (ASTM International, West Conshohocken PA, 2005)
26. O.O. Ajayi, R.O. Fagbenle, J. Katende, S.A. Aasa, J.O. Okeniyi, Int. J. Energy Environ. Eng. **4**, 27 (2013)
27. M.A.G. Tommaselli, N.A. Mariano, S.E. Kuri, Constr. Build. Mater. **23**, 328 (2009)
28. R. Coffey, S. Dorai-Raj, V. O'Flaherty, M. Cormican, E. Cummins, Hum. Ecol. Risk Assess.: An International Journal **19**, 232 (2013)

Biochemical Characterization of *Cymbopogon citratus*: Prospects on Environmentally-Friendly Corrosion-Protection of Concrete Steel-Reinforcement in Aggressive Environment

J.O. Okeniyi,[1,*] E.T. Okeniyi,[2] O.O. Ogunlana,[3] F.T. Owoeye,[4] E.O. Ogunlana[5]
[1]Mechanical Engineering Department, Covenant University, Ota, Nigeria
[2]Petroleum Engineering Department, Covenant University, Ota, Nigeria
[3]Biochemistry Programme, Department of Biological Sciences, Covenant University, Ota, Nigeria
[4]Chemistry Department, Covenant University, Ota, Nigeria
[5]Biochemistry Programme, Department of Biological Sciences, Crawford University, Igbesa, Nigeria
*e-mail: joshua.okeniyi@covenantuniversity.edu.ng

Abstract:
Biochemical characterization of inorganic and organic constituents of the leaf of *Cymbopogon citratus* was investigated in this paper. For this, methods of atomic absorption spectroscopy (AAS), Fourier transform infrared spectroscopy (FT-IR) and phytochemical screening analyses were employed. Results showed that the leaf of *Cymbopogon citratus* exhibited inorganic constituents including iron, Fe = 4,641.025 μg/g, manganese, Mn = 849.5069 μg/g, copper, Cu = 171.045 μg/g, lead, Pb = 13.2938 μg/g, nickel, Ni = 11.5187 μg/g, cadmium, Cd = 4.9310 μg/g, and chromium, Cr = 0.0 μg/g, from the AAS method. The FT-IR detailing indicates organic constituents from *Cymbopogon citratus* leaf-extract includes S-, N-, O- containing heteroatoms and aromatic compounds that are rich in π-electrons and which are known to exhibit coordinate affinity with the iron-containing reinforcing steel metal. Phytochemical screening analyses of *Cymbopogon citratus* leaf-extract showed it is constituted of tannins, phlobatannins, saponins, glycosides, flavonoids, steroids and terpenoids. Further tests on corrosion protection ability showed that this natural plant reduced total corrosion, analyzed as per ASTM G109-99a, in steel-reinforced concrete samples immersed in 0.5 M H_2SO_4 environment. These suggests implications of positive prospects of *Cymbopogon citratus* as an environmentally-friendly inhibitor of reinforcing steel corrosion in concretes having acidic medium as service-environment.

Keywords: *Cymbopogon citratus*, environmentally-friendly natural plant material, reinforcing steel in concrete, total-corrosion analyses, inorganic and organic characterization, phytochemical screening, H_2SO_4 environment.

1. Introduction

Among the different methods for mitigating corrosion risks in steel-reinforced concrete, corrosion inhibitor usage is a less costly and easily applicable method compared to the others [1-6]. However, due to the toxicity of traditional inhibitors [7-10], researchers are turning to extracts from natural plant sources that abounds with biologically safe organic constituents that are also known to inhibit reinforcing steel corrosion in aggressive environments [4,8,11-13]. While synthetic chemical inhibitors could be lethal to living organisms, by disrupting biochemical process and inducing malfunctioning or damage of internal organs, chemicals and phyto-constituents from natural plants are potent with eco-friendly electron donors that also inhibit the corrosion process [7,11,14]. But for use as corrosion inhibitor, constituents from natural plant need to be extracted and characterized for understanding the biochemical ligands that are produced by the plant [11,15]. Such extract also need to be tested in corrosive system for assessing effectiveness at mitigating metallic corrosion in specified environment [15-16].

Cymbopogon citratus, lemongrass, is a perennial, aromatic plant that is indigenous to tropical areas of the world including Africa, Asia, Central and South America, where the fresh and dried leaves are used for medicinal purposes and as ingredients in food [17-20]. According to literature, leaf-extract of *Cymbopogon citratus* is not toxic [17,21], rather infusions, decoctions and essential oils from the plant exhibit health benefits including positive bioactivities of antioxidant, anti-inflammatory, anti-carcinogenic, antihypertensive, anti-diabetic, anti-mutagenic and antimicrobial properties [21-23]. While studies had deliberated on the chemical constituents of this natural plant, indication from literature include the fact that such constituents could vary according to the geographical origin of the plant such that needs for bio-constituents of different extract are still required [17,20]. These constitute motivation for this study, especially on the basis that there is dearth of study in which characterization by the use of Fourier transform infrared, FT-IR, spectroscopy techniques has been detailed for *Cymbopogon citratus*. Also, the phytochemical and inorganic characterization of the plant from our study location could find comparison with that from other regions even as no study has detailed the composition of *Cymbopogon citratus* with respect to its prospect on corrosion-protection of steel-reinforcement in concrete. Thus, this study deliberates on the biochemical characterization of the inorganic and organic constituents of *Cymbopogon citratus* leaf and the prospects of the constituents on the corrosion protection of concrete steel-reinforcement in aggressive medium.

2. Experimental

Leaves of *Cymbopogon citratus* (*C. citratus*) *Poaceae* were collected fresh at Idiroko Road, Canaanland, Ota, Ogun State, Nigeria. The leaves were identified at the Forestry Herbarium Ibadan (FHI), Nigeria and a sample was deposited there with the voucher FHI. No. 109497. The leaves of *C. citratus* for this study were dried under cover in a well aerated room maintained at 20 °C by a 5 ton air-conditioning system.

Study of inorganic (heavy metal) constituent using the AAS (Atomic Absorption Spectrometer) technique followed the procedure that had been detailed in [15]. This was initiated by ashing some dried and pulverised leaves of *C. citratus* in a muffle furnace maintained for 2 hrs at 500°C. The ash content obtained by this = 6.3989%. From the ashed material, 0.25 g was soaked overnight in 5 ml of 1:1 nitric-perchloric acid mixture. This was then heated at 150 °C for 1 hr in a reflux condenser before raising the temperature gradually to 235 °C by heating and the heating then maintained for another 2 hr for the occurrence of dense fume. The test-material was then removed from the heating block, cooled to 100 °C before the addition of 1:1 HCl, and which was followed by heating to white fumes until the resultant solution obtained was colourless. The colourless solution was then poured into 100 ml flask and washed with water for five times, at which the washing was added to the flask each of the time. The volume was then made up to the 100 ml mark of the flask with water. Then, the obtained solution was filtered and the filtrate from this was taken to the Hollow Cathode Lamps equipped Model S Series, AA Spectrometer from Thermo Electron Corporation®.

Two methods were employed for the characterization of organic constituent, which was initiated by obtaining leaf-extract of *C. citratus*, using procedure that had been detailed in studies [13,24]. The first method, the FT-IR analyses, includes smearing of *C. citratus* leaf-extract between a pair of mounting discs that was then mounted onto the FT-IR instrument of the Perkin-Elmer FT-IR System, Spectrum BX.

The second method for organic constituent characterization employs phytochemical screening methods using the procedures prescribed in [25] and detailed in [15]. For this, 2 g of *C. citratus* leaf-extract was added to 20 ml of distilled water for making test sample that was then subjected to the phytochemical test-procedures detailed in [15] for the tests for tannins, phlobatannins, saponins, flavonoids, steroids, terpenoids, glycosides and alkaloids.

3. Results and discussion

Results of the AAS analyses for heavy metals are as shown in Table 1. This showed that the tested plant was rich in iron micronutrient and low in other heavy metals, which indicates that the growth environment of the studied *C. citratus* was not toxic with other heavy metals that could have resulted in the deficiency of Fe [15,26].

Table 1. AAS Test-results of inorganic constituents from *C. citratus*

Inorganic Constituent	Iron (Fe)	Manganese (Mn)	Copper (Cu)	Lead (Pb)	Nickel (Ni)	Cadmium (Cd)	Chromium (Cr)
Concentration (μg/g)	4641.025	849.5069	171.045	13.2938	11.5187	4.9310	-

Results of the organic constituent characterisation of *C. citratus* are presented in Fig. 1, for the FT-IR spectra, and in Table 2, for the phytochemical screening analyses. Fig. 1 showed that the extract exhibited overlaps of many organic heteroatoms. Notable from the figure include the free O–H stretching vibration of hydroxyl group absorbed at 3731.85 cm^{-1}, a high frequency that, according to [27] suggests characterization of phenol antioxidants class of compounds that could be found in food. This exhibits fingerprint of phenol (a hydroxyl group bonded to an aromatic hydrocarbon group) or tertiary alcohol O–H in-plane bending vibration at 1405.25 cm^{-1}. Another fingerprint for this group includes the C–O stretching bands at 1155.95 cm^{-1}, suggesting tertiary alcohol, and at 1039.63 cm^{-1}. The 3355.00 cm^{-1} exhibited potencies of overlaps of N–H stretch of the secondary amine group, having fingerprint of NH_2 scissoring at 1567.82 cm^{-1} and N–H wagging at 854.40 cm^{-1} and 709.25 cm^{-1}, and/or of carboxylic acid due to the additional O–H stretch at 2929.68 cm^{-1} and C=O at 1702.35 cm^{-1}. This carboxylic acid group suggestion followed from the overlapping of the group's fingerprints in the spectra including the in-plane bending of C–O–H at 1405.25 cm^{-1} and the O–H out-of-plane bending at 924.74 cm^{-1}. In the same light, the absorption at 709.25 cm^{-1} could also include C–Cl stretch of chloro halogenated organic compounds, just as the 1039.63 cm^{-1} could also represent weakened frequency, due to electron extraction, of the C=S thiocarbonyl while the absorption at 2351.10 cm^{-1} could be weakened frequency of the S–H thiols.

Phytochemical screening analyses of *C. citratus* leaf-extract showed that it contains seven out of the eight phytoconstituents tested; only alkaloids was not identified as been present in the extract. These phytochemical test-results find agreements with that from [17] wherein it was confirmed that *C. citratus* contained tannins, saponins, flavonoids and steroids. That study did not test for phlobatannins, glycosides and terpenoids although alkaloids was found to be present in *C. citratus* in that study but not observed by the phytochemical test in this study.

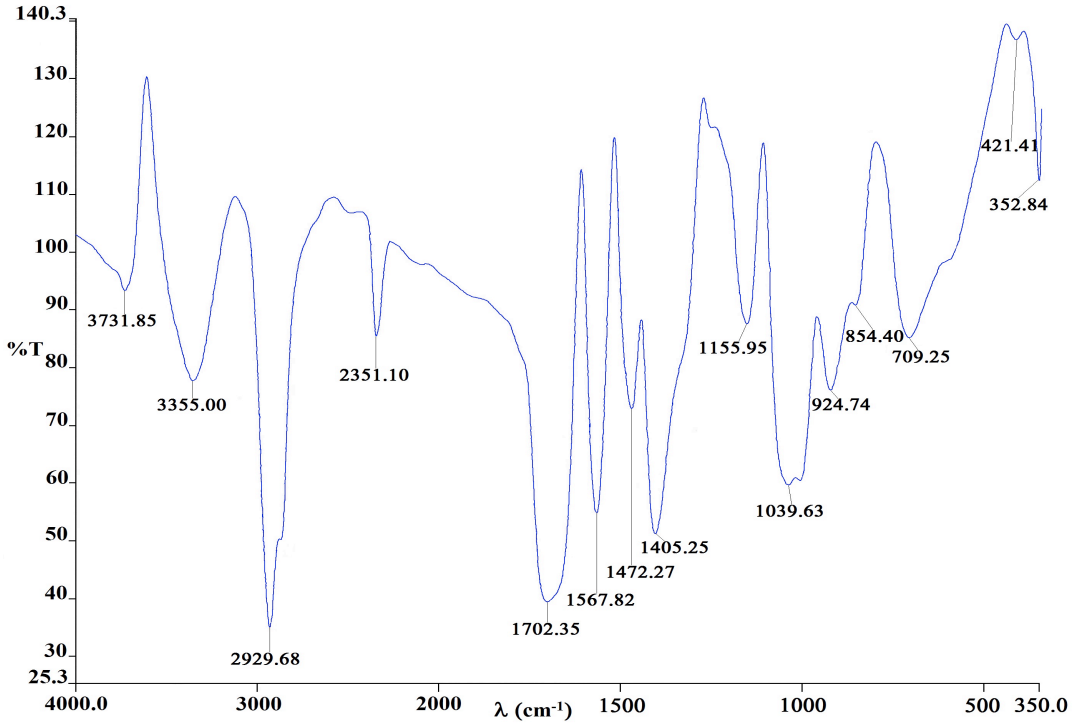

Fig. 1. FT-IR spectra of the leaf extract of *C. citratus*

Table 2. Phytochemical constituent of *C. citratus**

Tannins	Phlobatannins	Saponins	Glycosides	Flavonoids	Steroids	Terpenoids	Alkaloids
+	+	+	+	+	+	+	–

* Present ≡ +; Absent ≡ –

It is worth noting that plant extract with FT-IR spectra and phytochemical test-results finding similarity with that obtained in this study had been employed in other studies for inhibiting steel corrosion in aggressive media [13,24,28-29]. Among these, the plant extract in [24,28] inhibited steel corrosion in 0.5 M H_2SO_4. Also, the report in [28] showed that ligands with aromatic, lone pairs and π electron donors exhibited affinity for carbon steel. In that study in [28], the ligands were characterized from the protective film on the carbon steel metal. For this reason, 1.667 g/L (of concrete mixing water) *C. citratus* and 6.667 g/L *C. citratus* leaf-extract were admixed in steel-reinforced concrete specimens immersed in 0.5 M H_2SO_4 medium. From these, as well as from blank sample of similarly cast steel-reinforced concrete but with 0 g/L *C. citratus* leaf-extract (i.e. blank or control sample), corrosion current was measured at interval for 82 days experimental period and analyzed as per ASTM G109-99a [30-31]. The analyzed results of this experimentation are as plotted in Fig. 2.

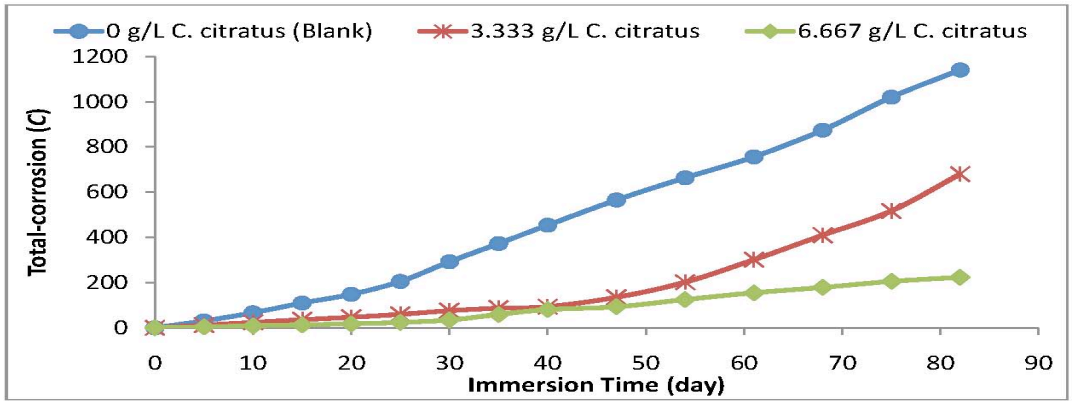

Fig. 2. Total corrosion effects of *C. citratus* leaf-extract admixture on steel-reinforced concrete in aggressive medium

This showed that admixtures of *C. citratus* in concrete reduced total corrosion of the embedded steel-reinforcement in the 0.5 M H_2SO_4-immersed concrete, relative to the blank specimen of steel-reinforced concrete in the aggressive environment. These bare implications of positive prospects on the suitability of *C. citratus* leaf-

extract as an environmentally-friendly admixture in concrete for the corrosion protection of reinforcing steel in concrete designed for aggressive service-environment.

4. Conclusion

It is established in this study that the leaf of *C. citratus* contains non-toxic levels of inorganic (heavy metal) micronutrients. Also, FT-IR characterization of *C. citratus* leaf-extract indicates the plant is potent with S-, N-, O-containing heteroatoms and aromatic compounds that are rich in lone pairs and π-electrons, which are known to exhibit coordinate affinity with steel metal used for concrete reinforcement. Phytochemical screening tests also indicate presence of phyto-constituents that could enhance steel-rebar corrosion-protection in aggressive environment. Test of this notion of corrosion-protection ability in the study also exhibited confirmations that concentrations of *C. citratus* leaf-extract admixture reduced total corrosion, relative to blank specimen without admixture, in steel-reinforced concretes immersed in 0.5 M H_2SO_4 medium. Therefore, it could be concluded from the study that *C. citratus* exhibited positive prospects for environmentally-friendly corrosion protection of concrete steel-reinforcement in aggressive environment.

References

1. D.M. Bastidas, M. Criado, S. Fajardo, A.L. Iglesia, J.M. Bastidas, Cem. Concr. Compos. **61**,1 (2015)
2. J.O. Okeniyi, I.O. Oladele, O.M. Omoniyi, C.A. Loto, A.P. Popoola, Can. J. Civ. Eng. **42**, 408 (2015)
3. F.–L. Fei, J. Hu, J.–X. Wei, Q.–J. Yu, Z.–S. Chen, Construct. Build. Mater. **70**, 43 (2014)
4. J.O. Okeniyi, C.A. Loto, A.P.I. Popoola, Int. J. Electrochem. Sci. **9**, 4205 (2014)
5. J.O. Okeniyi, I.J. Ambrose, I.O. Oladele, C.A. Loto, A.P.I. Popoola, Int. J. Electrochem. Sci. **8**, 10758 (2013)
6. Y. Tang, G. Zhang, Y. Zuo, Constr. Build. Mater. **28**, 327 (2012)
7. J.O. Okeniyi, O.A. Omotosho, O.O. Ajayi, C.A. Loto, Constr. Build. Mater. **50**, 448 (2014)
8. S.A. Asipita, M. Ismail, M.Z. Abd Majid, Z.A. Majid, C. Abdullahb, J. Mirza, J. Clean. Prod. **67**, 139 (2014)
9. J.O. Okeniyi, O.A. Omotosho, O. Ajayi, O.O. James, C.A. Loto, Asian J. Appl. Sci. **5**, 132 (2012)
10. O.A. Omotosho, J.O. Okeniyi, O.O. Ajayi, C.A. Loto, Int. J. Environ. Sci. **2**, 2346 (2012)
11. M. Ismail, P.B. Raja, A.A. Salawu, in Handbook of Research on Recent Developments in Materials Science and Corrosion Engineering Education, edited by H. Lim (IGI Global, Hershey, PA, 2015), p. 118
12. J.O. Okeniyi, C.A. Loto, A.P.I. Popoola, Energy Procedia **50**, 429 (2014)
13. J.O. Okeniyi, C.A. Loto, A.P.I. Popoola, Trans. Indian Inst. Met. **67**, 959 (2014)
14. A.K. Satapathy, G. Gunasekaran, S.C. Sahoo, K. Amit, P.V. Rodrigues, Corros. Sci. **51**, 2848 (2009)
15. J.O. Okeniyi, O.O. Ogunlana, O.E. Ogunlana, T.F. Owoeye, E.T. Okeniyi, in TMS2015 Supplemental Proceedings (John Wiley & Sons, Inc., Hoboken, NJ, 2015) p. 635
16. J.O. Okeniyi, C.A. Loto, A.P.I. Popoola, Energy Procedia **50**, 421 (2014)
17. C.E. Ekpenyong, E.E. Akpan, N.E. Daniel, J. Pharmacogn. Phytochem. **3**, 133 (2014)
18. K. Manvitha, B. Bidya, Int. J. Herb. Med. **1**, 5 (2014)
19. V. Francisco, A. Figueirinha, G. Costa, J. Liberal, M.C. Lopes, C. García-Rodríguez, C.F.G.C. Geraldes, M.T. Cruz, M.T. Batista, J. Funct. Foods **10**, 436 (2014)
20. G. Shah, R. Shri, V. Panchal, N. Sharma, B. Singh, A.S. Mann, J. Adv. Pharm. Technol. Res. 2, 3 (2011)
21. S. K. Olorunnisola, H.T. Asiyanbi, A.M. Hammed, S. Simsek, Int. Food Res. J. **21**, 455 (2014)
22. S.R. Kanatt, S.P. Chawla, A. Sharma, Food Biosci. **6**, 24 (2014)
23. V. Francisco, G. Costa , A. Figueirinha, C. Marques, P. Pereira, B.M. Neves, M.C. Lopes, C. García-Rodríguez, M.T. Cruz , M.T. Batista, J. Ethnopharmacol. **148**, 126 (2013)
24. J.O. Okeniyi, C.A. Loto, A.P.I. Popoola, Port. Electrochim. Acta **32**, 199 (2014)
25. H.O. Edeoga, D.E. Okwu, B.O. Mbaebie, Afr. J. Biotechnol. **4**, 685 (2005)
26. United States Environmental Protection Agency (USEPA), Ecological Soil Screening Levels for Iron (USEPA, Washington, DC, 2003).
27. J. Coates, in Encyclopedia of Analytical Chemistry, edited by R.A. Meyers (John Wiley & Sons Ltd, Chichester, 2000) p. 10815
28. P. Mourya, S. Banerjee, M.M. Singh, Corros. Sci. **85**, 352 (2014)
29. M. Sangeetha, S. Rajendran, J. Sathiyabama, A. Krishnaveni, P. Shanthy, N. Manimaran, B. Shyamaladevi, Port. Electrochim. Acta **29**, 429 (2011)
30. ASTM G109-99a, Standard Test Method for Determining the Effects of Chemical Admixtures on the Corrosion of Embedded Steel Reinforcement in Concrete Exposed to Chloride Environments. (ASTM International, West Conshohocken, PA, 2005)
31. J.O. Okeniyi, C.A. Loto, A.P.I. Popoola, in TMS2015 Supplemental Proceedings (John Wiley & Sons, Inc., Hoboken, NJ, 2015) p. 751

THE EFFICIENCY OF AL_2O_3-WATER NANOFLUID ON A FLAT-PLATE SOLAR COLLECTOR

N. Budak [1*], H.L. Yucel [2] , C. Yildiz [2], Z.Argunhan[1], S.Tekalp[3]

[1]Batman University, Department of Mechanical Engineering, Batman, Turkey.
[2]Firat University, Department of Mechanical Engineering, Elazig, Turkey.
[3]Batman University, Department of English Language and Literature, Batman, Turkey.

Abstract: Solar collectors are particular kind of heat exchangers that transform solar radiation energy into internal energy of the transport medium. One of the most effective methods is replacing the working fluid (water, ethylene glycol, engine oil…) by developing a new class of fluids with a higher thermal conductivity for thermal systems. In the present work the effect of Al_2O_3-water, as working fluid, on the efficiency of a flat plate solar collector is investigated experimentally. The mass flow rate of nanofluid is 150 Lit/h. The volume fraction of the nanoparticles is 0.2 %, 0.4 % and 0.8 % respectively. The results reveal the impact and importance of each of these parameters. Experimental results reveal that utilizing the nanofluid increases the collector efficiency in comparison to water as an absorbing medium.

Keywords: nanofluid, flat-plate solar collector, efficiency.

1. Introduction

Solar energy has the greatest potential of all the sources of renewable energy when other sources in the country have depleted. Solar collector as a solar energy recovery device recovers the energy of sun and converts it to heat. It is also used in different applications including solar electricity, air conditioning, cooker and water heater [1]. Various types of solar collectors are available, but most productive and commonly used is flat plate solar collector. It is cheaper and based on simpler technology, but it has comparatively low efficiency and outlet temperatures [2]. Using the flat plate solar collectors in applications has been subjected to a lot of studies [3-7]. Some conventional modifications are used (the size optimization, the glazing materials changing... etc.) to improve the collector's efficiency. But these methods are often inconvenient.

The novel approach is to introduce the nanofluids instead of conventional heat transfer fluids (like water, engine oil, ethylene glycol …). The poor heat transfer properties of these conventional fluids compared to most solids are the primary obstacle to the high compactness and effectiveness of the system. The essential initiative is to seek the solid particles having thermal conductivity of several hundred times higher than those of conventional fluids. Applying nanotechnology to thermal engineering, the new concept of 'nanofluid' which was coined by Choi in 1995 [8] has been proposed to meet cooling challenges. Nanofluids are suspensions of metallic or nonmetallic nanoparticles (<100 nm) in a base fluid. Nanofluids represent improved stability compared with conventional fluids added with micrometer- or millimeter-sized solid particles because of size effect and Brownian motion of the nanoparticles in liquids. With such ultrafine nanoparticles, nanofluids can flow smoothly in a microchannel without clogging and the size of the heat transfer system can be reduced for the use of nanofluids with high heat transfer efficiency [9]. Xie et al. [10] prepared non-oxide ceramic (SiC) nanofluid with particle size ranging between 26 and 600 nm, whereas Xie et al. [11] produced Al_2O_3 nanofluid with particle size ranging from 1.2 to 302 nm. High enhancement in the thermal conductivity was observed in addition to the effect of particle size. Hrishikesh et al. [12] obtained for thermal conductivity of nanofluids with variation in nanoparticle material (Al_2O_3, CuO, Cu, Al), base liquid (transformer oil, ethylene glycol, water) particle size (11, 31, 45, 80, 150 nm), particle volume fraction (0.5, 1, 2, 3%) and suspension temperature (20, 30, 40, 50^oC) experimentally. It was also observed that the

thermal conductivity of nanoparticle suspensions is relatively higher at lower volume fractions, thereby giving a non-linear dependence on the particle volume fraction. Kang et al. [13] reported a 75% thermal conductivity enhancement for ethylene glycol with 1.2% (v/v) diamond nanoparticles between 30 and 50nm in diameter. Nanofluids thermophysical properties were investigated by several studies on thermal conductivity and convective heat transfer coefficient for different materials and particle size [14-16]. Duangthongsuk et al. [17] experimentally examined the temperature-dependent thermal conductivity and viscosity of TiO_2/water nanofluids with volume concentrations between 0.2 and 2.0%. The data were collected for temperatures ranging from 15 ^oC to 35 ^oC. The results showed that the relative thermal conductivity of nanofluids increased with increasing particle volume concentration and slightly decreased with increasing temperature.

So far, there are many other publications reporting on the enhanced thermal conductivity of different nanofluids as the working fluid under different conditions for the solar collectors recently. [18-20]. Yousefi et al. [21] investigated the effect of Al_2O_3-water nanofluid on the efficiency of flat plate solar collector and reported 28.3% enhancement for 0.2 wt%. Also the same researchers [22-23] reported the effect of MWCNT-H_2O as an absorbing medium on the efficiency and the effect of pH variation experimentally for 0.4 wt%. Results showed 35% enhancement in the collector efficiency for 0.4 wt%. Otanicar et al. [24] studied experimentally the effects of different nanofluids (carbon nanotubes, graphite and silver) on the performance of a micro scale direct absorption solar collector (DASC). They demonstrated efficiency improvements of up to 5% in solar thermal collectors by utilizing nanofluids as the absorption mechanism. The effects of using CuO-water nanofluid as the absorbing medium on the flat-plate solar collector efficiency were studied experimentally by Moghadam et al.[25]. The results demonstrated that using CuO–H_2O nanofluid increases the solar collector efficiency in comparison with that of water by 16.7%.

Based on the previous study, the aim of this current experimental work is to investigate the effect of Al_2O_3-water, as working fluid, on the efficiency of a flat plate solar collector for 0.2 %, 0.4 % and 0.8 % volume fractions respectively.

2. Experimental apparatus and description

2.1. Preparation of nanofluids

Adding nanoparticles into base fluid is an important process requiring special attention. The prepared nanofluid should be stable suspension for long durations without sedimentation [26]. The two-step method has been applied in this study. The two-step method used for preparing nanofluids is a process in which nanoparticles are dispersed into the base liquids. [27]. The commercial γ- Al_2O_3 powders were supplied by Sigma–Aldrich Corporation in this experimental study. De-ionized water was used as the base liquid. Nanoparticles were dispersed into the de-ionized water with different concentrations of 0.2%, 0.4%, and 0.8%. The mixture was prepared for about 2 hour in an ultrasonic homogenizer (UP-400S ultrasonic model) continuously in order to minimize nanoparticles aggregation and improve dispersion behavior at Erzurum Technical University. The prepared nanofluid solutions are shown in Fig.1. No sedimentation was observed for concentrations in the first 90 days.

Figure 1. Prepared Al_2O_3- water nanofluids

2.2. Experimental set-up

The image of the experimental setup are presented in Fig. 2.

Figure 2. The image of the experimental setup

The solar collector performance was experimentally investigated in Elazig, Turkey (latitude is 38^o 40' 51" N and longitude is 39^o

13' 25" E). The optimum collector slope is calculated as follows [28]:

$$\beta = |\phi - \delta| \quad (1)$$

where ϕ is the latitude and δ is given by:

$$\delta = 23/45 \sin(360 \frac{n+284}{365}) \quad (2)$$

in which , n is the number of day in a year. In this study, the optimum slope of the collector is obtained 35°. The solar system is a force convection system, accordingly the working fluid is circulated through the collector by using an electrical pump.

2.3. Testing method

The ASHRAE Standard 86-93 [29] is one of the most important standards used to provide test methods and calculation procedures for determining steady-state and quasi-steady-state thermal performance, time and angular response characteristics of solar collectors. The standard computes the performance by obtaining the values of instantaneous efficiency for various combinations of incident radiation, inlet fluid temperature and ambient temperature.

2.4. Efficiency calculation

The performance of a solar collector operating under steady-state conditions can be successfully described by Eq. (4) according to ASHRAE Standard. The useful energy can also be described in terms of the energy absorbed by the absorber and the energy lost from the absorber as given by Eq. (5).

$$Q_u = mC_p(T_o - T_i) \quad (4)$$

$$Q_u = A_c F_R[G_T(\tau\alpha) - U_L(T_i - T_a)] \quad (5)$$

where C_p is the heat capacity of water or nanofluid. The heat capacity of nanofluid is calculated as follow [28] :

$$C_{p,nf} = C_{p,np}(\varphi) + C_{p,bf}(1-\varphi) \quad (6)$$

where φ indicates the volume fraction of nanoparticles, and $C_{p,np}$ and $C_{p,bf}$ are 880j/kg K and 4182 j/kg K, respectively.

The instantaneous collector efficiency relates the useful energy to the total energy incident on the collector surface by the following equations:

$$\eta_i = \frac{Q_u}{A_c G_T} = \frac{mc_p(T_o - T_i)}{G_T} \quad (7)$$

$$\eta_i = F_R(\tau\alpha) - F_R U_L \frac{T_i - T_a}{G_T} \quad (8)$$

If the normal incidence conditions are nearly provided, $F_R(\tau\alpha)$ may be assumed constant within the measured temperature ranges. So according to Eq. (8), a straight line will be obtained for the collector efficiency. This line intersects the vertical axis (efficiency) at $F_R(\tau\alpha)$. At this point, the temperature of the fluid entering the collector equals the ambient temperature, and the maximum collector efficiency is achieved. In this study, it is nominated as the absorbed energy parameter. The line slope which is equal to $F_R U_L$ indicates that how energy has removed from the solar collector, and so it has been nominated as the removed energy parameter [30].

3. Results and discussion

In order to investigate the performance of nanofluids as the working fluids in the solar collector system, each experiment was performed 07:30 – 18:30 (each test run was chosen 30 min) and the good data, which have minimum errors, were chosen to analyze. Figure 3 shows an example of typical recorded data for water and nanofluids at 150 Lit/h in one of the test days. The inlet fluid temperature is almost remain unchanged, the outlet fluid temperature is the critical parameter.

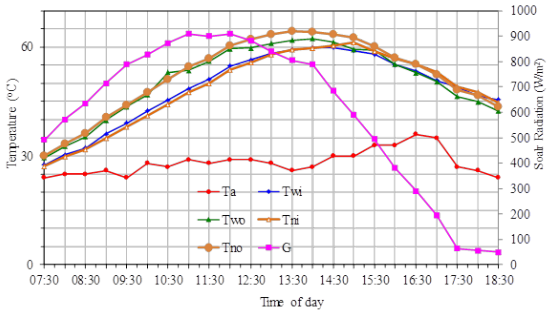

Figure 3. Experimental data for water and nanofluid as working fluid

As can be seen from Fig. 4, before 13:30 the outlet temperature of nanofluids is higher than that of water. The temperature difference of the outlet between nanofluids and water decreased gradually with the solar radiation decline (13:30-18:30). The temperature of nanofluids enhanced faster than that of water because of the superior heat transfer performance. But in the process of solar radiation rapid decline, the heat loss cannot be ignored. The heat loss of nanofluids is more than that of water. Hence, the outlet temperature of nanofluids is more and

more close to the outlet temperature of water [31]. Figure 4, 5 and 6 represent the effect of volume fraction of water and nanofluids on the efficiency of solar collector. The efficiency of collector for water and nanofluid is drawn versus decreased temperature parameters ($\frac{T_i - T_a}{G_T}$). As shown in Fig 4, 5 and 6, the efficiency of flat plate solar collector with Al_2O_3-H_2O nanofluid is higher than that of water. The maximum efficiency (T_i=T_a) of flat-plate solar collector with 0.2 % Al_2O_3-H_2O nanofluid is increased compared with water.

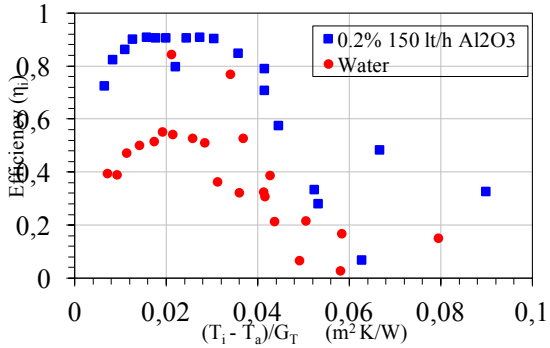

Figure 4. The efficiency of the flat-plate solar collector for water and Al_2O_3-H_2O as the working fluid in 0.2% volume fraction

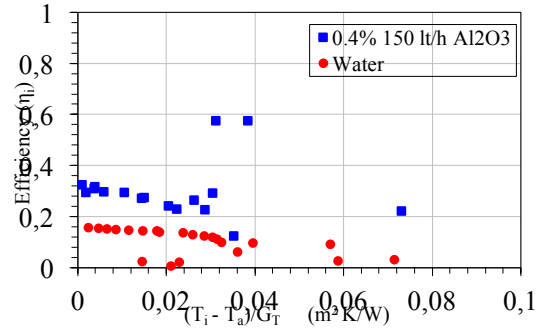

Figure 5. The efficiency of the flat-plate solar collector for water and Al_2O_3-H_2O as the working fluid in 0.4% volume fraction

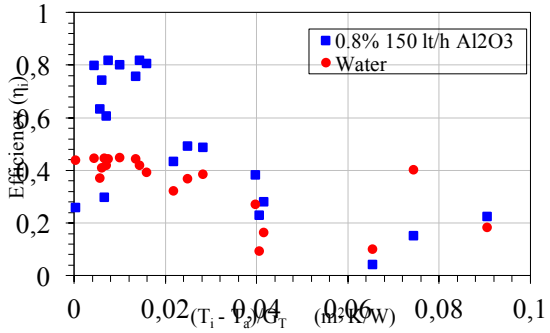

Figure 6. The efficiency of the flat-plate solar collector for water and Al_2O_3-H_2O as the working fluid in 0.8% volume fraction

According to previous researches [32], nanoparticles in nanofluids at higher concentration tend to be agglomerated and the stability of homogenous solutions will be reduced. So, the stability of prepared nanofluid with lower concentration is more than the higher one. It can be resulted that for small temperature differences, the growth rate of thermal conductivity for 0.8% is smaller than that for 0.2 %. However, higher temperature causes the speed increment of molecules, and increases collisions between nanoparticles and the molecules of bulk liquid, results in an increased thermal conductivity [21, 22, 23].

4. Conclusion

This paper presented an experimental study of the effect of using the Al_2O_3-H_2O nanofluid as a working fluid in a flat-plate solar collector. The effect of volume fractions (0.2%, 0.4% and 0.8%) on the efficiency of the collector was investigated at 150 Lit/h. The results showed that adding nanoparticles into de-ionized water enhanced heat transfer and increased the efficiency of collector in comparison with water. It can be concluded that the investigation reported here will deliver the solar investigators with knowledge about enhancing the collector systems using nanofluids.

Acknowledgement

This research is supported by Firat University, Research Project Foundation (Project No: MF.14.24). The authors wish to thank Firat University.

References

[1] Thirugnanasambandam M, Iniyan S, Goic R. A review of solar thermal technologies. Renewable and Sustainable Energy Reviews, 2010; 14: 312–22.

[2] Said Z., Sabiha M.A., Saidur R., Hepbaşlı A., Rahim N.A., Mekhilef S., Ward T.A. Performance enhancement of a flat plate solar collector using Titanium dioxide nanofluid and Polyethylene Glycol dispersant. Journal of Cleaner Production, 2015; 92: 343-353.

[3] Esen M., Esen H. Experimental investigation of a two-phase closed thermosiphon solar water heater. Solar Energy, 2005; 79: 459–468.

[4] Rojas D., Beermann J., Klein S., Reindl D. Thermal performance testing of flat plate collectors. Solar Energy, 2008; 82: 746–757.

[5] Villar N.M., López J., Muñoz F. D., García E.R., Andrés A.C. Numerical 3-D heat flux simulations on flat plate solar collectors. Solar Energy, 2009; 83: 1086–1092.

[6] Tang R, Yang Y, Gao W. Comparative studies on thermal performance of water-in-glass evacuated tube solar water heaters with

different collector tilt-angles. Solar Energy, 2011; 85: 1381–1389.
[7] Amer E.H., Nayak, J.K., Sharma, G.K. Transient test methods for flat-plate collectors: Review and experimental evaluation. Solar Energy, 1997; 60: 5, 229–243.
[8] Choi, S.U.S. Enhancing thermal conductivity of fluids with nanoparticles, in: The Proceedings of the 1995 ASME Int. Mechanical Engineering Congress and Exposition, ASME, San Francisco, USA, 1995, pp. 99-105. FED 231/MD 66.
[9] Haddad Z., Abid , C., Oztop H. F., Mataoui A., A review on how the researchers prepare their nanofluids. International Journal of Thermal Sciences, 2014; 76: 168-189.
[10] Xie H, Wang J, Xi T, Liu Y., Study on the thermal conductivity of SiC nanofluids. J Chin Ceram Soc, 2001; 29(4): 361–364.
[11] Xie HQ, Wang JC, Xi TG, Liu Y, Ai F, Wu QR, Thermal conductivity enhancement of suspensions containing nanosized alumina particles, 2002; J Appl Phys 91: 4568–4572.
[12] Patel , H. E., Sundararajan , T., Das S. K. An experimental investigation into the thermal conductivity enhancement in oxide and metallic nanofluids, 2010; Journal of Nanoparticle Research, 12(3):1015-1031.
[13] Kang HU, Kim SH, Oh JM. Estimation of thermal conductivity of nanofluid using experimental effective particle volume. 2006; Exp Heat Transfer 19(3):181–91.
[14] Saidur R., Leong K.Y., Mohammad H.A. A Review on Applications and Challenges of Nanofluids. Renew. 2011; Sustain. Energy Rev., 15: 1646–68,.
[15] Colangelo G., Favale E., de Risi A., Laforgia D., Results Of Experimental Investigations on the Heat Conductivity of Nanofluids Based on Diathermic Oil for High Temperature Applications. 2012; Appl Energy, 97: 828–33,
[16] Chopkar M., Das P.K., Manna I., Synthesis And Characterization of Nanofluid for Advanced Heat Transfer Applications. 2006; Scripta Materialia, 55: 549–52.
[17] Duangthongsuk, W.,Wongwises, S., Measurement of temperature-dependent thermal conductivity and viscosity of TiO2-water nanofluids. 2009, Thermal Fluid Sci. 33, 706-714.
[18] Polvongsri S., Kiatsiriroat T., Enhancement of Flat-Plate Solar Collector Thermal Performance with Silver Nano-fluid, 2011, The Second TSME International Conference on Mechanical Engineering,
[19] Chaji H., Ajabshirchi, Y., Esmaeilzadeh, E., Heris, S. Z., Hedayatizadeh M., Kahani M., Experimental Study on Thermal Efficiency of Flat Plate Solar Collector Using TiO_2/Water Nanofluid, 2013; Modern Applied Science; Vol. 7, No. 10; 60-69.
[20] Nasrin, R., Parvin, S., Alim M. A., Effect of Prandtl number on free convection in a solar collector filled with nanofluid, 2013, Procedia Engineering,56, 54 – 62.
[21] Yousefi, T., Veisy, F., Shojaeizadeh, E., Zinadini, S. An experimental investigation on the effect of Al_2O_3–H_2O nanofluid on the efficiency of flat-plate solar collectors. Renew. Energ. 2012; 39: 293–298.
[22] Yousefi, T., Veisy, F., Shojaeizadeh, E., Zinadini, S. An experimental investigation on the effect of MWCNT-H_2O nanofluid on the efficiency of flat-plate solar collectors. Exp. Therm. Fluid Sci. 2012; 39: 207–212.
[23] Yousefi, T., Veysi, F., Shojaeizadeh, E., Zinadini, S. An experimental investigation on the effect of pH variation of MWCNT-H_2O nanofluid on the efficiency of a flat-plate solar collector. Solar Energy, 2012; 86: 771–779.
[24] Otanicar, T.P., Phelan, P.E., Prasher, R.S., Rosengarten, G., Taylor, R.A. Nanofluid based direct absorption solar collector. J. Renew. Sustain. Energy, 2010;2:. 033102-1.
[25] Moghadam, A., J., Mahmood, F., G., Mahmood, S., Monireh, H.,Z. Effects of CuO/water nanofluid on the efficiency of a flat-plate solar collector. Experimental Thermal and Fluid Science, 2014; 58: 9–14.
[26] Sahin B., Gültekin, G.,G., Manay, E., Karagoz S., Experimental investigation of heat transfer and pressure drop characteristics of Al_2O_3–water nanofluid. Experimental Thermal and Fluid Science, 2013; 50: 21–28.
[27] Yanjiao Li, Y., Jing'en Zhou, J., Simon Tung, S., Schneider, E., Xi, S. A review on development of nanofluid preparation and characterization. Powder Technol, 2009; 196: 89–101.
[28] J. Duffie, W. Beckman, Solar Engineering of Thermal Processes, Wiely, 2006.
[29] ASHRAE Standard 93-2003, Methods of testing to determine the thermal performance of solar collectors, Atlanta, GA, USA, 2003.
[30] Zhou, S., Ni, R., Measurement of the specific heat capacity of water-based Al2O3 nanofluid. Applied Physics Letters, 2008; 92: 093123.

[31] He, Q., Zeng , S., Wang, S., Experimental investigation on the efficiency of flat-plate solar collectors with nanofluids, Applied Thermal Engineering, 2015; 88: 165-171.
[32] Colangelo, G., Favale, E., Miglietta, P., Risi, A., Milanese, M., Laforgia, D., Experimental test of an innovative high concentration nanofluid solar collector. Applied Energy, 2015; 154: 874–881.

Effect of Repetitive Thermomechanical Processing on Grain Boundary Characteristics in alpha-phase brass

K. J. Al-Fadhalah
Kuwait University, Department of Mechanical Engineering, Kuwait

Abstract:
Commercial (70Cu–30Zn) brass alloy of alpha-phase was thermomechanically processed to enhance the special coincidence site lattice (CSL) boundaries. Four cycles of thermomechanically processing (TMP) were applied, with each cycle consisting of uniaxial compression (strain of 0.15) and annealing (670ºC/10 min). Also, three different compression temperatures (25ºC, 250ºC and -100 ºC) were used. Microstructure evaluation by electron backscattered diffraction (EBSD) indicates that the use of high compression temperature of 250ºC after one cycle promoted the largest formation of Σ3 boundaries (frequency of 57%), associated with the formation of annealing twins. It was also found that the use of 4 cycles of TMP was necessary to stabilize the grain boundary characteristics and to further increase the frequency of Σ3 boundaries to about 62%. In addition, the formation of annealing twins was accompanied by partial randomization of compression texture.

Keywords: brass, thermomechanical processing, annealing twins, microstructure, texture.

Introduction:
Thermomechanical processing (TMP) has been widely used to alter several properties of fcc metals of low stacking fault energy, including strength, ductility, creep resistance, and resistance to intergranular corrosion [1]. In TMP, the polycrystalline metal typically deforms to a specific amount of strain and later annealed to a temperature sufficient to facilitate recrystallization of the deformed microstructure and thus enhance formation of annealing twins. Consequently, the improvement of properties greatly depends on the manipulation of the grain boundary crystallography, which generally requires repetitive TMP cycles (commonly 2 to 5 cycles). The annealing twin boundaries formed by TMP have been commonly described in terms of CSL boundaries with low values of Σ , particularly $\Sigma 3^n$ boundaries (n =1,2,3). Randle [2] reported that $\Sigma 3^n$ boundaries boundaries serve at different stages of microstructural development, including retaining strain during deformation, generating additional $\Sigma 3^n$ and other 'special' boundaries, and break-up of the random boundary network. Several GBE studies have been applied on brass alloys due to its low stacking-fault energy (SFE) [3-7]. Most of the focus has been mainly made on α-phase brass alloy, which consists of FCC structure, to examine the effect of repetitive TMP on the increased proportion of Σ3 boundaries and grain boundary characteristic distribution. Nevertheless, no previous studies on repetitive TMP have reported the effect of deformation temperature on development of CSL boundaries in low SFE fcc metals. In this regard, the present work aims to evaluate the effect of deforming temperature on development of $\Sigma 3^n$ boundaries in α-phase brass during repetitive TMP.

Experimental Procedure:
Compression test cylinders of α-brass (70Cu–30Zn) were made with dimensions of 10 mm in diameter and 12.5 mm. Four TMP cycles were used in this study, with each cycle consisting of compression the cylinders to a strain of 0.15 at different test temperatures (25ºC, 250ºC and -100ºC) and later annealing at 670 ºC for 10 min. The microstructure of brass samples was analyzed using scanning electron microscopy (SEM) and electron back scattered diffraction (EBSD) technqiue. The samples were subjected to conventional metallographic preparation and finally electropolished in a solution of 25% phosphoric acid, 20% ethanol, and 10% propanol in water. The average grain size, grain size distributions and texture were determined from EBSD maps.

Results and Discussion:
Figure 1 shows an SEM micrograph illustraing the formation of annealing twins in the initial material, with an average grain size of 23 μm. In general, there are different sizes and shapes of the annealing twins: long-narrow twins extending throughout the parent grains, and short-wide twins formed within the parent grains. Fig.2 presents EBSD maps for cartridge brass samples processed up to 4 cycles at 25ºC. The results generally show that repetitive TMP resulted in large formation of annealing twins in the microstructure as demonstrated by the formation of Σ3 twin boundaries (shown in red color). The results also show that increasing number of cycles led to coarsening of the grains and also enlargement of the annealing twins.

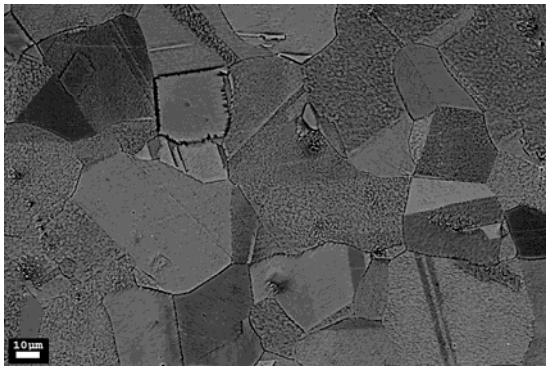

Figure 1: SEM micrograph of the initial microstructure of α-brass sample. (Magnification: 500X)

Table 1: Average grain size (μm) of brass samples

Sample	Cycle 1	Cycle 2	Cycle 3	Cycle 4
T= 25°C	37.0	37.6	41.6	48.3
T= 250°C	33.6	38.7	40.9	45.0
T=-100°C	35.8	37.2	44.2	46.4

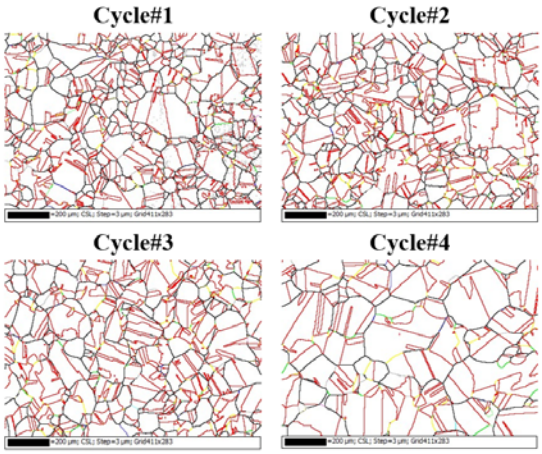

Figure 2: EBSD maps for TMP α-brass samples compressed at 25°C. Black lines denote random HABs, while red, yellow and green lines represent Σ3, Σ9 and Σ27 boundaries.

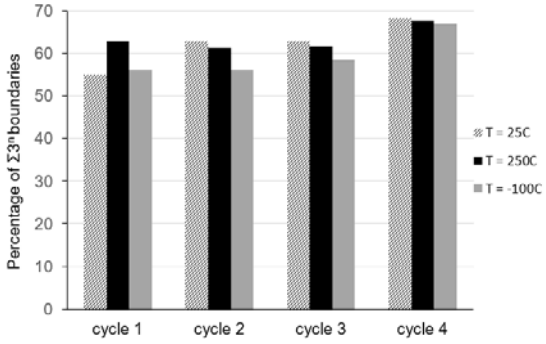

Figure 3: Distribution of $\Sigma 3^n$ boundaries for brass samples

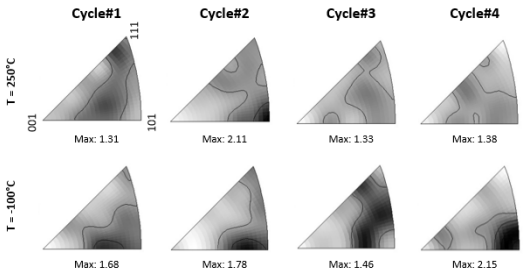

Figure 4: Inverse pole figures for brass samples annealed after being compressed at T= 250°C and T = -100°C.

Table 1 shows that the average grain size after cycle#1 is the range of 33.6-37.0 μm and it becomes coarser after cycle#4 (45.0 to 48.3 μm).Intersetingly, compressing samples at 250°C produced the smallest average grain size. This was found to correlate with the fast development of $\Sigma 3^n$ boundaries at cycle#1 for barss deformed at T=250°C as shown in Fig.4. The results also show that the frequency of $\Sigma 3^n$ boundaries remained unchanged for cycles 2 and 3.On the otherhand, the percentage of $\Sigma 3^n$ boundaries increased and became almost similar for the three compression temperatures at cycle#4 (68.3% for 25°C, 67.8% for 250°C and 66.9% for -100°C). The slow development of Σ3n boundaries after two cycles was reported in previous works [2,5]. This was necessary to homogenize the microstructure in preparation for subsequent cycles required for the enhancement of grain boundary characteristics and material properties. In such case, the strain is retained at twin boundaries during the first cycle of TMP and hence provides suffiecent driving force for recrystallization. Upon applying strain in the second cycle, annealing has more tendency to cause grain boundary migration and thus possible annihilation of some twins and strain relief occur. Additional cycles were shown to induce new strain into the material and thus providing necessary driving force for nucleation and generation of new annealing twins and break-up of the random boundary network. This has also been observed in the current TMP of brass as an increase in twinning activities occurred at cycle#4 for all compression temperatures.

For FCC metals of low stacking fault energy, such as brass, the annealing texture typically consists of a mixture of <111> and <001> fiber components, while the compression texture becomes a mixture of <111> and <101> fiber components due to the occurrence of deformation twinning. The compression texture for the brass in this work has a strong <101> fiber but weak <111> fiber. This implies that deformation twinning was not very active as a deformation mode during compression at small strain of 0.15. Fig. 4 presents the inverse pole figures for brass samples subjected to compression temperature of 250°C and -100°C. The results show annealing cuased scattering of the texture while the compression texture is partially retained around <101> fiber. The relatively lower values of maximum intensity for sample processed at 250°C is most likely attributed to the fast development of $\Sigma 3^n$ boundaries during cycle#1.

Acknowledgments: The author acknowledges the funding provided by Kuwait University under grant number EM02/13 and support provided by Kuwait University General Facility project (GE01/07) for sample preparation and SEM/EBSD. Addiotional fund was also made by Kuwait Foundation for the Advancment of Sciences.

References:

[1] Lehockey EM, and Palumbo G, Mater Sci & Engrg A, vol. 237, 1997, pp. 168-172.
[2] Randle V, Acta Materialia, 2004, vol.52, pp. 4067–81.
[3] Davies P, Randle V, Watkins G, and Davies H, J. Mater. Sci., 2002, vol. 37, pp.4203-09.
[4] Davies D, and RandleV, Philosophical Magazine A, 2001, vol. 81, pp.2553-64.
[5] RandleV, and Davies H, Metall. Mater Trans A, 2002, vol.33, pp.1853.
[6] Rohrer, GS, Randle V, Kim C-S, and Hu Y, Acta Mater., 2006, vol. 54, pp.4489-4502.
[7] Pinto AL, Viana CS, Luiz HA, Mater Sci & Engrg A, 2007, vol.445–446, pp.14–19.

Magnetic Excitation in Chiral Graphene Model

Yu.P.Rybakov, M.Iskandar and A.B.Ahmed
Department of Theoretical Physics and Mechanics
Peoples' Friendship University of Russia
117198 Moscow, 6, Miklukho-Maklay str, Russia
e-mail: soliton4@mail.ru

Abstract

The s- and p- hybridization effect for the valence electrons of carbon atoms appears to be the main property of the electron bonding in mono-atomic carbon layers of graphene. For realizing this effect the chiral model of graphene was suggested [1], the unitary $SU(2)$ matrix $V = a_0\tau_0 + i(\vec{a}\vec{\tau})$ being considered as an order parameter [2]. Here $\tau_0, \vec{\tau}$ denote the unit matrix and the Pauli matrices respectively, scalar and vector fields $a_0, \vec{a}; a_0^2 + \vec{a^2} = 1$, describing s- and p-states of the free valence electron. For the description of spin and quasi-spin excitation in graphene, the latter ones corresponding to independent excitation modes of the two triangular sub-lattices of graphene, we introduce the two Dirac spinors ψ_1, ψ_2 and consider the combined spinor field $\Psi = \xi \otimes (\psi_1 \oplus \psi_2)$as a new order parameter, where ξ stands for the first column of V. The electromagnetic interaction is included throught the extention of derivatives, the Pauli direct interaction term being added.

Keywords: chiral model of graphene, dirac spinors

The Lagrangian density $\mathcal{L}$ of the model

$$\mathcal{L} = \frac{I}{2}\overline{D_\mu \Psi} P D^\mu \Psi - \frac{\lambda^2}{2}\vec{a}^2 j_\mu j^\mu + i\mu_0 \overline{\Psi}\sigma_{\mu\nu}F^{\mu\nu}\Psi \qquad (1)$$

includes the projector $P = \gamma^\nu j_\nu$ on the positive energy states, where $j_\mu = \overline{\Psi}\gamma_\mu\Psi, \mu = 0, 1, 2, 3$, designates the Dirac current,$\overline{\Psi} = \Psi^+\gamma_0$. The model

contains the two constant parameters: the exchange energy I per lattice spacing and some characteristic inverse length $\sqrt{\lambda}$. The interaction with the electromagnetic field is realized through the extension of the derivative:
$D_\mu = \partial_\mu - ie_0 A_\mu \Gamma_e$, with $e_0 > 0$ being the coupling constant and $\Gamma_e = (1-\tau_3)/2$ being the charge operator chosen in accordance with the natural bondary condition at infinity: $a_0(\infty) = 1$. However, the additional interaction term of the Pauli type should be added to take into account the proper magnetic moments of the electrons. Here $\sigma_{\mu\nu} = [\gamma_\nu, \gamma\mu]/4, F_{\mu\nu} = \partial_\mu A_\nu - \partial_\nu A_\mu$ and $\mu_0 > 0$ denotes the Bohr magneton per lattice spacing cubed.
Let us consider as an illustration the interaction of the mono-atomic carbon layer $z = 0$ with the static uniform magnetic field $\vec{B_0}$ oriented along the x-axis. We introduce first the vector potential $A_y = A(z)$, with the intensity of the magnetic field being $B_x = B(z) = -A'(z)$ and the natural boundary condition at infinity: $A \to -B_0 z$. The model in question admits the evident symmetry $\psi_1 \Leftrightarrow \psi_2, \gamma_0-$invariance $\Psi \Rightarrow \gamma_0\Psi$ and also the discrete symmetry:$\psi_i \Leftrightarrow \psi_i^*; a_{2,3} \Rightarrow -a_{2,3}$. Therefore,one can introduce the chiral angle $\Theta(z) : a_0 = cos\Theta, a_1 = sin\Theta$ and the real 2-spinor $\varphi(z) = col(u, -u)$, where $\psi_1 = \psi_2 = col(\varphi, \varphi)$. As a result the new Lagrangian density take the form:

$$\mathcal{L} = -2IU'^2 - 8IU^2(\Theta'^2 + e_0^2 A^2 sin^2\Theta) - 8\lambda^2 U^2 sin^2\Theta - 4\mu_0 A'U - A'^2/(8\pi) \quad (2)$$

where the new variable is introduced: $U = |\varphi|^2 = 2u^2$. Taking into account that $j^2 = 16U^2$, one can deduce from (2) and the boundary condition at infinity: $j^2(\infty) = 1, \Theta(\infty) = 0, A'(\infty) = -B_0$ the following "energy" integral:

$$E = -2IU'^2 - 8IU^2(\Theta'^2 - e_0^2 A^2 sin^2\Theta) + 8\lambda^2 U^2 sin^2\Theta - A'^2/(8\pi) = -B_0^2/(8\pi),$$

that implies the Hamilton-Jacobi equation for the "action" S:

$$\frac{1}{8I}\left(\frac{\partial S}{\partial U}\right)^2 + \frac{1}{32IU^2}\left(\frac{\partial S}{\partial \Theta}\right)^2 + 2\pi\left(\frac{\partial S}{\partial A} + 4\mu_0 U\right)^2 = \frac{B_0^2}{8\pi} + 8U^2 sin^2\Theta(\lambda^2 + Ie_0^2 A^2) \quad (3)$$

Here the following defenitions of the Jacobi momentums are used:

$$\frac{\partial S}{\partial U} = -4IU'; \frac{\partial S}{\partial \Theta} = -16IU^2\Theta'; \frac{\partial S}{\partial A} = -4\mu_0 U - \frac{A'}{4\pi} \tag{4}$$

Let us study the behavior of solution to the equation (3) and (4) as $z \to \infty$ where $A \approx -B_0 z$. In the first approximation one gets:

$$S \approx \left[\frac{B_0}{4\pi} - \mu_0 - 8e_0 IU^2 sin^2\Theta\right] A \tag{5}$$

Inserting (5)into (4), one derives the differential equation $U' = 4U\Theta' tan\Theta$ with the evident integral $4U = cos^{-4}\Theta$ corresponding to the boundary condition $U(\infty) = 1/4$. In view of (4)this fact permits to obtain the equation for $\Theta(z) = \frac{2\Theta'}{sin2\Theta} = e_0 A \approx -e_0 B_0 z$ with the solution of the form:

$$tan\Theta = tan\Theta_0 exp\left[-\frac{e_0}{2} B_0 z^2\right] \tag{6}$$

where Θ_0 stands for the integration constant. Finally, combining (6)and the last relation in (4), one can find the magnetic field intensity in the asymptotic domain $z \to \infty$:

$$B = -A' \approx B_0 - 2\pi(e_0 I - 4\mu_0)\Theta_0^2 exp(-e_0 B_0 z^2) \tag{7}$$

As can be seen from(7), the effect of weakening of the magnetic field is revealed for the positive value of the constant $e_0 I - 4\mu_0$, this effect being similar to that of London "screening" caused by the second term in the electromagnetic current:

$$J_\mu = e_0 I Im(\overline{\Psi} P \Gamma_e \partial_\mu \Psi) - e_0^2 I j^2 (a_1^2 + a_2^2) A_\mu + 2i\mu_0 \partial^\nu (\overline{\Psi}\sigma_{\mu\nu}\Psi) \tag{8}$$

The current (8)contains beyond the standard conduction term, the diamagnetic current and the Pauli magnetization-polarization one.

As follows form(7), for the negative value of the constant $e_0 I - 4\mu_0$ the paramagnetic behavior of the material takes place [3, 4]

Bibliography

[1] Rybakov Yu P.//Solid State Phenomena, v.190.2012, P.59-62.

[2] Yu.A Izymov, M.I. Katsnelson and Yu.N.Skryabin. Itinerant Electron Magnetism,-Moscow: Nauka, 1994.

[3] Geim A.K.//Science, v.324.2009, P.1530-1534

[4] Katsnelson M.I., Novoselov K.S.//Solid State Communications, v. 143.2007, P.3-13.

Fabrication of Metal Oxide/Reduced Graphene Oxide Nanocomposites for Anodes in Li-ion Batteries

Edreese Alsharaeh*[1], Faheem Ahmed[1], Yasmin Mussa[1], Yazeed Aldawsari[1], Ali Hendawi[1], Mohammad Alshahrani[2], Hatem Abuhimd[2], Lain-Jong Li[3]

[1]Dept. of chemistry, College of Science & General Studies, Alfaisal University, Riyadh, Saudi Arabia,
[2]National Nanotechnology Research Center, King Abdulaziz City for Science and Technology, Riyadh, Saudi Arabia,
[3] King Abdullah University of Science and Technology, Physical Science & Engineering Division, Thuwal 23955-6900, Saudi Arabia
***E-mail:** ealsharaeh@alfaisal.edu, Tel: +966-55-215-7739, fax: +966-55-215-7739

Abstract
In this work, we report a simple one-step microwave irradiation method to synthesize the nanocomposites of cobalt oxide (Co_3O_4) nanoparticles and reduced graphene oxide (RGO). X-ray diffraction (XRD) and Raman studies revealed the formation of crystalline Co_3O_4 nanoparticles on the RGO sheets. Ultraviolet–visible (UV-Vis) spectra showed the characteristic absorption peaks of Co_3O_4 nanoparticles and RGO. From field emission scanning electron microscopy (FESEM) analysis, nanoporous structure was observed for Co_3O_4/RGO nanocomposites. These novel Co_3O_4/RGO nanocomposites exhibited good cycling stability as an anode material for lithium-ion batteries. The results have shown an electrochemical response in terms of charge/discharge capacity (174 mAh/g at 1 mA/g). Cyclic performance was also good as a reversible capacity (158 mAh/g at 1 mA/g) was retained for 10 charge/discharge cycles. The presented approach to prepare graphene based nanocomposites within few minutes using cheap, cost effective and environmental friendly microwave irradiation method will be a track to bridging between laboratory and industry for future energy applications.

Keywords: Nanocomposites; Li-ion battery; Microwave irradiation; TEM; XRD.

1. Introduction

Li-ion battery (LIB) has shown great potential to fulfil the growing energy demands for hybrid electric vehicle, smart grid applications, and portable electronic devices, due to its advantages such as high power and energy density, long cycle life and structure stability [1–4]. The energy density and performance of LIBs are largely determined by the chemical and physical properties of the cathode and anode materials [5–7]. Although significant progress has been made in improving the properties of electrode materials over the years [8–10], there is immense interest to develop new electrode materials that can boost both the energy and power densities of LIB [11–13].

As an allotrope of carbon, graphene consists of a single planar sheet of sp^2-bonded carbon atoms that are densely packed in a honeycomb crystal lattice. Graphene has been demonstrated to be a promising anode material for LIBs due to its intriguing physical and chemical properties, such as high electrical conductivity, large specific surface area, and mechanical robustness [14–16].

Co_3O_4 nanoparticles have been synthesized using different methods such as co-precipitation, hydrothermal synthesis, thermal decomposition and reduction et al. [17-20]. Synthesis of Co_3O_4/RGO

nanocomposites is usually achieved by in situ reduction of cobalt salt precursors or assembly of the nanoparticles on the GO surface [21]. However, some problems with the approaches reported so far, such as poor control over the size, size distribution, and location of nanoparticles on the GO sheets. To solve this issue, Co_3O_4 and Co_3O_4/RGO nanocomposites were synthesized using a novel, cost effective, and environmental friendly solution method assisted with microwave irradiation (MWI), The synthesized nanocomposites can be used as anodes in LIB.

2. Materials and methods

In a typical synthesis of Co_3O_4/RGO nanocomposites, 920 mg of CTAB was mixed with 800 ml of distilled water and 8% (2mg/ml) GO (synthesized by the hummer's method [22]) in a 1000 ml beaker. After 30 minutes of continuous stirring, a mixture of 4.6 g of cobalt acetate in 333 ml distilled water was added drop wise to the solution. Next, 1ml of the reducing agent hydrazine hydrate was added to the solution. The solution was heated under microwave irradiation (KENWOOD; 740 W) for 20 minutes with a power of 100W; then the product was washed several times by distilled water and ethanol and then was dried at 80^0 C overnight. The dried sample was ground and calcined at 600 ^{0}C for 2h. A black coloured product was obtained. In addition, pure Co_3O_4 nanoparticles and RGO were synthesized by the same method.

The X-ray diffraction (Philips-PW 1729, Holland) of the material were investigated with Cu radiation (1.54430 A°). The XRD patterns were recorded in the scan ranging from 5^o to 60^o of 2θ, with a step size of 0.02^o and scan speed of 2^o/min. A field emission scanning electron microscope (FESEM, FEI Quanta 200) was employed to study the morphology of the product. Room temperature optical absorption spectra were recorded in the range of 200–800 nm using a UV-Vis spectrophotometer (Agilent-8453).

The electrochemical performance was evaluated using two-electrode coin half-cell with a polypropylene membrane separator (Celgard 2325, Celgard, Inc., USA) as separator and Li-metal (purity 99.9%) as counter electrode. 1 M $LiPF_6$ in EC/DMC (1:1, v/v) was used as an electrolyte. Cells were assembled in a dry room and galvanostatically charged/discharged at current densities of 1 mA in a potential range of 0.01 to 3V, using 8-channel battery tester (MTI-USA).

3. Results and discussion

XRD analysis was done to study the crystal phase of the Co_3O_4 nanoparticles and Co_3O4/RGO nanocomposites as shown in Fig. 1.

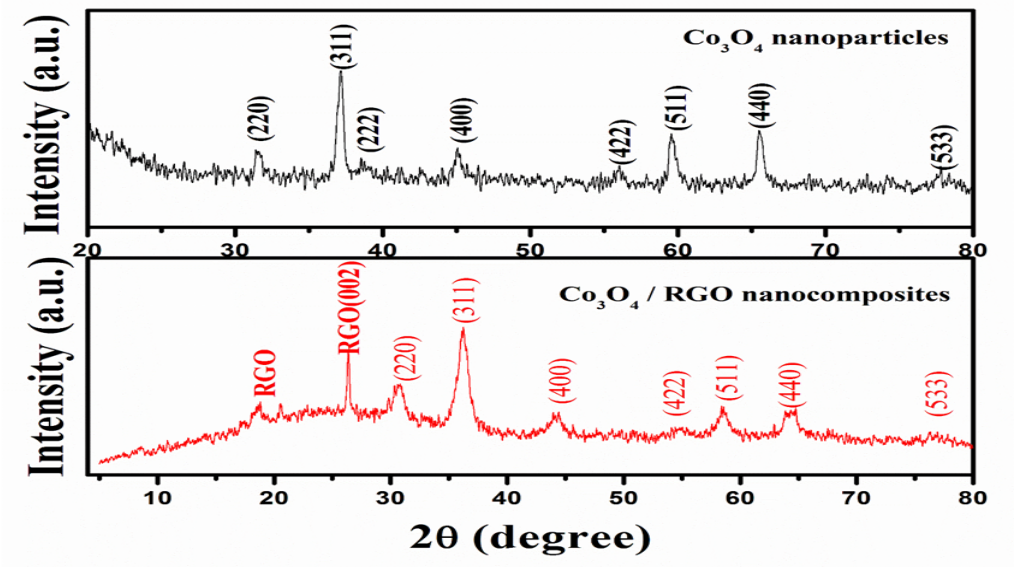

Fig. 1: XRD pattern of Co_3O_4 nanoparticles and Co_3O_4/RGO nanocomposites (8%RGO).

The diffraction peaks at 2θ of 31.55^0, 37.23^0, 38.54^0, 45.04^0, 56.09^0, 59.50^0, 65.68^0 and 77.71^0 can be indexed as the (220), (311), (222), (400), (422), (511), (440) and (533), respectively. The diffraction peaks of the Co_3O_4 nanoparticles are similar to those of pure Co_3O_4 with cubic normal spinel structure (JCPDS card no. 76–1802). No other peaks of impurity were detected. In addition to the characteristic peaks attributed to Co_3O_4 nanoparticles, the XRD pattern of Co_3O_4/RGO nanocomposites also exhibits an extra peak at around 19^0 which can be indexed as the (002) proving the presence of RGO [22].

4. Conclusion

In summary, Co_3O_4/RGO nanocomposites (8% RGO) were successfully prepared using microwave assisted solution method. XRD, UV-Vis and Raman results show that the prepared nanocomposites containing highly crystalline Co_3O_4 nanoparticles and RGO sheets. Morphological studies show nanoporous structure Co_3O_4 supported on RGO sheets. The nanocomposites prepared by MWI shows remarkable properties as a good anode material for LIBs. A good electrochemical response in terms of charge/discharge capacity, cyclic performance, and columbic efficiency was observed. This excellent performance could be attributed to the formation of 2D RGO framework decorated with Co_3O_4 nanoparticles.

5. Acknowledgment

The authors would like to acknowledge King Abdulaziz City for Science and Technology for funding this work.

References

1. Qie, L. et al. Nitrogen-Doped Porous Carbon Nanofiber Webs as Anodes for Lithium Ion Batteries with a Super-high Capacity and Rate Capability., Adv. *Mater.,* **24,** 2047, (2012).
2. Wang, H., et al. Mn_3O_4−Graphene Hybrid as a High-Capacity Anode Material for Lithium Ion Batteries., *J. Am. Chem. Soc.,* **132,** 13978 **(**2010).
3. Fan, Z.J. et al. Nanographene-Constructed Carbon Nanofibers Grown on Graphene Sheets by Chemical Vapor Deposition: High-Performance Anode Materials for Lithium Ion Batteries. *ACS Nano*, **5**, 2787 (2011).

4. Jiang, Z. & Jiang, Z. J. Effects of carbon content on the electrochemical performance of $LiFePO_4$/C core/shell nanocomposites fabricated using $FePO_4$/polyaniline as an iron source. *J. Alloys Compd.,* **537,** 308, (2012).
5. Hou, J., Shao, Y., Ellis, M. W., Moore, R. B. & Yi, B. Graphene-based electrochemical energy conversion and storage: fuel cells, supercapacitors and lithium ion batteries., *Phys. Chem. Chem. Phys.,* **13**, 15384, (2011).
6. Shen, L., Zhang, X., Li, H., Yuan, C. & Cao, G. Design and Tailoring of a Three-Dimensional TiO_2–Graphene–Carbon Nanotube Nanocomposite for Fast Lithium Storage., *J. Phys. Chem. Lett.,* **2**, 3096, (2011).
7. Wu, Z.S., Ren, W., Xu, L., Li, F. & Cheng, H.M. Doped Graphene Sheets as Anode Materials with Super-high Rate and Large Capacity for Lithium Ion Batteries. *ACS Nano*, **5**, 5463, (2011).
8. Li, S. at al. Vertically Aligned Carbon Nanotubes Grown on Graphene Paper as Electrodes in Lithium-Ion Batteries and Dye-Sensitized Solar Cells. *Adv. Energy Mater.,* **1**, 486, (2011).
9. Chen, S., Yeoh, Liu. & Wang, W. Q. G. Chemical-free synthesis of graphene–carbon nanotube hybrid materials for reversible lithium storage in lithium-ion batteries. *Carbon*, **50**, 4557, (2012).
10. Yao, F. et al. Diffusion Mechanism of Lithium Ion through Basal Plane of Layered Graphene., *J. Am. Chem. Soc.,* **134**, 8646, (2012).
11. Wang, Z. L. et al. Facile, mild and fast thermal-decomposition reduction of graphene oxide in air and its application in high-performance lithium batteries., *Chem. Commun.,* **48**, 976, (2012).
12. Chen, X. C. et al. A graphene-based nanostructure with expanded ion transport channels for high rate Li-ion batteries. *Chem. Commun.,* **48**, 5904, (2012).
13. Wen, Z. et al. Binding Sn-based nanoparticles on graphene as the anode of rechargeable lithium-ion batteries. *J. Mater. Chem.,* **22**, 3300, (2012).
14. Xiang, H. F. et al. Graphene sheets as anode materials for Li-ion batteries: preparation, structure, electrochemical properties and mechanism for lithium storage. *RSC Adv.,* **2**, 6792, (2012).
15. Wang, C., Li, D., Too, C. O. & Wallace, G. G. Electrochemical Properties of Graphene Paper Electrodes Used in Lithium Batteries., *Chem. Mater.,* **21**, 2604, (2009).
16. Yin S. et al. Assembly of Graphene Sheets into Hierarchical Structures for High-Performance Energy Storage. *ACS Nano*, **5**, 3831, (2011).

17. Wang X, Chen XY, Gao LS, Zheng HG, Zhang Z, Qian YT, One-Dimensional Arrays of Co3O4Nanoparticles: Synthesis, Characterization, and Optical and Electrochemical Properties, J Phys Chem B 2004;108:16401.
18. Yang RZ, Wang ZX, Liu JY, Chen LQ, Nano Co3O4 Particles Embedded in Porous Hard Carbon Spherules as Anode Material for Li-Ion Batteries, Electrochem Solid State Lett 2004;7:A496.
19. Salabas EL, Rumplecker A, Kleitz F, Radu F, Schuth F, Exchange Anisotropy in Nanocasted Co_3O_4 Nanowires, Nano Lett 2006;6:2977.
20. Moro F, Tang SVY, Tuna F, Lester E, Detection of para–antiferromagnetic transition in $Bi_2Fe_4O_9$ powders by means of microwave absorption measurements, J Magn Magnet Mat 2013;348:1–7.
21. Shen JF, Hu YZ, Shi M, Li N, Ma HW, Ye MX, One Step Synthesis of Graphene Oxide−Magnetic Nanoparticle Composite, J Phys Chem C 2010;114:1498.

22. Alsharaeh EH, Othman AA, Microwave irradiation synthesis and characterization of RGO-AgNPs/polystyrene nanocomposites, Polymer Comp 2014;35:2318.
23. Hadjiev VG, Iliev MN, Vergilov IV, The Raman spectra of Co3O4, *J Phys C: Solid State Phys* 1988;21:L199.
24. Reddy, M. V. et al. α-Fe_2O_3 Nanoflakes as an Anode Material for Li-Ion Batteries., *Adv. Funct. Mater.,* **17**, 2792 (2007).